MIDDLE EAST TECHNICAL UNIVERSITY
EARTHQUAKE ENGINEERING RESEARCH CENTER

THE ELÂZIĞ-SİVRİCE EARTHQUAKE [24 JANUARY 2020 M_W=6.8] FIELD OBSERVATIONS ON SEISMIC AND STRUCTURAL DAMAGE

REPORT NO: METU/EERC 2020-01

MARCH 2020
ANKARA

MIDDLE EAST TECHNICAL UNIVERSITY
EARTHQUAKE ENGINEERING RESEARCH CENTER

THE ELÂZIĞ-SİVRİCE EARTHQUAKE [24 JANUARY 2020 M_W=6.8] FIELD OBSERVATIONS ON SEISMIC AND STRUCTURAL DAMAGE

REPORT NO: METU/EERC 2020-01

MARCH 2020
ANKARA

Editors

Spec. Salim AZAK

Res. Asst. Okan KOÇKAYA

Acknowledgments

We would like to express our sincere thanks to the Office of the President of the Middle East Technical University, the Dean of the Faculty of Engineering, the Head of the Department of Civil Engineering and all the persons and organizations mentioned below, for their support and contributions before, during and after the emergence of this study.

METU Earthquake Engineering Research Center also would like to thank:

- The Office of the President of the Fırat University for providing great assistance during the field studies and researches,
- The faculty members and research assistants of Fırat University; Assoc. Prof. Dr. Muhammet KARATON, Assoc. Prof. Dr. Erkut SAYIN, Assist. Prof. Dr. Ayşe Ruşen DURUCAN, Assist. Prof. Dr. Cengizhan DURUCAN and Res. Asst. Dursun BAKIR, who provided all kinds of assistance and who accompanied during the investigations of reinforced concrete buildings,
- The faculty members of Hacettepe University Department of Civil Engineering; Prof. Dr. Berna UNUTMAZ and Assoc. Prof. Dr. Mustafa Kerem KOÇKAR, the faculty members of Erzurum Technical University Department of Civil Engineering; Assist. Prof. Dr. Dilek OKUYUCU, the faculty members of Fırat University Department of Civil Engineering; Assist. Prof. Dr. Ayşe Ruşen DURUCAN and Asst. Prof. Dr. Cengizhan DURUCAN, and Res. Asst. Abdullah İÇEN, one of the Research Assistants of the Munzur University Department of Civil Engineering, for their contribution and support to damage investigations in rural areas, and
- Assoc. Prof. Dr. Nejan HUVAJ SARIHAN, faculty member of the Middle East Technical University Department of Civil Engineering, Kâmil ERGÜNER, the Chief Bridge Engineer from MEGA Mühendislik, Res. Asst. Burak AKBAŞ, one of the Research Assistants of the Atılım University Department of Civil Engineering, Murat KENKÜL , graduate of Middle East Technical University Department of Civil Engineering, and Muhammet DURMAZ, graduate student of Middle East Technical University Civil Engineering Department, for their contribution and support during bridge performance observations.

Contents

Figures

Tables

Chapter 1
Introduction

Prof. Kemal Önder ÇETİN[1]

Res. Asst. Makbule ILGAÇ[1]

Res. Asst. Gizem CAN[1]

Res. Asst. Elife ÇAKIR[1]

Res. Asst. Berkan SÖYLEMEZ[1]

[1] *Middle East Technical University*

1.1 Introduction

On January 24, 2020 at 8.55.11 p.m. local time (UTC 5.55.11 p.m.), a moment magnitude M_w 6.8 (AFAD; Disaster and Emergency Management Presidency; www.afad.gov.tr) or M_w 6.7 (USGS) earthquake occurred on the East Anatolian Fault zone, due to a NE-SW strike-slip fault rupture along the Sivrice-Pütürge Segment in Elâzığ, Turkey. Within the confines of this report, the findings of geological, seismological and geotechnical and structural reconnaissance studies as well as preliminary field investigation studies will be presented. In addition to geological and geotechnical evaluations in the course of reconnaissance studies, some typical lifeline and superstructure damage examples are also given. Independent engineering groups composed of earth scientists, geological, geophysical, and civil engineers have compiled and documented perishable data immediate upon Elâzığ-Sivrice earthquake. For the purpose of honoring collaborative research studies among different disciplines and universities, it was decided to present the findings in a co-authored report. We believe that this report and others will encourage and reinforce further interdisciplinary studies and culture of collaborative research.

The cities of Elâzığ and Malatya are located in the eastern Turkey as shown in Figure 1.1. The epicenter is located at N38.3593°, E39.0630°, approximately 37 km south-southwest of Elâzığ, and 64 kms east of Malatya with a focal depth of 8.06 km (AFAD). Sivrice-Pütürge segment is located within the East Anatolian Fault system in association with the tectonic boundary of the Eurasian, Arabian and African plates and Anatolian Block, which accommodates approximately 5-10 mm annual slip (Gulerce et al., 2017). The effects of the Elâzığ-Sivrice earthquake have been widely observed across Elâzığ and Malatya regions, extending from Hazar Lake in the east to downtown Malatya in the west. The cities of Kahramanmaraş, Diyarbakır, Adıyaman, Şanlıurfa and Batman have also felt the earthquake shaking relatively strongly. Despite attempts to identify and map surface expressions of fault rupture, a clear evidence has not been reported (yet). However, in the literature and the press, there exist contradicting opinions.

Turkey is a tectonically active country, and regularly experiences damaging earthquakes. Within 250 km of January 24, 2020 earthquake event, on the EAFZ, seven other M_w 6 or larger events have been reported to occur since 1870's. Several of these events have been destructive:

- In May 1971, M_w 6.9 Bingöl earthquake, 150 km to the northeast of this recent event killed 65 people and also caused significant damage.
- In September 1975, M_w 6.7 Lice earthquake, about 140 km to the east of the recent event killed more than 2,000 people and caused significant local damage.
- In May 1986, M_w 6.1 Sürgü earthquake, about 120 km to the west of this earthquake, killed 15 people and damaged over 4,000 houses.
- In May 2003, M_w 6.4 Bingöl earthquake, 140 km to the northeast of the recent event's epicenter killed 177 people, injured hundreds, and destroyed over 700 buildings.
- In March 2010, M_w 6.1 Elâzığ-Kovancılar earthquake, 100 km to the northeast of 2020 event killed 42 people, injured 100 people, and destroyed close to 300 buildings.

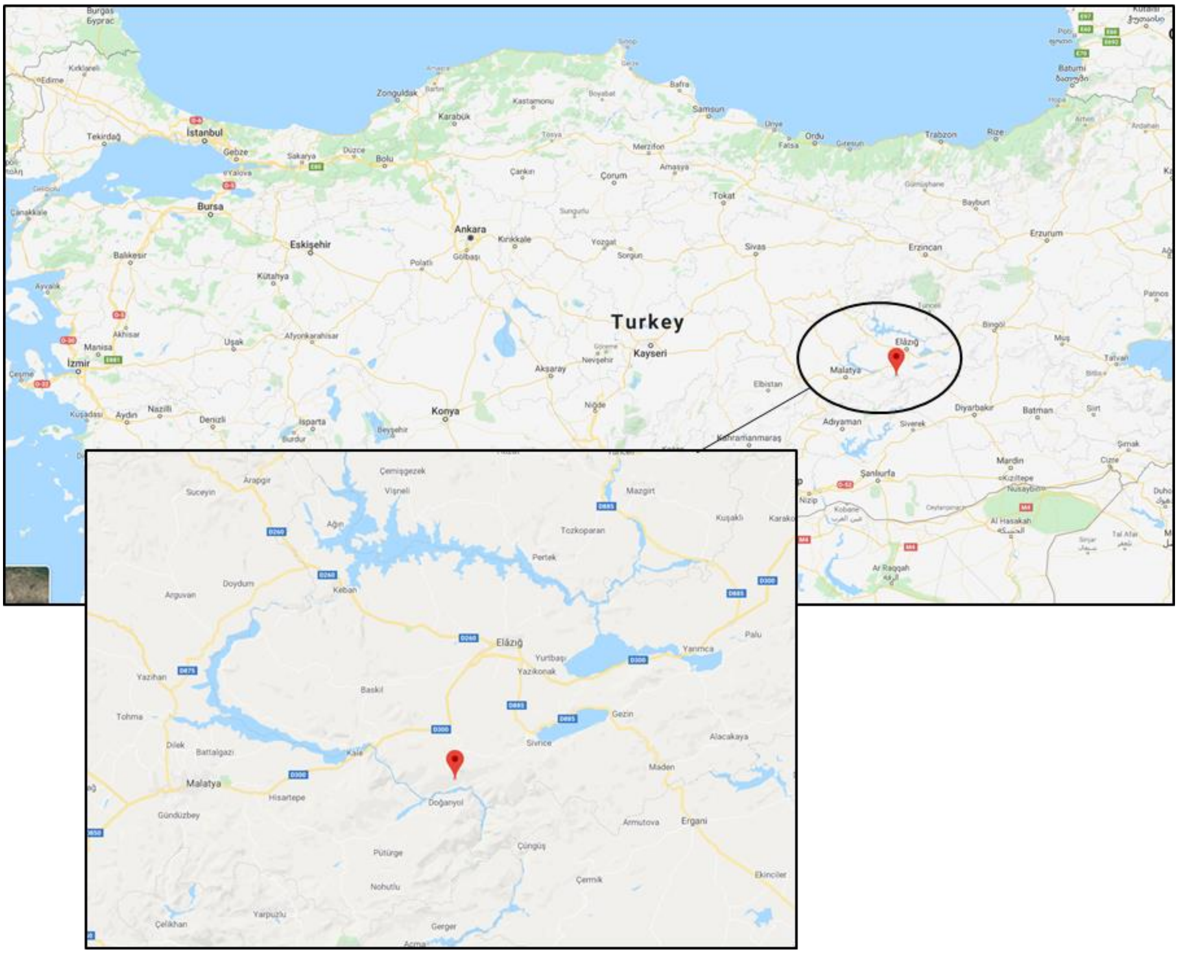

Figure 1.1 Map of Turkey (Google Maps) The epicenter of the January 24, 2020 Earthquake is shown with a red pin.

On the basis of the events listed and the map shown in Figure 1.2, it can be concluded that January 24, 2020 event has occurred on a segment of the east Anatolian fault, which has been seismically quiet since the last earthquake in 1875.

41 citizens lost their lives, and owing to successfully managed search and rescue operations, 45 citizens have been rescued from the heavily damaged and/or collapsed residential structures. 1,587 out of 1,631 injured citizens are soon discharged, 46 of citizens, 5 of whom are under intensive care, continue to be treated, as of February 3, 2020. Following the major shock of Elâzığ-Sivrice earthquake, again as of February 3, 2020, a total number of 1,948 aftershocks occurred in the region. 23 of these aftershocks have magnitudes over 4.0.

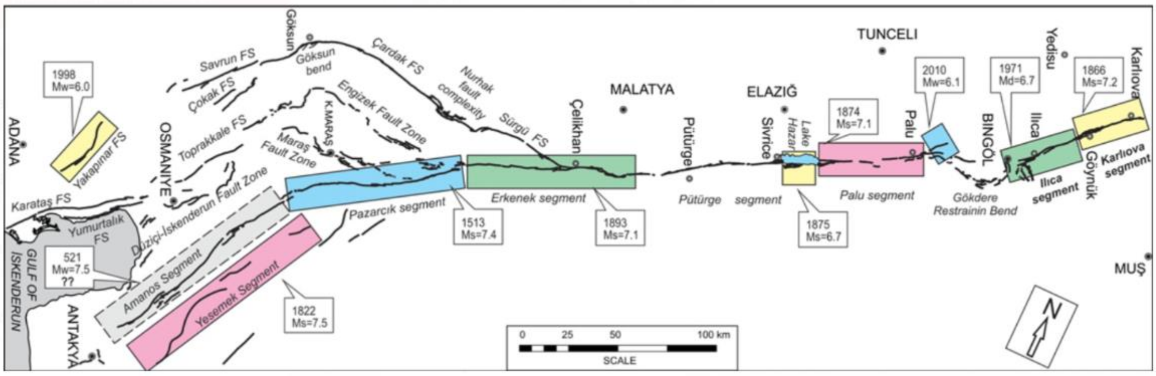

Figure 1.2 Different segments of the East Anatolia fault zone (Duman and Emre, 2013)

In response to this event, several research teams have visited the region to investigate the effects of the earthquake. The preliminary objective of the reconnaissance efforts was to document the effects of strong shaking on buildings and ground failure such as the prevalence of liquefaction, landslides and surface fault rupture. Our research team has visited the area on the 31st of January to collect and document perishable data in the form of ground deformations, liquefaction, lateral spreading and slope instabilities, rock falls and retaining structures. Additionally, the performances of railway systems, hydraulic structures, highways and residential structures on the investigation route are also documented. As a result, the subsequent investigative efforts have been mostly focused on documenting the following topics:

- Background information related to the geology of the region,
- Seismology and ground motions of the event,
- Detailed mapping of ground deformations,
- Measuring ground deformation in the very near fault region,
- Assessing the performance of slope instabilities
- Assessing the performance of hydraulic structures and railways.

The findings regarding all these will be presented next.

Chapter 2
Geological Setting of the Region (Compiled Study)

Prof. Kemal Önder ÇETİN[1]

Res. Asst. Makbule ILGAÇ[1]

Res. Asst. Gizem CAN[1]

Res. Asst. Elife ÇAKIR[1]

Res. Asst. Berkan SÖYLEMEZ[1]

[1] *Middle East Technical University*

2.1 Tectonic Setting

January 24, 2020 Elâzığ-Sivrice Earthquake occurred on Turkey's the second largest fault system: left lateral strike slip East Anatolian Fault Zone's (EAFZ) Sivrice-Pütürge segment. The EAFZ is defined by a zone of fault segments that joins the eastern end of the North Anatolian Fault Zone (NAFZ) to the Mediterranean Sea in the Gulf of Iskenderun (Taymaz et al 1991). NAFZ meets EAFZ at the Karlıova junction.

EAFZ exhibits translational characteristics, which is induced due to continent-continent collision of Arabian-African and the Eurasian plates. The interaction of four major tectonic plates of Arabian, Eurasian, Indian, and African with relatively smaller tectonic block of Anatolia is the source of high seismicity in the region, as shown in Figure 2.1 (USGS, Bozkurt 2001). Owing to more recent tectonic processes, EAFZ is under a tectonic compression regime in the N-S direction. The Anatolian block, squeezed between NAFZ and EAFZ, is moving towards the west. (Şengör et al., 1985; AFAD Report, 2010). The EAFZ predominantly produces left-lateral strike-slip events with occasional normal segments, but its fault trace is less continuous and less localized than that of the NAFZ. Recent GPS data indicated that the slip rate in the EAFZ has an upper bound of 8±1 mm/year (Ambraseys, 2009).

Historically, the EAFZ has nucleated relatively small magnitude earthquakes in the twentieth century (www.koeri.boun.edu.tr) contrary to NAFZ, which characteristically generates M_w greater than 7 events. Figure 2.2 shows the active fault map of Turkey as provided by General Directorate of Mineral Research and Explorations (MTA).

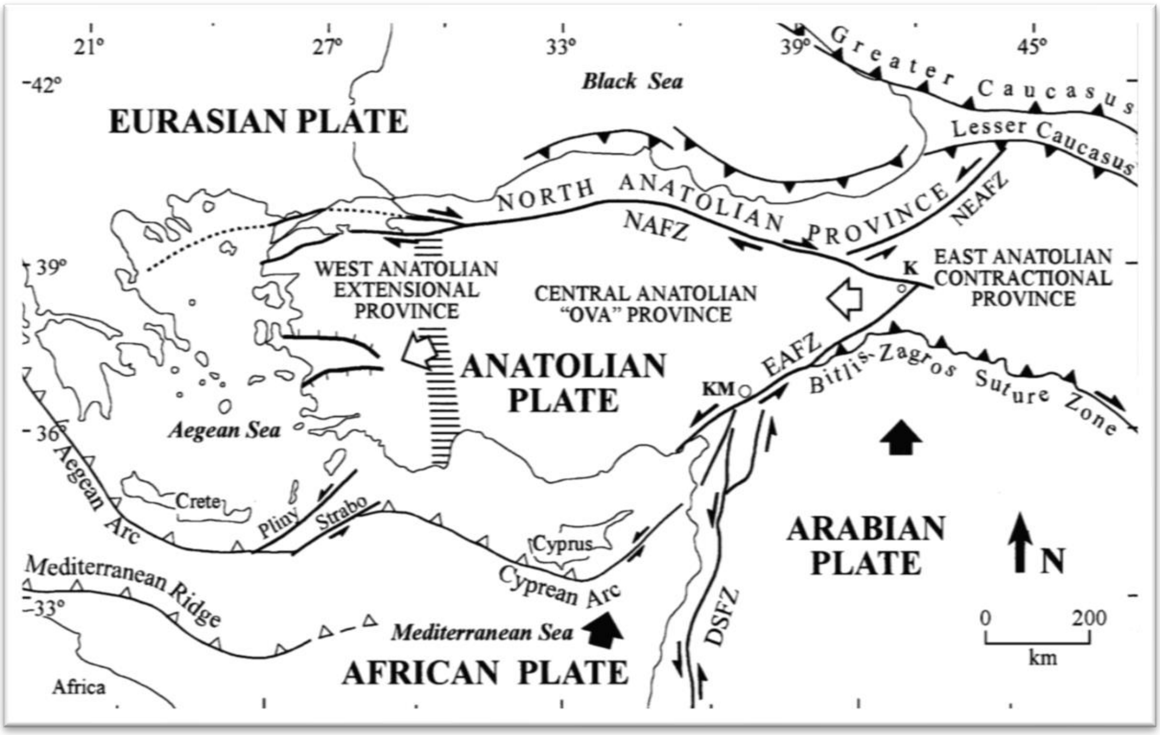

Figure 2.1 Tectonic structure of Turkey (from Bozkurt 2001).

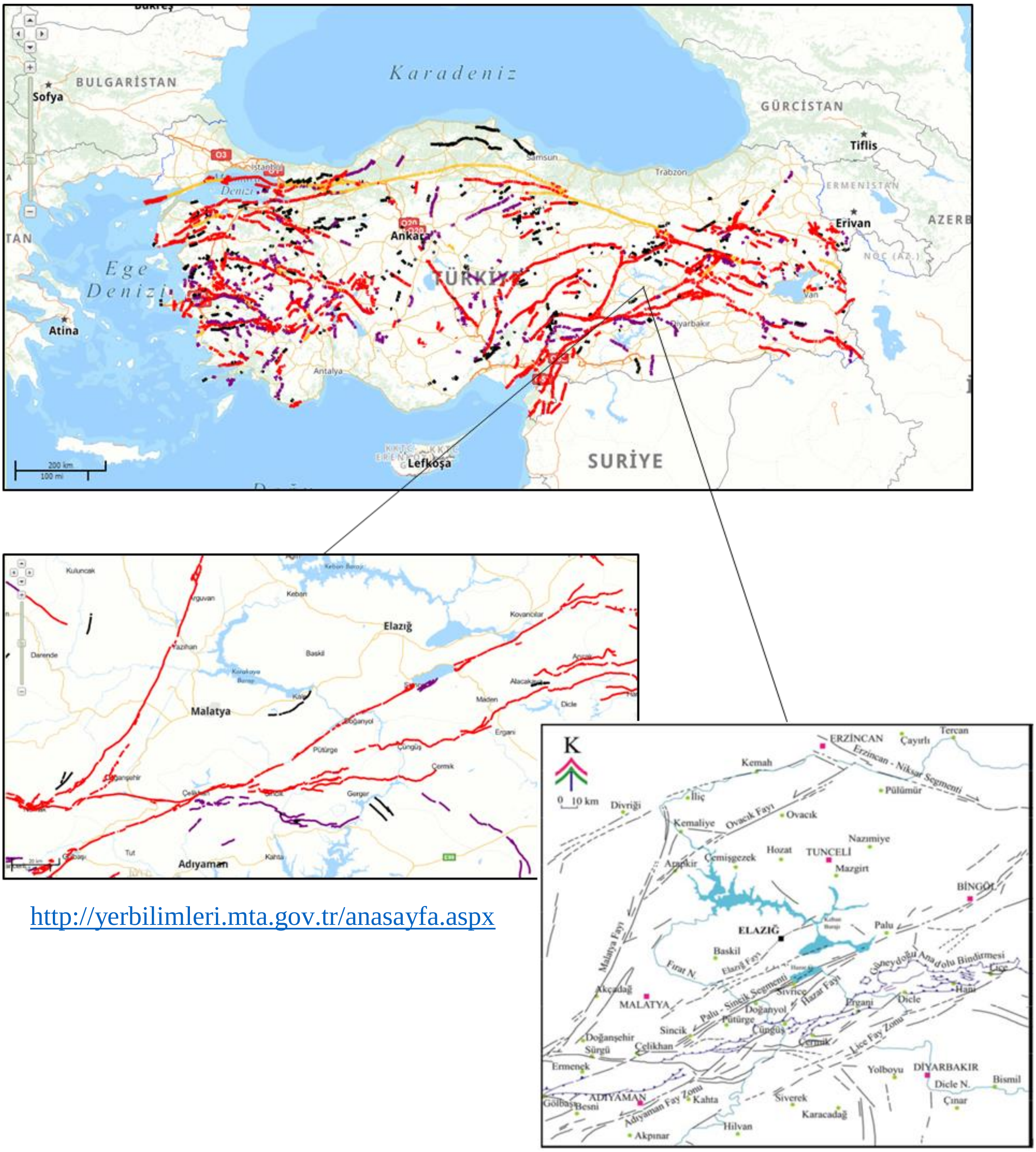

http://yerbilimleri.mta.gov.tr/anasayfa.aspx

(Palutoğlu ve Tanyolu, 2006)

Figure 2.2 Active faults and fault segments in the vicinity of Elâzığ and Malatya cities (MTA, 2020)

2.2 Historical Earthquakes

In the twentieth century, EAFZ produced several large earthquakes (M_w>7) with surface rupturing exhibiting complex migration patterns, as shown in Figure 2.3 (Barka, 1996; Utkucu et al., 2003). As reported by AFAD 2020, in the 20th century, on the EAFZ, 299 earthquakes occurred with M_w larger than 4.0, the largest of which was a 6.9 moment magnitude event. Also, before year 1900, 40 historical earthquakes have been reported in the region.

Several of these destructive earthquakes as summarized by USGS are briefly discussed below:

- M_w 6.9 Bingöl earthquake in May 1971, 150 km to the northeast of the killed 65 and also caused significant damage.
- M_w 6.7 Lice earthquake in September 1975, about 140 km to the east of today's earthquake killed more than 2,000 people and caused significant local damage.
- M_w 6.1 Sürgü earthquake in May 1986, about 120 km to the west of this earthquake, killed 15 and damaged over 4,000 houses.
- M_w 6.4 Bingöl earthquake in May 2003, 140 km to the northeast of today's event killed 177 people, injured hundreds, and destroyed over 700 buildings.
- M_w 6.1 Elâzığ-Kovancılar earthquake in March 2010, a 100 km to the northeast killed 42, injured 100, and destroyed close to 300 buildings.

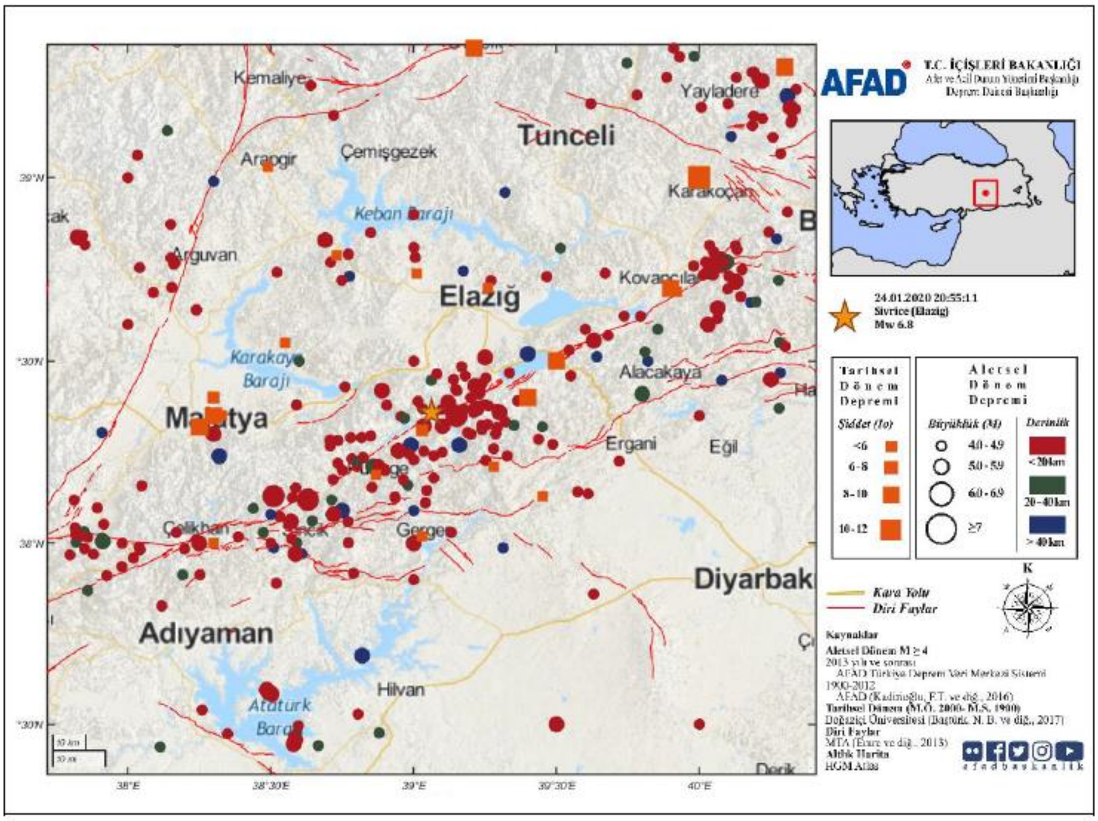

Figure 2.3 Seismicity of EAFZ during the last century (AFAD, 2020)

2.3 Geological Setting of the Region

The geological units of Elâzığ province, starting from the oldest to the youngest, are listed as:

- Keban metamorphites consisting of Permo Triassic aged crystallized limestones,

- Elâzığ Magmatites consisting of senonian aged granite, granodiorite, basalt, basaltic pillow lava, andesite and dacite dykes and volcanosedimanter rocks,
- Harami Formation consisting of Upper Maestrichtian aged massive limestones,
- Kırkgeçit Formation consisting of Middle Eocene-Upper Oligocene aged conglomerate, sandstone, marl and limestones,
- Mine Complex consisting of sedimentary rocks such as mudstone, sandstone, claystone and magmatic rocks such as basalt, andesite and diabase,
- Karabakır Formation, consisting of upper Miocene-Lower Pliocene aged tuff, agglomerate, basaltic lava and lacustrine limestones with lateral transition.

Figure 2.4 shows the geological map of the province. Units will be discussed in the next sections as compiled by Aksoy (1993), Avşar (1983) and İnceöz (1983).

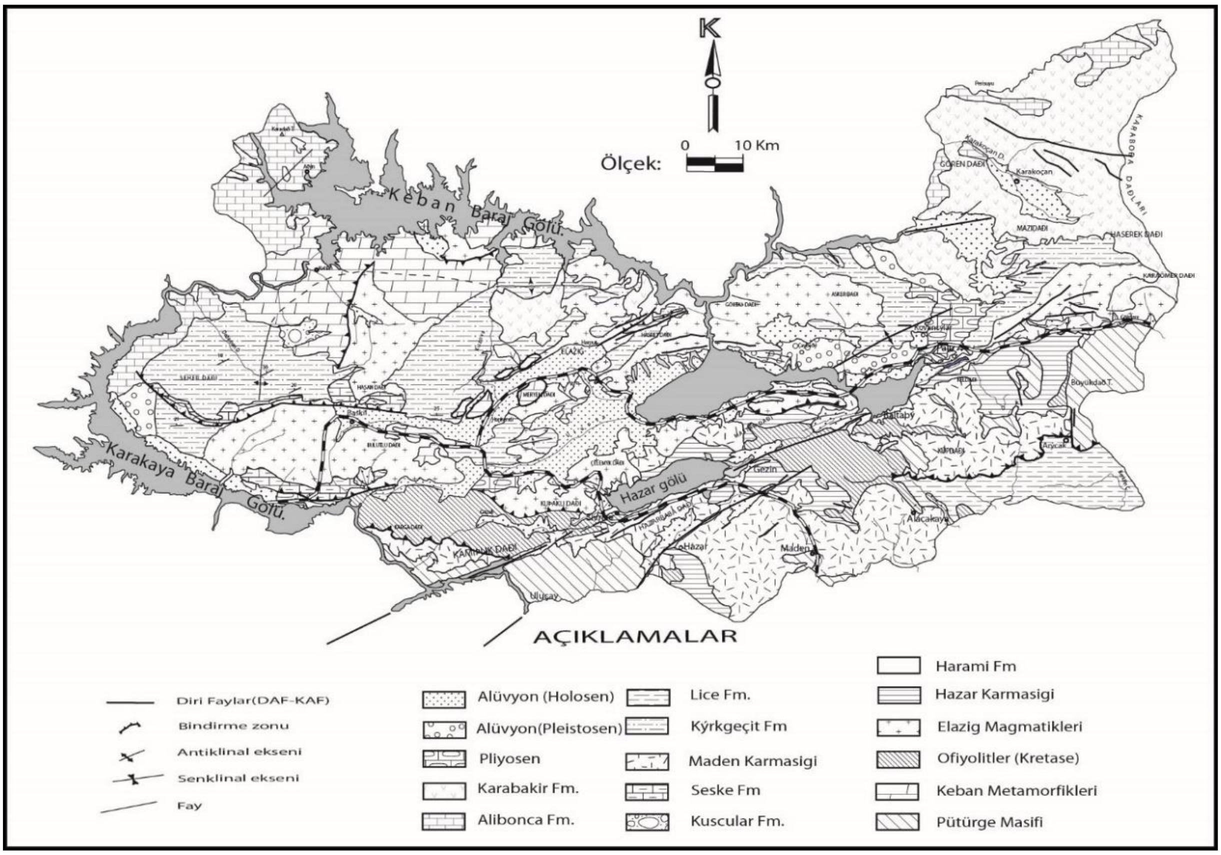

Figure 2.4 Geological map of Elâzığ province (Palutoğlu, M., Tanyolu, E., 2006, in Turkish)

2.3.1 Keban Metamorphics

Keban metamorphics in Elâzığ, is mostly located in the area between Abdullahpaşa-Sarıçubuk districts and Allahuekber Hill, and on the skirts of Mount Meryem southwest of Sürsürü district. It is covered by angular unconformities of Kırkgeçit Formation and exhibits unconformity with Karabakır Formation at the foot of Mount Meryem in the area between Abdullahpaşa, Cumhuriyet Sarıçubuk districts, and Allahuekber Hill.

Keban Metamorphics consist of recrystallized limestones-calcschist, marble, metaconglomerate-calcillites, but are mostly represented by recrystallized limestones in the study area.

2.3.2 Elâzığ Magmatites

Elâzığ Magmatites are sub-divided into magmatic rocks and Volcano-sedimentary rocks. Magmatic rocks are located in the west of Harput, north of Fevziçakmak, Esentepe and Safran districts, at the north of Fırat University, Cumhuriyet and Abdullahpaşa districts, about 1 km east of Şahinkaya Village, Yeniköy and Yadigâr districts, and in the vicinity of Keklik and Karataş hills. Volcano-sediments are usually located in between Eski Beyyurdu-Karşıyaka districts.

Keban Metamorphics tectonically overlie Elâzığ Magmatites, whose base is not visible in the central settlement area of Elâzığ province, and in accordance with Harami Formation, Kırkgeçit and Karabakır formations are angular unconformity. Elâzığ Magmatites are lithologically composed of gabbro-diorites at the base, basaltic-andesitic volcanic rocks, and volcano-clastics overlying them, and granodiorite-tonalites and dacite dykes cutting them.

2.3.3 Harami Formation

Harami formation exists as a few hundred square-meters pockets in the north, south and east of Harput. The unit covering Elâzığ Magmatites is covered by Kırkgeçit Formation generally represented by massive limestones. This unit consists of lenticular red conglomerate and sandstone at the bottom, sandy limestone and massive limestone at the lower levels. Formation environments are shallow, clear, not widespread, disconnected and exhibit recifal characteristics. Harami Formation was deposited in a narrow and shallow basin in Maastrichtian. Red conglomerates and sandstones at the base are terrestrial deposits with fan delta character. The sandy limestone and limestones overlying them are carbonate deposits, deposited in shallow sea. According to paleontological findings, it is Maastrichtian or older.

2.3.4 Kırkgeçit Formation

The Kırkgeçit Formation, which extends to the city of Van, is mapped in three different lithological columns. Sandstone-marl units outcrop in the north of Virane district, northeast and northwest. The conglomerate-sandstone is observed in the vicinity of Sarıçubuk and Şahinkaya Villages and Körpınar district, in the north of Cumhuriyet and Zafran districts, in the north and northeast of Harput, and the Marn units in the north of Akyazı and Virane districts, and about 1 km to the north. The sandstone-marl layers are interchangeable and bear conglomerate levels.

2.3.5 Karabakır Formation

Karabakır formation is mapped in three geological units: volcanics, limestone and conglomerate-sandstone. Volcanic rocks are located about one km east of Yeniköy, and west of Yadigâr districts. Limestone member can be seen in the vicinity of Rızvan and Baz Hills and west of Doğukent, Salıbaba, Çatalçeşme districts. The conglomerate-sandstone lies in the north and northeast of Yeniköy District, around Yadigâr District. Karabakır Formation covers the Keban Metamorphics, Elâzığ Magmatites and Kırkgeçit Formation unconformity. There are also unconformity Pleistocene aged alluviums. The age of the Karabakır formation is the Upper Miocene according to its paleontological findings.

2.3.6 Alluvium

Alluvium sediments, which spread over large areas, are mapped in three separate units. Due to their different lithologies they are classified as silty clay, sandy gravelly-clay and sand-gravel.

Silty clay dominates the southeast of Sürsürü, Kültür, Olgunlar, Hicret, Akpınar, Sarayatik, Nailbey, University and Çarşı districts.

Sandy gravelly clays are mapped in the Sanayi district, south of Kırklar district, in the middle and north part of İzzetpaşa district, Yeni district, south and east of Fırat University campus, south, north and northwest of Sürsürü district, east of Abdullahpaşa district and in the south, near the north of Yadigâr district, in the direction of Aksaray district.

The sand-gravel layer is in the north and northwest of Abdullahpaşa district, south of Cumhuriyet district, in Ulukent, Yıldızbağları, Rızaiye, İcadiye, Mustafapaşa, Rüstempaşa, Aksaray, Kızılay, Gümüşkavak and north of Sanayi districts. It is also observed in Çatalçeşme, Doğukent districts between Salıbaba-Karşıyaka districts. The sand-gravel proportions vary from district to district with also variable clay layer thicknesses.

Figure 2.5 shows the geological units mapped in the vicinity of Elâzığ city center, along with representative cross-sections, as explained in the preceding subsections. Also Figure 2.6 presents the generalized stratigraphic columnar section representing Elâzığ geological setting.

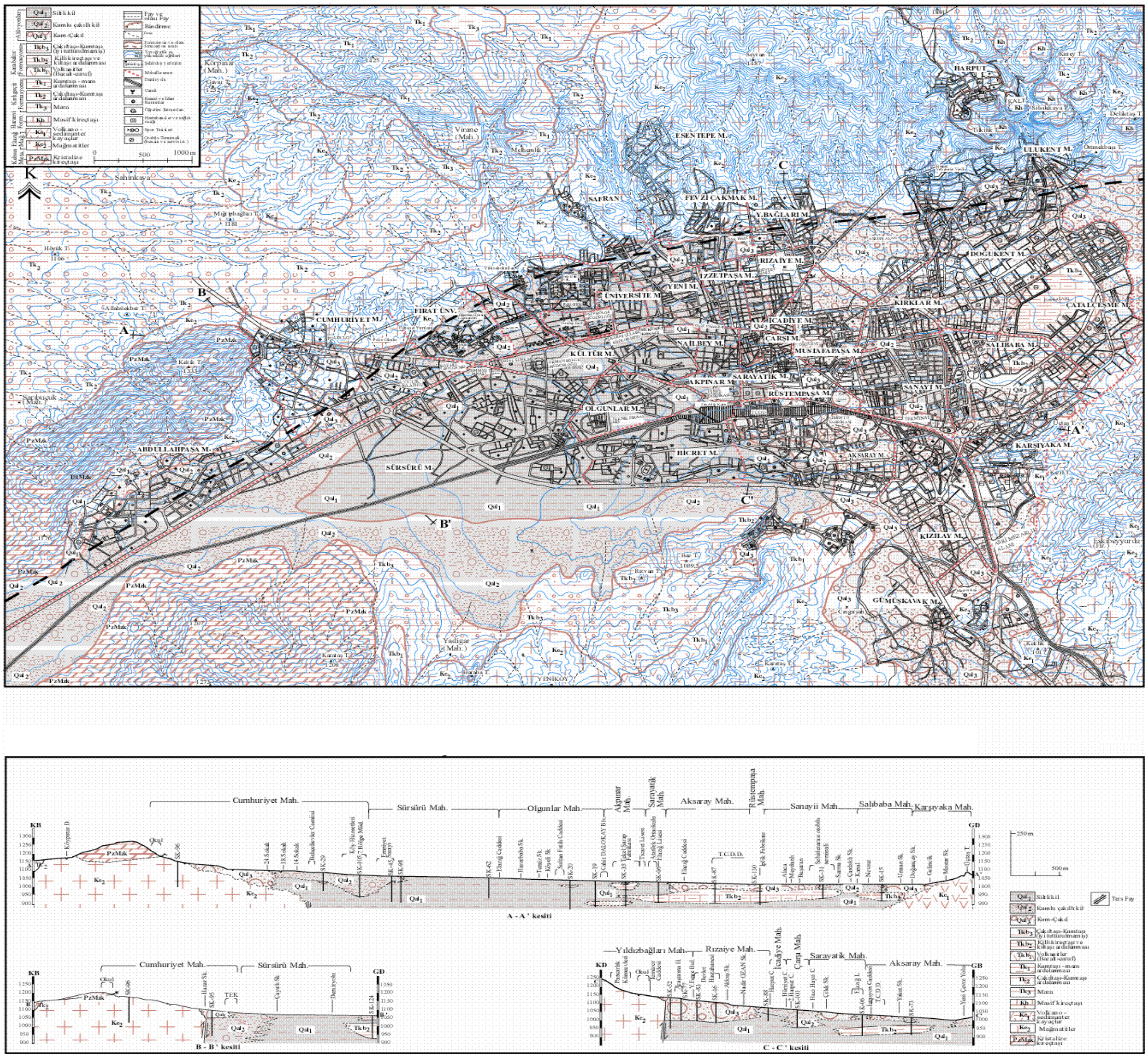

Figure 2.5 Geological map of Elâzığ City Center (Palutoğlu, M., Tanyolu, E., 2006)

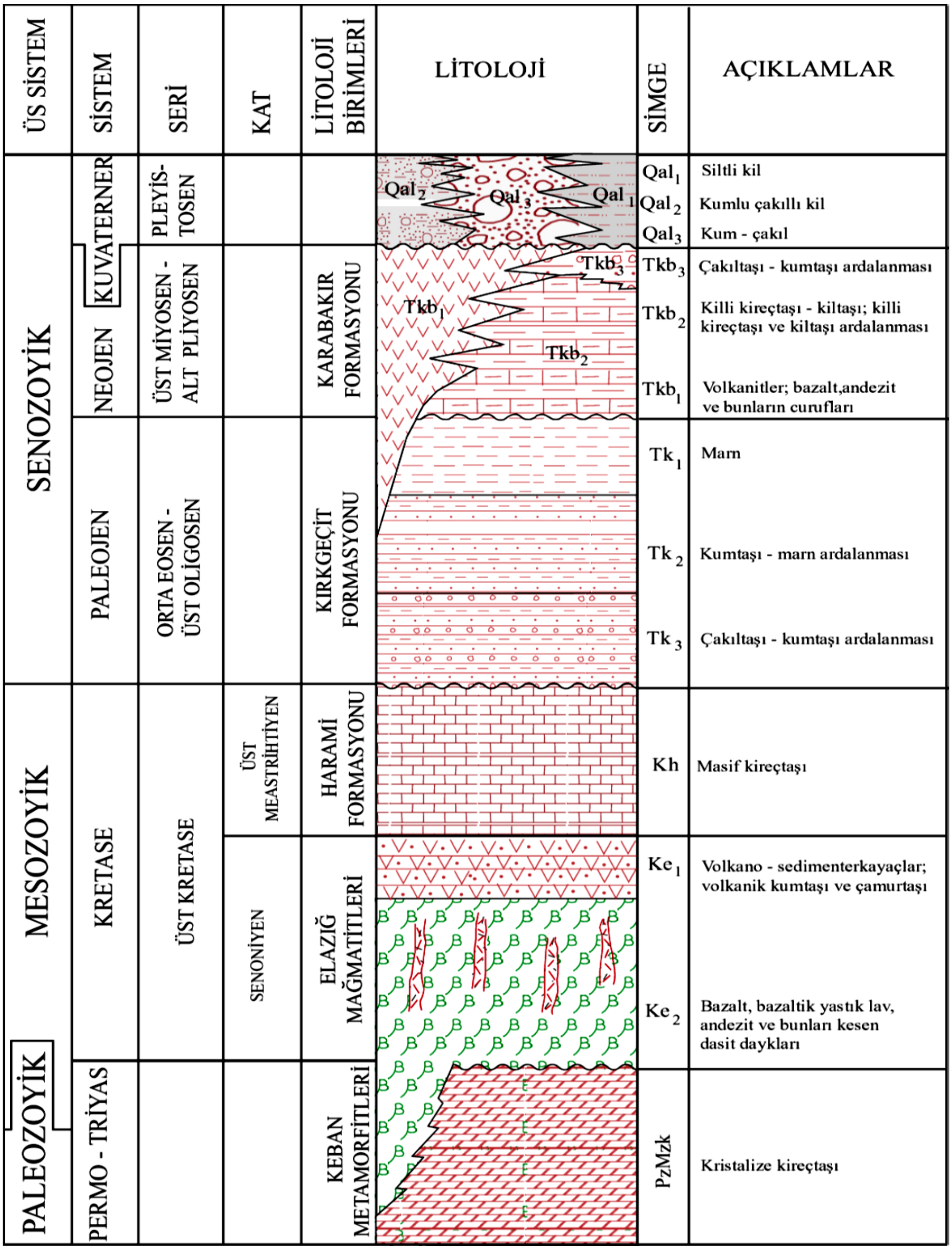

Figure 2.6 Generalized stratigraphic columnar section of Elâzığ
(Palutoğlu, M. and Tanyolu, E., 2006)

Chapter 3
Seismological Setting and Strong Ground Motion Characteristics

Prof. Kemal Önder ÇETİN[1]

Prof. Ayşegül ASKAN GÜNDOĞAN[1]

Prof. Zeynep GÜLERCE[1]

Inst. Shaghayegh KARİMZADEH NAGHSHİNEH[1]

Res. Asst. Makbule ILGAÇ[1]

Res. Asst. Gizem CAN[1]

Res. Asst. Elife ÇAKIR[1]

Res. Asst. Berkan SÖYLEMEZ[1]

Abdullah ALTINDAL[1]

[1] *Middle East Technical University*

3.1 Introduction

On January 24, 2020 at 8.55.11 p.m. local time (UTC 5.55.11 p.m.), a destructive earthquake occurred on the East Anatolian Fault Zone (EAFZ) due to the rupture of the fault with a left lateral strike slip source mechanism more specifically along the Pütürge segment extending in the NE-SW direction. The earthquake was reported with a moment magnitude M_w=6.8 according to the Disaster and Emergency Management Presidency (AFAD) and a moment magnitude M_w=6.7 according to the United States Geological Survey (USGS). The epicenter was located at N38.3593°, E39.0630°, approximately 37 km SSW of Elâzığ and 64 km east of Malatya with the focal depth of 8.06 km according to AFAD.

3.2 Seismological Characteristics of the Earthquake

EAFZ is a NE-SW striking, left-lateral intra-continental strike slip fault system that extends between the Karlıova junction and Antakya at the NE corner of Mediterranean Sea (Şaroğlu et al., 1992). Duman and Emre (2013) proposed seven segments with segment lengths ranging between 31 and 113 km for the EAFZ master fault strand which is adopted in the Updated Active Fault Maps of MTA as well (Emre et al., 2013). Two separate segments are defined by Duman and Emre (2013): the Palu segment between Palu and Lake Hazar and the Pütürge segment between Lake Hazar and Sincik separated by the Lake Hazar releasing bend. The rupture zone of the 2010 Elâzığ-Kovancılar earthquake (M_w=6.1) coincided with the Palu segment; whereas, the rupture zone of this event is associated with the Pütürge segment (Figure 3.1). The causative fault of the 2020 event is considered to have increased stress levels due to the 2010 Kovancılar earthquake (Akkar et al., 2011).

According to the preliminary report of field observations published by MTA, surface deformations related to this earthquake was observed for approximately 48 kilometers, starting from the Hazar Lake down to Pütürge (Malatya). These observations are consistent with the spatial distribution of the aftershocks shown in Figure 3.2. Therefore, the approximate rupture plane defined by the surface deformations given in the preliminary MTA report is considered in this report to calculate the source-to-site distance.

3.3 Source Characteristics of the Event

The mainshock focal mechanism solutions provided by AFAD and USGS are shown in Table 3.1. They both provide planes that prove left lateral strike slip motions as dominant source mechanisms consistent with the regional tectonics and the properties of the causative fault. Additionally, geometric distribution and focal mechanism solutions of the aftershocks with moment magnitude values ranging between 4.0-5.1, are also shown in Figure 3.3.

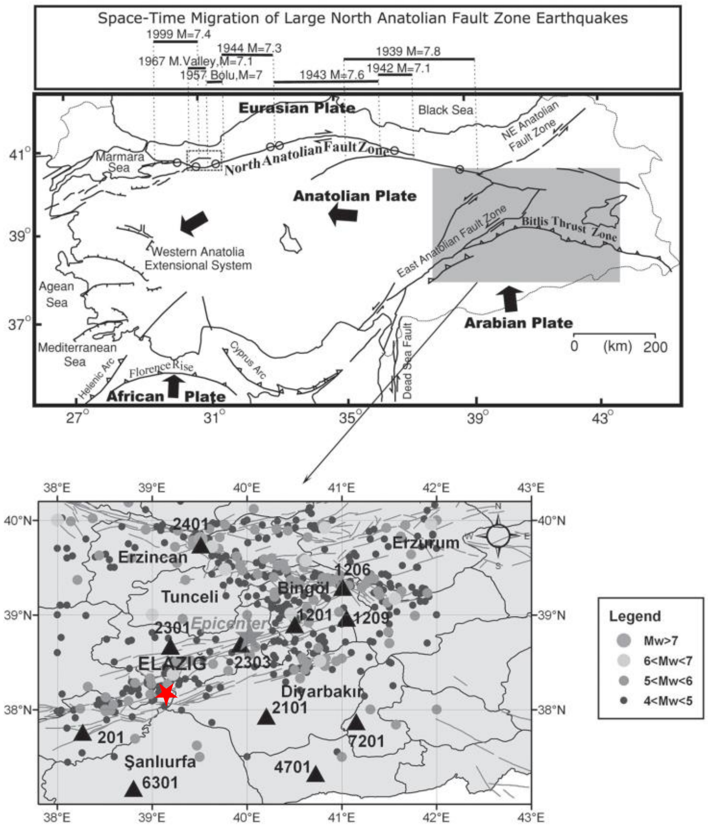

Figure 3.1 Major tectonic structures and epicenters of the 2020 (red star) and 2010 (grey star) earthquakes along with seismicity within the last century (Figure is modified from Akkar et al., (2011))

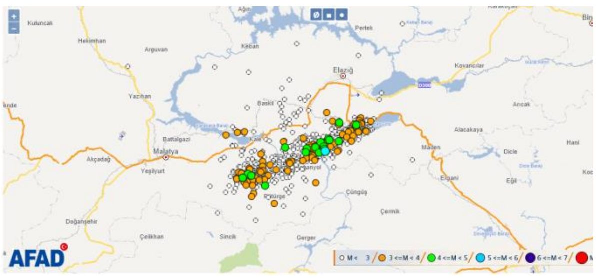

Day 1

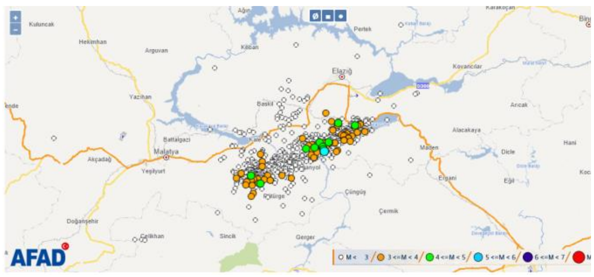

Day 2

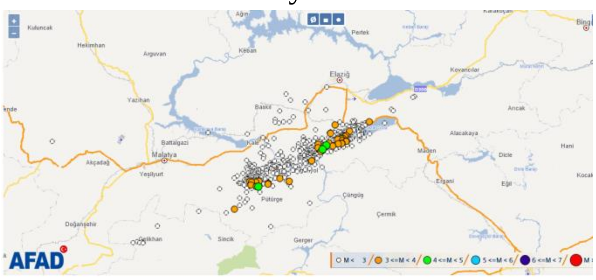

Day 3

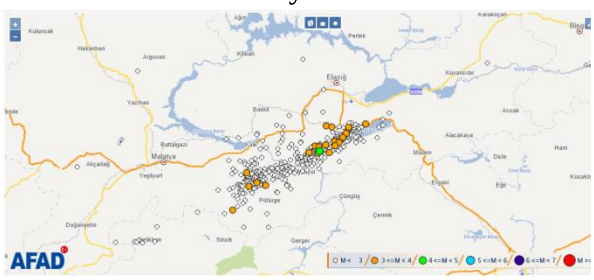

Day 4

Figure 3.2 Spatial distributions of the aftershocks between 24/01/2020-28/01/2020 (https://deprem.afad.gov.tr/ddakatalogu)

The mainshock was followed by 1948 aftershocks with magnitudes ranging in between 0.8 and 5.1, within 10 days after the event. The focal depths of the aftershocks are mostly concentrated in between 5-20 kms from the ground surface consistent with the seismogenic depth of the region (Figure 3.4).

3.4 Preliminary Analysis of Recorded Strong Ground Motions

The mainshock is recorded by 66 strong ground motion stations according to the preliminary report published immediately after the event by AFAD. In the preliminary report, only three-component peak ground accelerations (PGA) recorded by five nearby stations were provided. Up this date, the waveforms or the response spectra of the recordings were not disseminated to the public by AFAD. Therefore, a detailed analysis of the strong motion characteristics is not included in this report. On the other hand, provided PGA values are useful for the preliminary and comparative analysis of recorded ground shaking levels with the current ground motion prediction equations (GMPEs) and the design PGA values provided in the recently-updated Turkish Seismic Hazard Map (2018).

Table 3.2 provides the PGA values recorded in this event that are gathered from AFAD's preliminary report. Fortunately, the shear wave velocity profiles for all stations are available: the time-averaged shear wave velocity at the first 30 meters (V_{S30}) for Pütürge (ID#4404), Center (ID#2301), and Maden (ID#2302) stations are measured by Sandıkkaya et al. (2010) and disseminated through http://kyhdata.deprem.gov.tr (last accessed January 31, 2020). The V_{S30} values of the other two stations, Sivrice (ID#2308) and Gerger (ID# 0204), are taken from the final report of a recently finalized project funded by AFAD (Kurtuluş et al., 2019). These values are also provided in Table 3.2. To compare the distance attenuation of the recorded strong ground motions with the distance scaling of current GMPEs, the recorded values are normalized to V_{S30} = 400 m/s by using the site amplification scaling utilized in each model. Rupture (R_{RUP}) and Joyner-Boore (R_{JB}) distances given in Table 3.2 are calculated by using the fault plane shown in Figure 3.5. Because the termination points at both ends of the rupture plane are still controversial, the source-to-site-distance metrics for Sivrice and Maden stations include a certain degree of uncertainty.

Abrahamson et al. 2008 (ASK08) from NGA-West GMPE's is used along with the appropriate distance metrics and site conditions to predict the peak ground accelerations (PGA). Figure 3.6 shows the geometric mean of the recorded PGA values as compared with the GMPE predictions for $V_{s,30}$=200, 350, 500 and 1100 m/s. Based on these comparisons, it is concluded that the recorded PGA values are in conformance with the predictions of Abrahamson et al GMPE. According to Wells and Coppersmith (1994) relationship, the length of the rupture is estimated as to vary in the range of 40-60 km consistent with the field and aftershock observations. This value is also compatible with the regional characteristics of the local tectonic environment, as stated in Gulerce et al. (2017).

Table 3.1 Moment tensor solution by AFAD and USGS

AFAD	Strike 1	Dip 1	Rake 1	Strike 2	Dip 2	Rake 2
	248	76	1	158	89	166
USGS	Strike 1	Dip 1	Rake 1	Strike 2	Dip 2	Rake 2
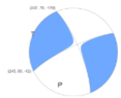	337	78	-170	245	80	-12

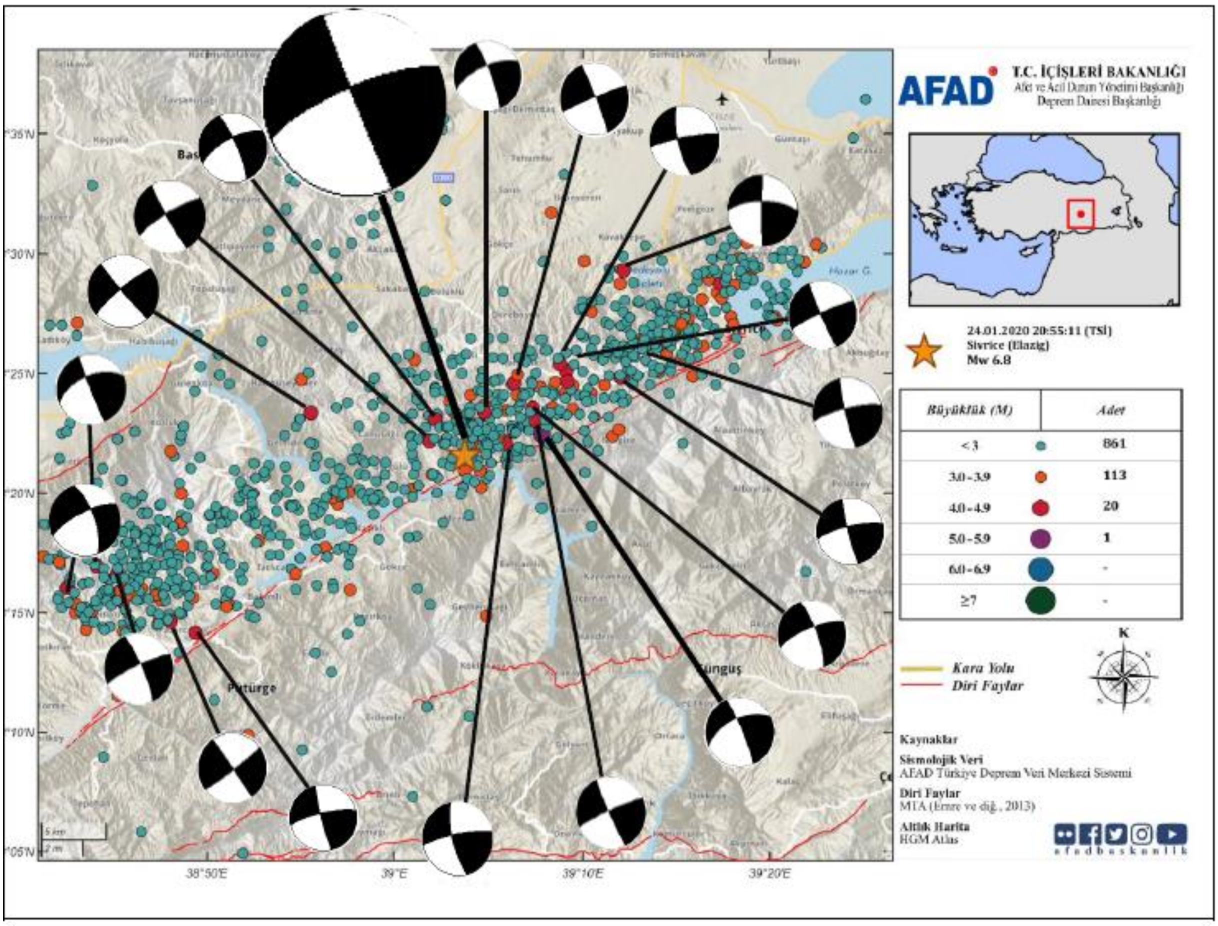

Figure 3.3 24/01/2020 Malatya-Elâzığ Earthquake M_w=6.8 and aftershock distribution along with focal mechanism solutions given by AFAD.
(https://deprem.afad.gov.tr/)

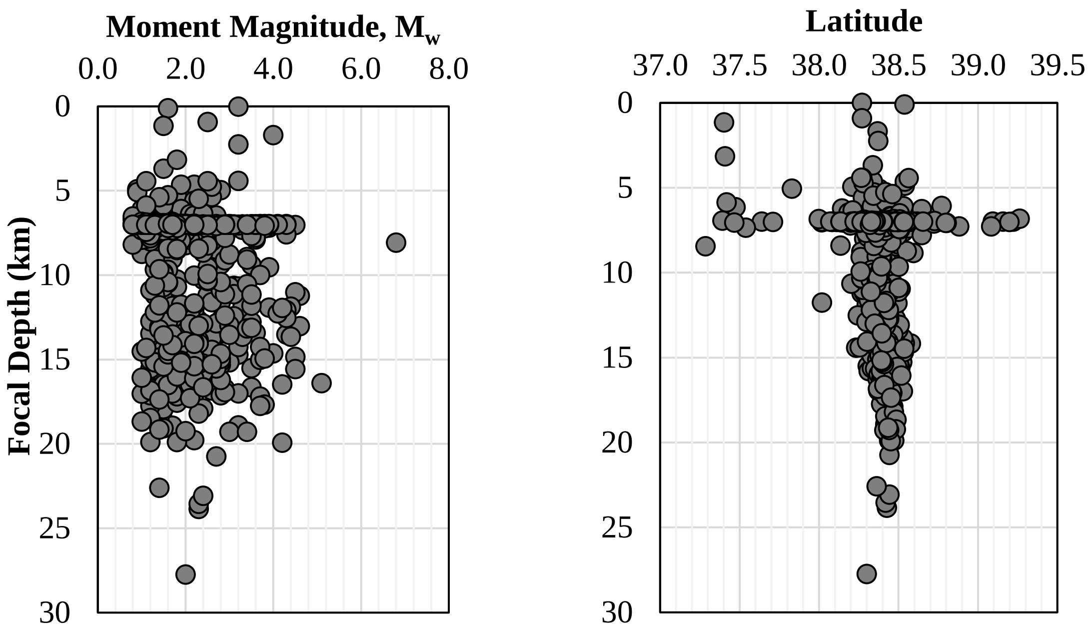

Figure 3.4 M_w vs. focal depth scatters recorded between January 24 to February 03, 2020 following the mainshock of 2020 Elâzığ-Sivrice Earthquake (AFAD)

Table 3.2 Strong Ground Motion Stations and Recorded PGA values (AFAD)

Stations				**Measured Acceleration Values (gals)**			***R_{rup} (km)**	***R_{jb} (km)**	**V_{s30}** (m/s)**
Station Code	**Town**	**Latitude**	**Longitude**	**N-S**	**E-W**	**U**			
2308	Sivrice	38.451	39.310	238	292.8	190.1	1.76	1.45	450
4404	Pütürge	38.196	38.874	207	239.2	153.9	5.49	5.4	1380
204	Gerger	38.029	39.035	94	110.1	60.8	28.62	28.6	555
2301	Center	38.670	39.193	119	140.7	66.3	27.87	27.85	407
2302	Maden	38.392	39.675	26.3	34	22.8	31.27	31.25	907

* Estimated based on the approximate location of the rupture plane based on the preliminary MTA report.

** Adapted from AFAD Ground Motion Station

The geometric mean of the PGA values for the closest five stations to the zone of energy release are compared with the predicted median values obtained by ASK08. Figure 3.6 shows the calculated PGA values at different distances as compared to the values recorded at strong ground motion stations. Based on these comparisons, it is concluded that despite slightly lower values recorded at Sivrice and Maden stations, the PGA values are roughly in good agreement with the predictions of GMPE. The discussions and interpretations will be enriched when strong ground motion records and station data become publicly available.

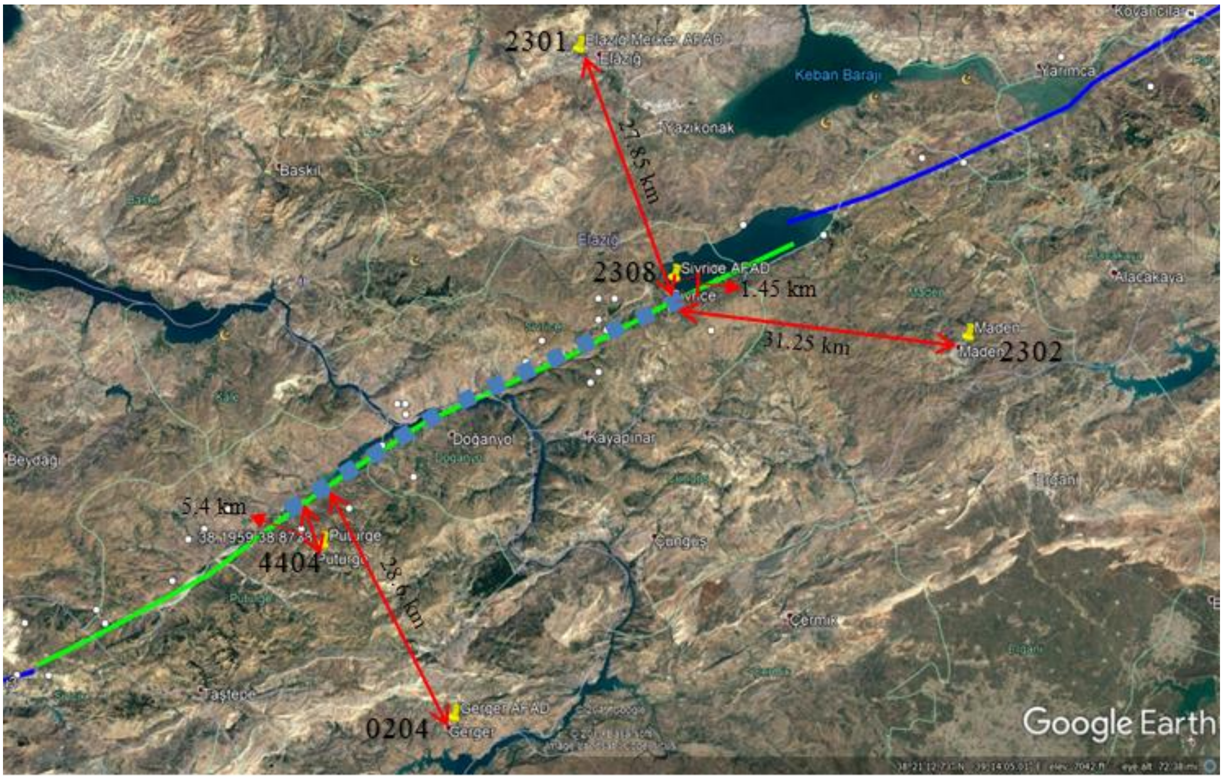

Figure 3.5 Locations of the five strong motion stations included in the AFAD's preliminary report.

R_{JB} values are approximately estimated according to the surface rupture given in MTA report (blue dashed line). Blue and green lines are the Palu and Pütürge segments that are slightly modified for their termination points by Gülerce et al. (2017)

A recent study by Kale (2019) has utilized several ranking methods for comparing the predictive performance of GMPEs for shallow crustal and active tectonic regions with the Turkish strong motion database. Analyses results indicated that the regional Kale et al. (2015) model, Turkey-adjusted version of the Boore and Atkinson (2008) model (Gülerce at al., 2016) and the global Chiou and Youngs (2014) model have better predictive performance among the other alternatives. Based on these findings, the normalized PGA values from this event are compared with the predictions lying in the median±1σ range given by TR-adjusted Boore and Atkinson (2008), TR-adjusted Chiou and Youngs (2008), Boore at al. (2014), Chiou and Youngs (2014) and Kale et al. (2015) in Figure 3.7. According to Figure 3.7, the PGAs recorded in Pütürge, Gerger and Elâzığ Center stations are equal to or very close to the median estimations of the tested GMPEs. The PGA values recorded at the Sivrice recording station, which is the closest location to the epicenter, are lower than the median estimations of Kale et al. (2015) and are approximately one standard deviation lower than the median estimations of the other GMPEs. Similarly, the PGA value recorded at Maden station is significantly lower than the median estimations, lying outside the median±1σ range of each model. These findings are consistent with the distance attenuation plots given in Akkar et al. (2011): faster attenuation of waves due to low quality factor values in the region beyond 100 km was observed in the recorded ground motions of the 2010 Elâzığ-Kovancılar Earthquake. The amount of data at the locations beyond 30 km distance is currently very limited; therefore, the discussions and interpretations given here will be further elaborated when the strong ground motion records are publicly available.

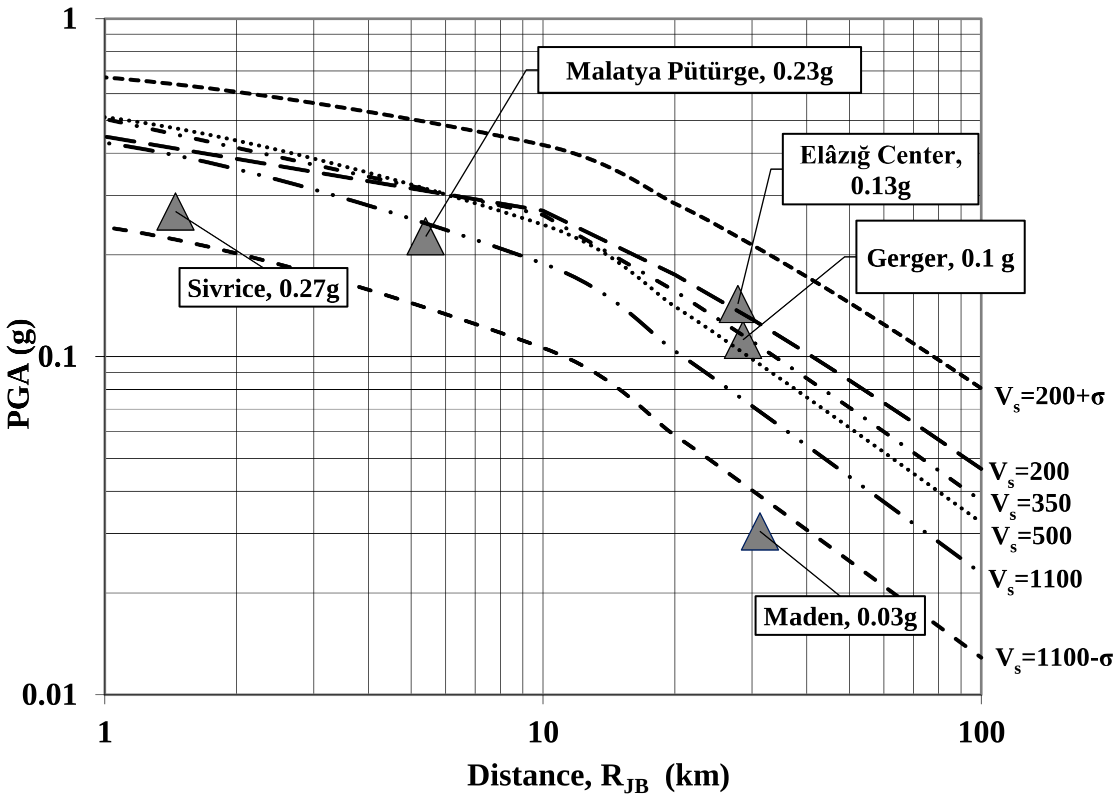

Figure 3.6 Comparison of the PGA values at different distances estimated by ASK08 to the recorded PGA values at the SGM Stations

The Turkish Seismic Hazard Map (TSHM) was updated in 2018 (Akkar et al., 2018) and is enforced by the updated Turkish Building Earthquake Code (TBEC, 2019) to obtain the design spectrum of regular buildings since the beginning of 2019. The short period ground motions (S_{DS}) with 50% and 10% chance of exceedance in 50 years (72 and 475 years return period, respectively) are downloaded from https://tdth.afad.gov.tr (last accessed in Feb 11, 2020) for each station as shown in Figure 3.8 and presented in Table 3.3. To calculate the S_{DS} values, the site classifications given in Table 3.2 are considered and the PGA values at the same hazard level are calculated by taking 40% of SDS.

TSHM suggests that the PGA values for 475-years and 72-years return periods are equal 0.722g and 0.277g respectively for Sivrice station with the closest distance to the fault plane. Maximum accelerations recorded in this station (0.3g) is significantly lower than the PGA for 475-years return period and close to but slightly higher than the PGA for 72-years return period. A similar observation is valid for the Pütürge station as well. For the other stations with higher source to site distances, recorded maximum accelerations are smaller than the PGA suggested by TSHM for 72-years return period. As a result of these inferences, it is clearly seen that the Elâzığ event is less severe than the design level earthquake.

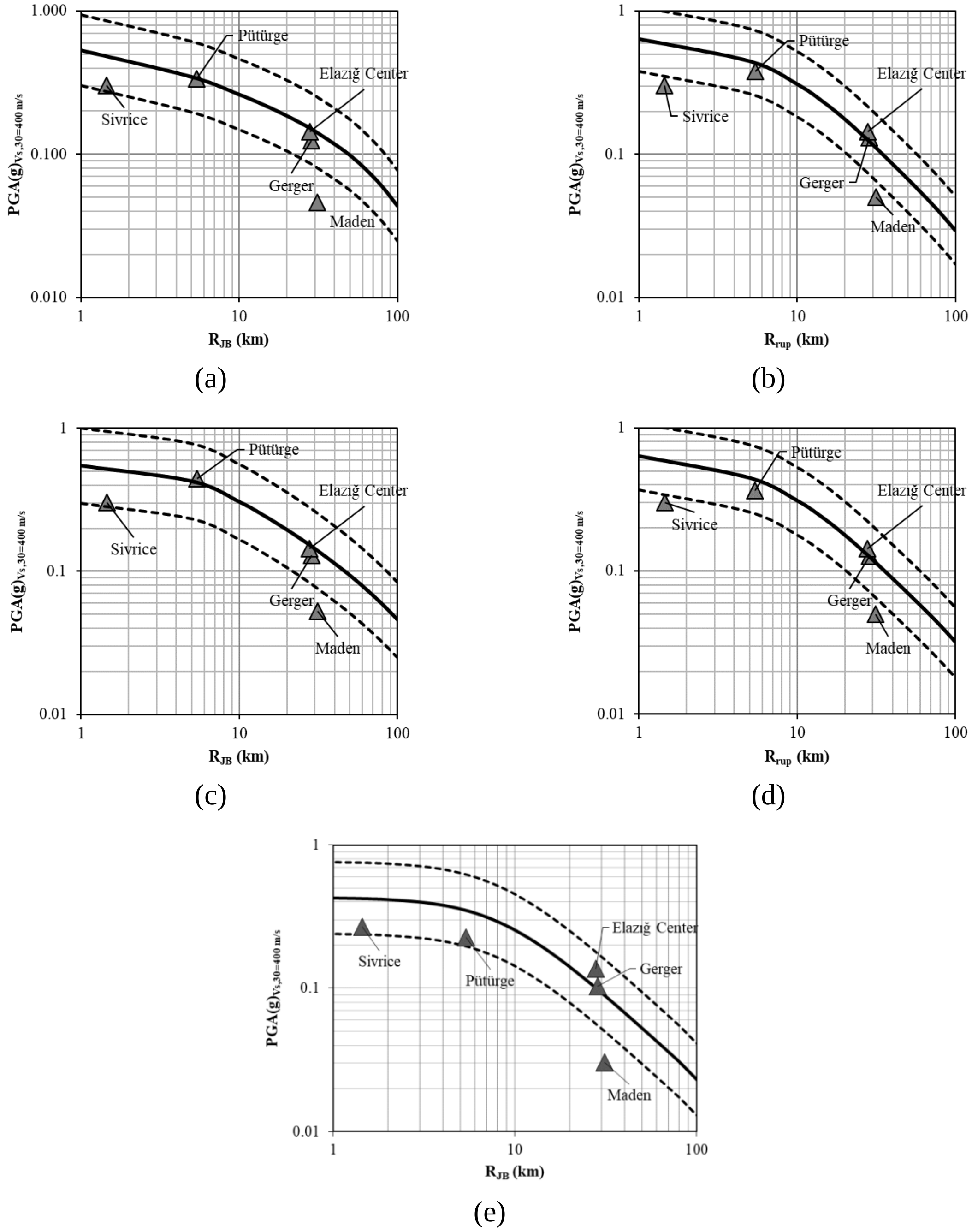

Figure 3.7 Comparison of the normalized geometric mean of recorded PGA values with the distance scaling of GMPEs for M_w=6.8, $V_{S,30}$=400m/s of a strike slip event (a) for TR-adjusted BA08, (b) for TR-adjusted CY08, (c) for BSSA14, (d) for CY14, (e) for Kale et al. (2015).

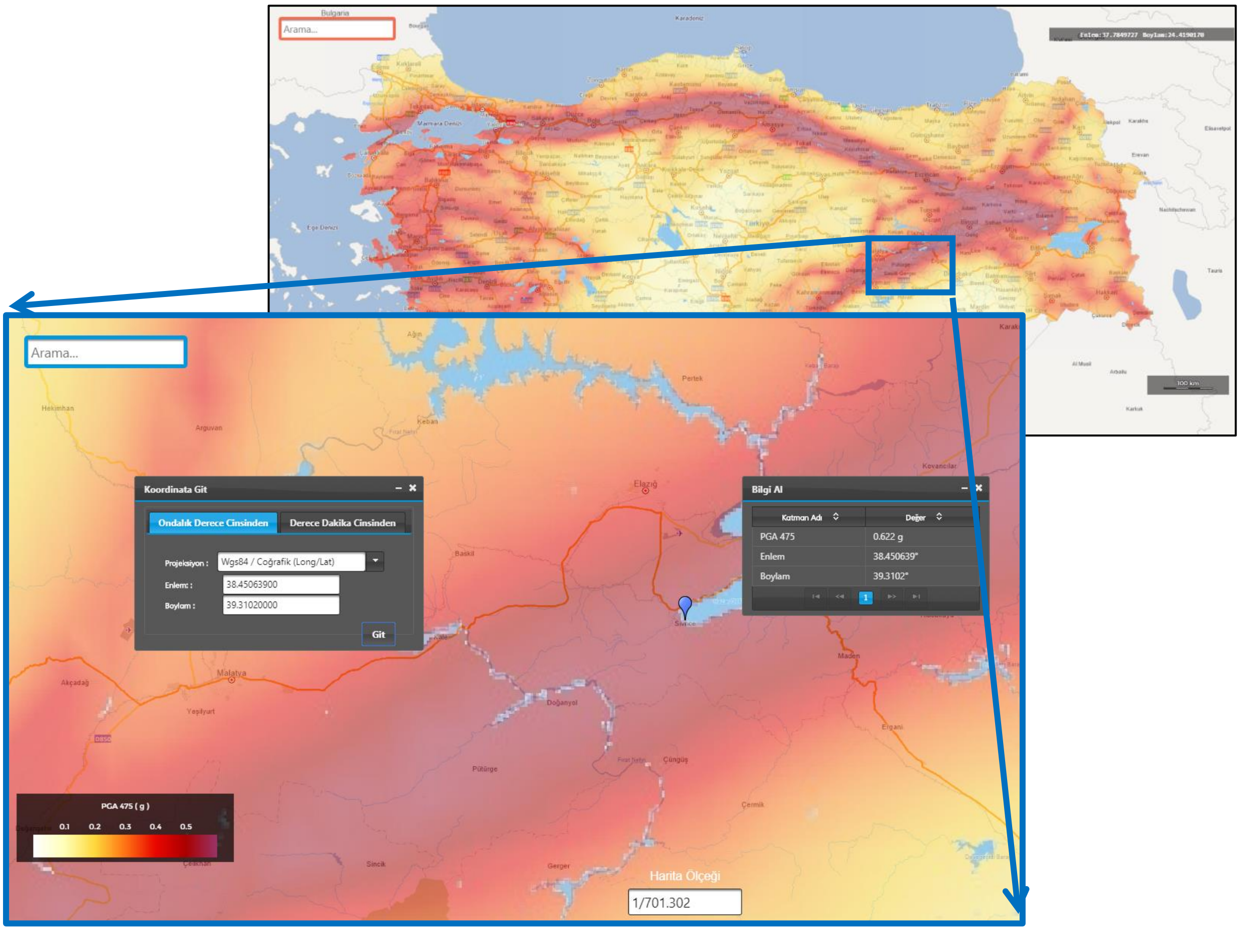

Figure 3.8 The Updated Turkish Earthquake Hazard Map (from https://tdth.afad.gov.tr). Elâzığ-Sivrice station (ID#2308) is pinned in blue color on the map and 475 years PGA value for that particular location is shown on the same figure.

Table 3.3 Strong Ground Motion Station Characteristics and Recorded PGA values

Station Code	**Site Class**	**$V_{s,30}$**	**PGA* (g)**	**72-year return period**					**475-year return period**				
				S_S	**S_1**	**S_{DS}**	**S_{D1}**	**PGA** (g)**	**S_S**	**S_1**	**S_{DS}**	**S_{D1}**	**PGA** (g)**
2308	ZC	450	0.3	0.539	0.126	0.692	0.189	0.277	1.504	0.396	1.805	0.594	0.722
4404	ZB	1380	0.24	0.548	0.122	0.493	0.098	0.197	1.578	0.403	1.42	0.322	0.568
204	ZC	555	0.11	0.344	0.085	0.447	0.127	0.179	0.883	0.233	1.06	0.35	0.424
2301	ZC	407	0.14	0.342	0.097	0.445	0.146	0.178	0.912	0.257	1.094	0.386	0.438
2302	ZB	907	0.04	0.428	0.107	0.385	0.086	0.154	1.148	0.306	1.033	0.245	0.413

* Maximum values of the recorded PGA's are reported

** Since PGA values that are compatible with field conditions are not available, the scaled S_{DS} value for field conditions is converted to PGA values approximately by multiplying S_{DS} with 0.4.

It must be noted that, without full acceleration waveform data, it is not possible to compute and comment on the spectral accelerations which are critical on the evaluation of the seismic performance of the structures in the region.

3.5 Spatial Distribution of Macroseismic (Felt) Intensity in the Region

One way to measure the anticipated levels of ground shaking is to employ macroseismic intensity values. Particularly, a spatial distribution of such values is valuable immediately after an earthquake to evaluate the effects of the earthquake. Even though, the macroseismic intensity values have certain degrees of uncertainty when compared to instrumental measures of ground motions, they are employed all over the world for immediate assessment of earthquakes, particularly to see the effects on built environment and humans. It is possible to prepare empirical iso-seismal maps on the field by observations on human response and building damage. Another alternative is to use correlations between intensity and peak or spectral ground motion parameters.

The closest city center, Elâzığ downtown, is approximately at 26.5 km from the zone of energy release, similarly Malatya and Adıyaman city centers are located 33.8 and 62.7 km away from the epicenter respectively. However, there are several smaller towns and villages in the fault vicinity probably experienced higher level of excitations. The preliminary intensity map in terms of Modified Mercalli Scale (MMI) by AFAD is shown in Figure 3.9. The values in this map are obtained by AFAD-RED system which employs correlations between MMI and strong ground motion parameters. The earthquake intensity map suggests that the maximum predicted MMI value is IX around the vicinity of the epicenter. Next, an estimated MMI map is shown in Figure 3.10 where MMI distributions are computed from the following empirical correlation (Bilal and Askan, 2014):

$$MMI = 3.884 \times \log(PGA) + 0.132 \tag{1}$$

To compute the PGA values, Kale et al. (2015) is employed followed by calibrations at the 5 stations where PGA values are known. Then, conversion to MMI is performed through Equation (1). After the ground motion data is made public, these efforts will be repeated for the entire dataset.

It is observed that very similar MMI values are computed in the study area. The distribution of the intensity values is consistent with the fault plane as well as the spatial distribution of damage observations in the field, particularly around the rural area. In addition, an observed MMI map is currently being prepared with the team efforts.

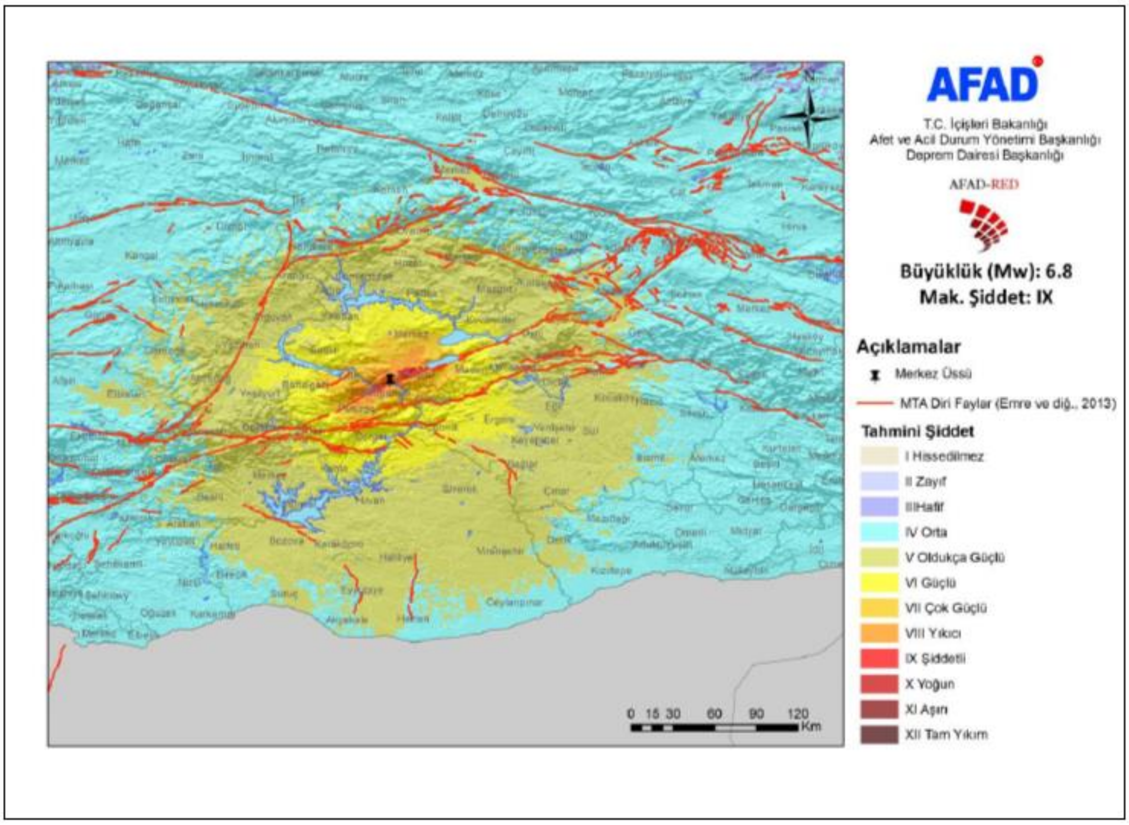

Figure 3.9 Preliminary Intensity Distribution given by AFAD

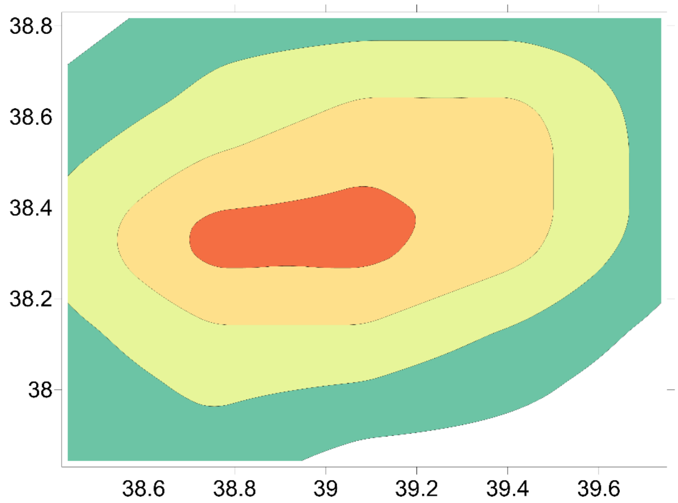

Figure 3.10 Computed MMI distributions using MMI-PGA correlations (Bilal and Askan, 2014)

Chapter 4
Geotechnical Reconnaissance Observations

Prof. Kemal Önder ÇETİN[1]

Asst. Prof. Mesut GÖR[2]

Res. Asst. Makbule ILGAÇ[1]

Res. Asst. Gizem CAN[1]

Res. Asst. Elife ÇAKIR[1]

Res. Asst. Berkan SÖYLEMEZ[1]

Faik CÜCEOĞLU

[1] *Middle East Technical University*
[2] *Fırat University*
[3] *General Directorate of State Hydraulic Works*

4.1 Introduction

This chapter discusses the preliminary geotechnical field observations made during and after the reconnaissance studies performed during the period of January 26-February 1st. After a brief introduction of the geotechnical conditions in Elâzığ Province, the field observations in the form of pictures and maps along with simple interpretations will be presented. On the path during reconnaissance studies, some structural performance observations were also made, which will be presented for documentation purposes. Detailed geotechnical discussion and interpretations including in-depth analyses will be the scope of future studies.

4.2 Downtown Elâzığ Soil Site Conditions

On the basis of available local geotechnical data, the geotechnical setting of downtown Elâzığ's most affected four districts namely, i) Mustafapaşa, ii) Şahinkaya, iii) Sürsürü, iv) Zafran will be discussed next. The available shear wave velocity measurements by Multi-Channel Surface Wave Analysis Method (MASW) along with Standard Penetration Test results establish the basis of these assessments. A generalized representative borehole is constructed for these districts as discussed in the following sections.

4.2.1 Downtown Elâzığ

4.2.1.1 Elâzığ- Mustafapaşa District

Several structurally damaged residential buildings were mapped in Elâzığ-Mustafapaşa district, which is located in the city center of Elâzığ city. Mustafapaşa district consists of Plio-Quaternary aged young sediments. Typical soil type observed in the district is classified as brown gravelly sandy clay. Groundwater table is typically observed at 15 meters. A representative lithology is presented in Figure 4.1. Shear wave velocity of the upper 30 m ($V_{s,30}$) for the region is estimated as 300-350 m/s by Multi-Channel Surface Wave Analysis Method (MASW). Note that the borelog given in Figure 4.1 reflects idealized soil conditions, which may not representative for the whole district.

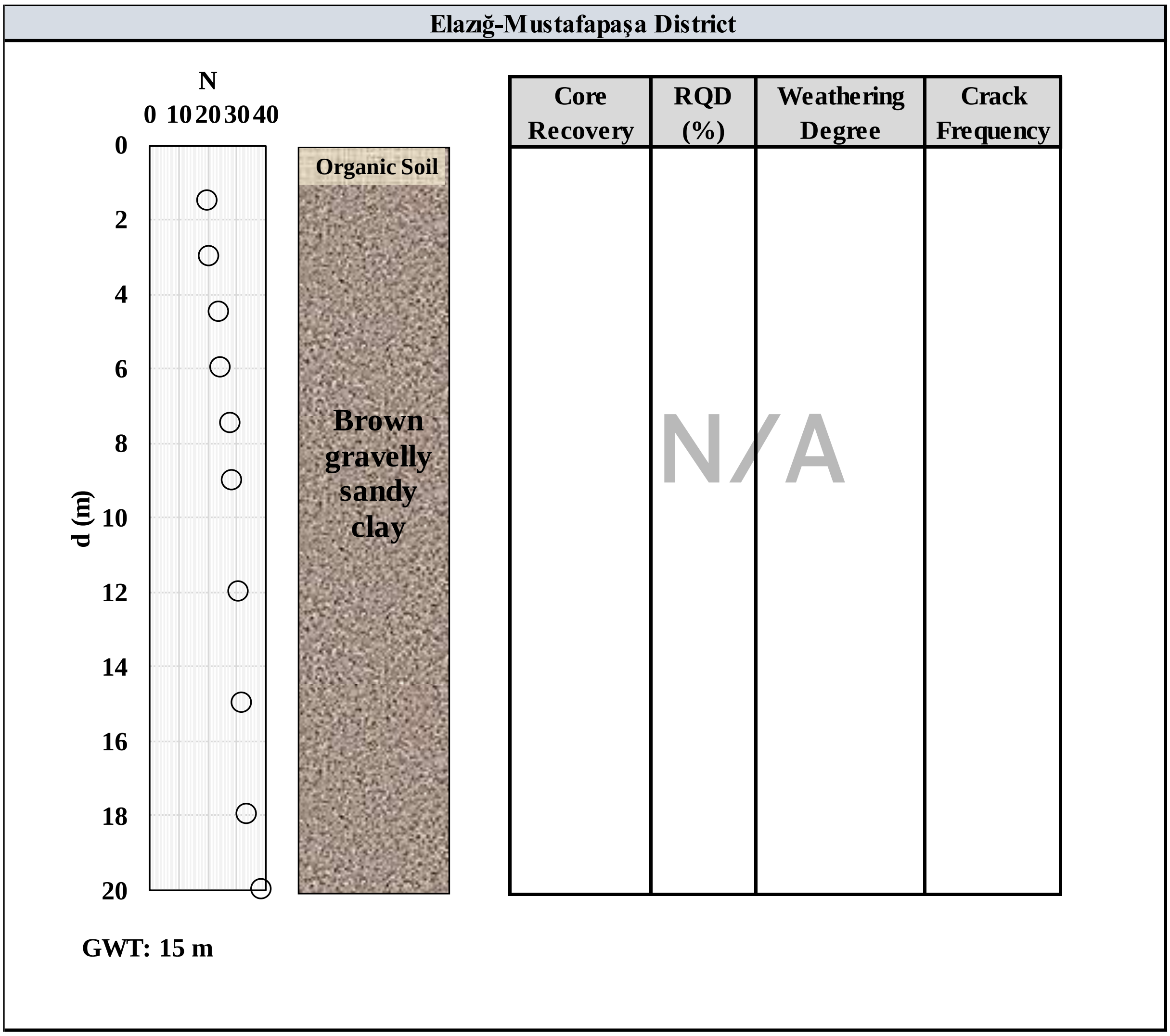

Figure 4.1 Typical Borelog for Elâzığ-Mustafapaşa District

4.2.1.2 Elâzığ- Şahinkaya District

In Şahinkaya district, again a concentration of structural damage has been observed. The district foundation soil/rock profile is composed of mostly weathered sandstone. The weathering and fracturing decreases with depth. Groundwater table is located at 6 meters. A representative soil/rock profile is presented in Figure 4.2. Shear wave velocity of the upper 30 m ($V_{s,30}$) for the district is estimated as 400-500 m/s by Multi-Channel Surface Wave Analysis Method (MASW).

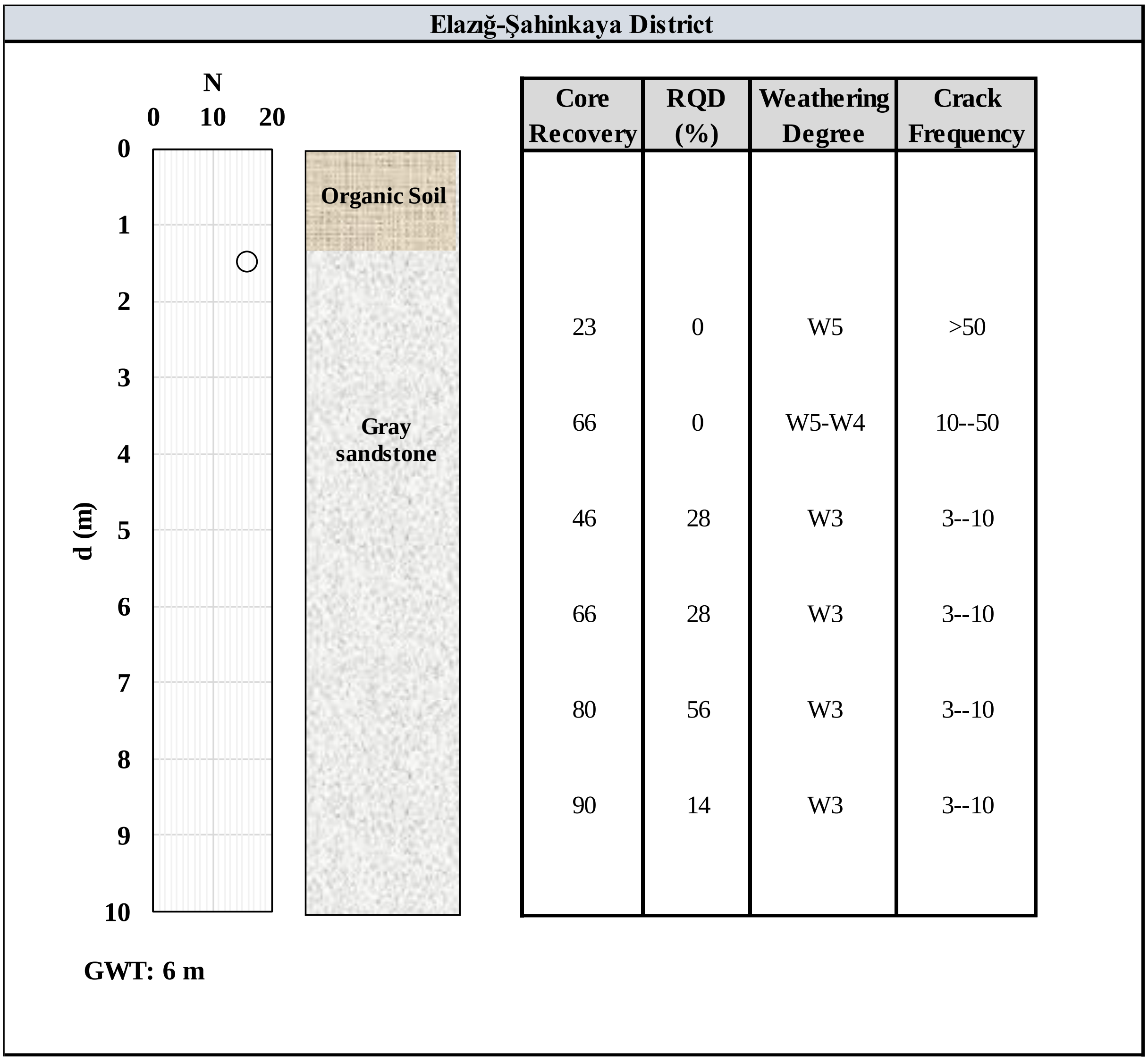

Core Recovery	RQD (%)	Weathering Degree	Crack Frequency
23	0	W5	>50
66	0	W5-W4	10--50
46	28	W3	3--10
66	28	W3	3--10
80	56	W3	3--10
90	14	W3	3--10

Figure 4.2 Typical Borelog for Elâzığ-Şahinkaya District

4.2.1.3 Elâzığ- Sürsürü District

The most of the structural damage had been concentrated in Elâzığ-Sürsürü district, where Plio-Quaternary aged young sediments dominate foundation profiles. The upper surficial layers are classified as brown gravelly sandy clay. Groundwater table is located below 15 m depth. Two representative lithology are presented in Figure 4.3. Shear wave velocity of the upper 30 m ($V_{s,30}$) for the region is estimated as 350-400 m/s by Multi-Channel Surface Wave Analysis Method (MASW).

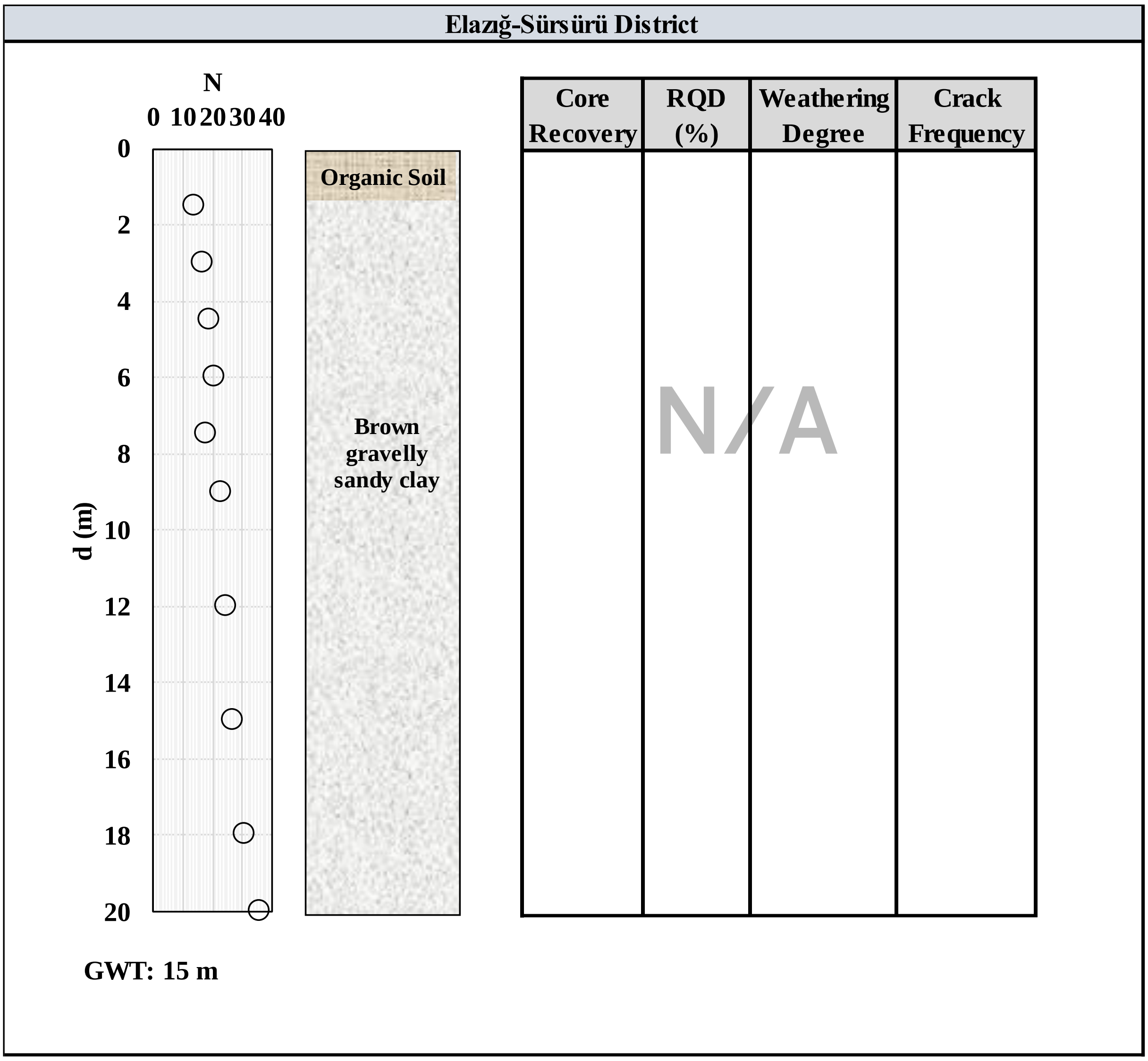

Figure 4.3 Typical Borelog for Elâzığ-Sürsürü

During the site visit, a field investigations study including borehole drilling, undisturbed and disturbed soil sampling with SPT measurements, was witnessed. The borelog of this study is retrieved by personal communication and is presented in Figure 4.4.

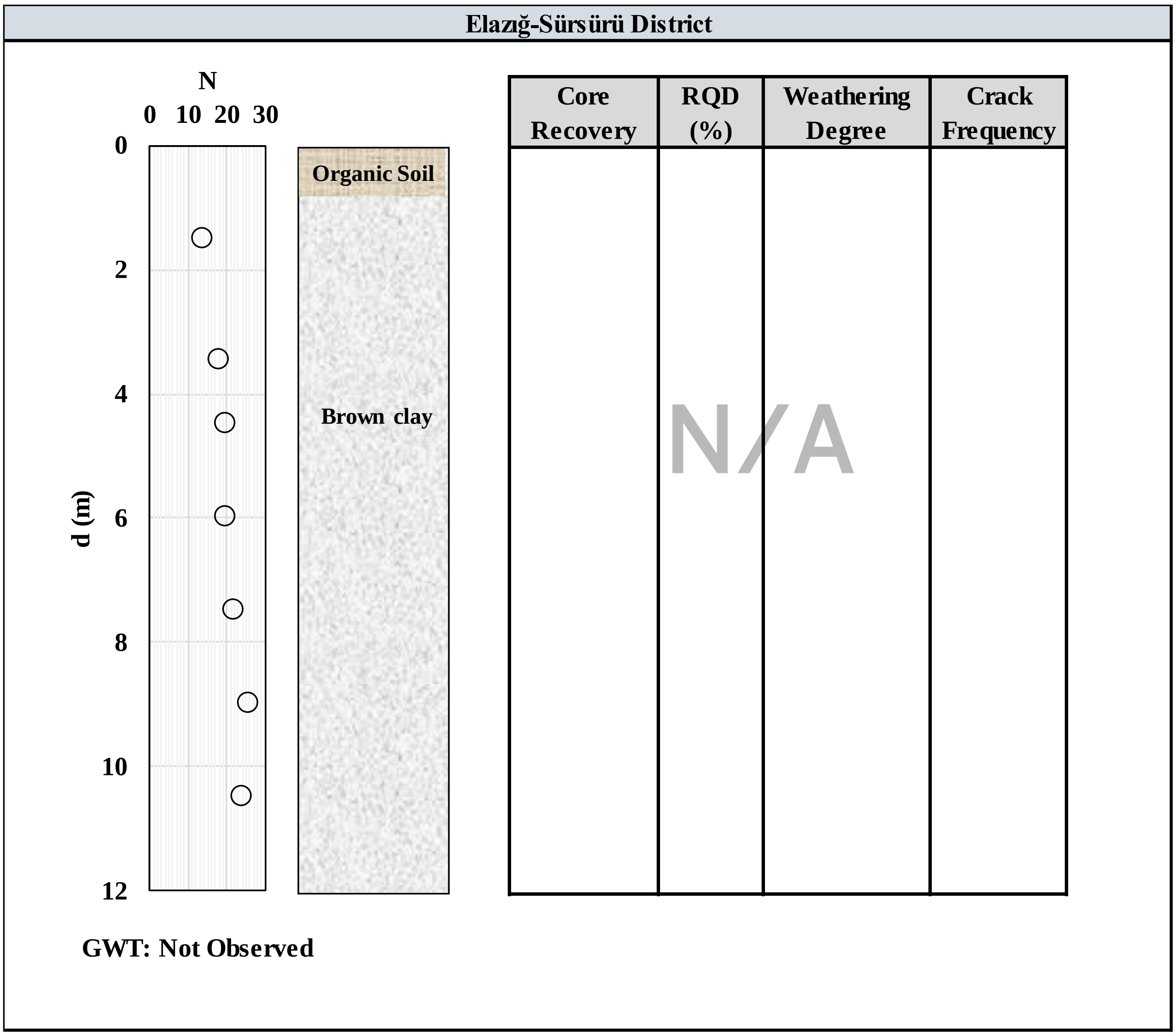

Figure 4.4 Typical Borelog for Elâzığ-Sürsürü District

4.2.1.4 Elâzığ- Zafran District

Mainly weathered and fractured gray-beige sandstone is observed in Elâzığ-Zafran District. The rock becomes relatively intact with depth. Groundwater table is observed to be deeper than 10 meters. A representative soil/rock profile is presented in Figure 4.5. Shear wave velocity for the upper 30 m ($V_{s,30}$) is estimated as 650-700 m/s by Multi-Channel Surface Wave Analysis Method (MASW). The structural damage patterns specific for the district are not available yet and will be the scope of future studies.

Elazığ-Zafran District

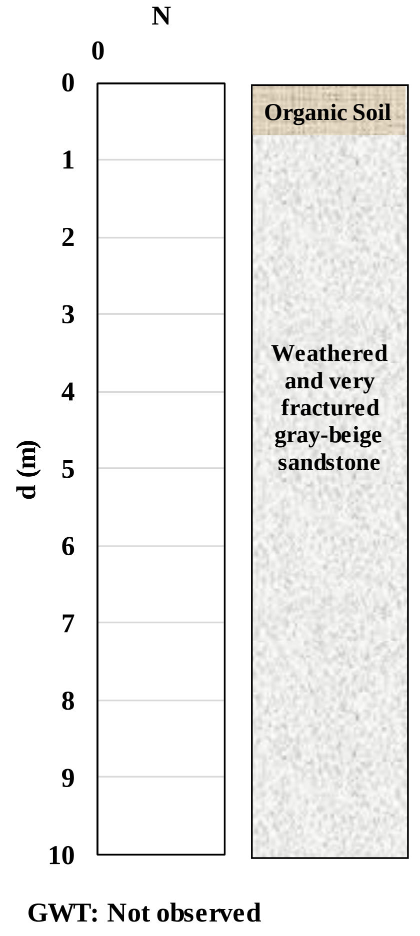

Core Recovery	RQD (%)	Weathering Degree	Crack Frequency
20	14	W2	>50
40	40	W2	>50
40	8	W2	>50
50	50	W2	>50
36	20	W2	>50
33	25	W2	>50
55	47	W2	>50

Figure 4.5 Typical Borelog for Elâzığ-Zafran District

4.3 Ground Deformations in the Very Near Fault Region

The reconnaissance team visited Elâzığ and Malatya regions on the days of 31.01.2020 – 01.02.2020. Hazar Lake is visited on the first day, the route of which is shown in Figure 4.6. The team stopped at 16 locations around Hazar Lake. The detailed observations are discussed in Section 4.2.1.

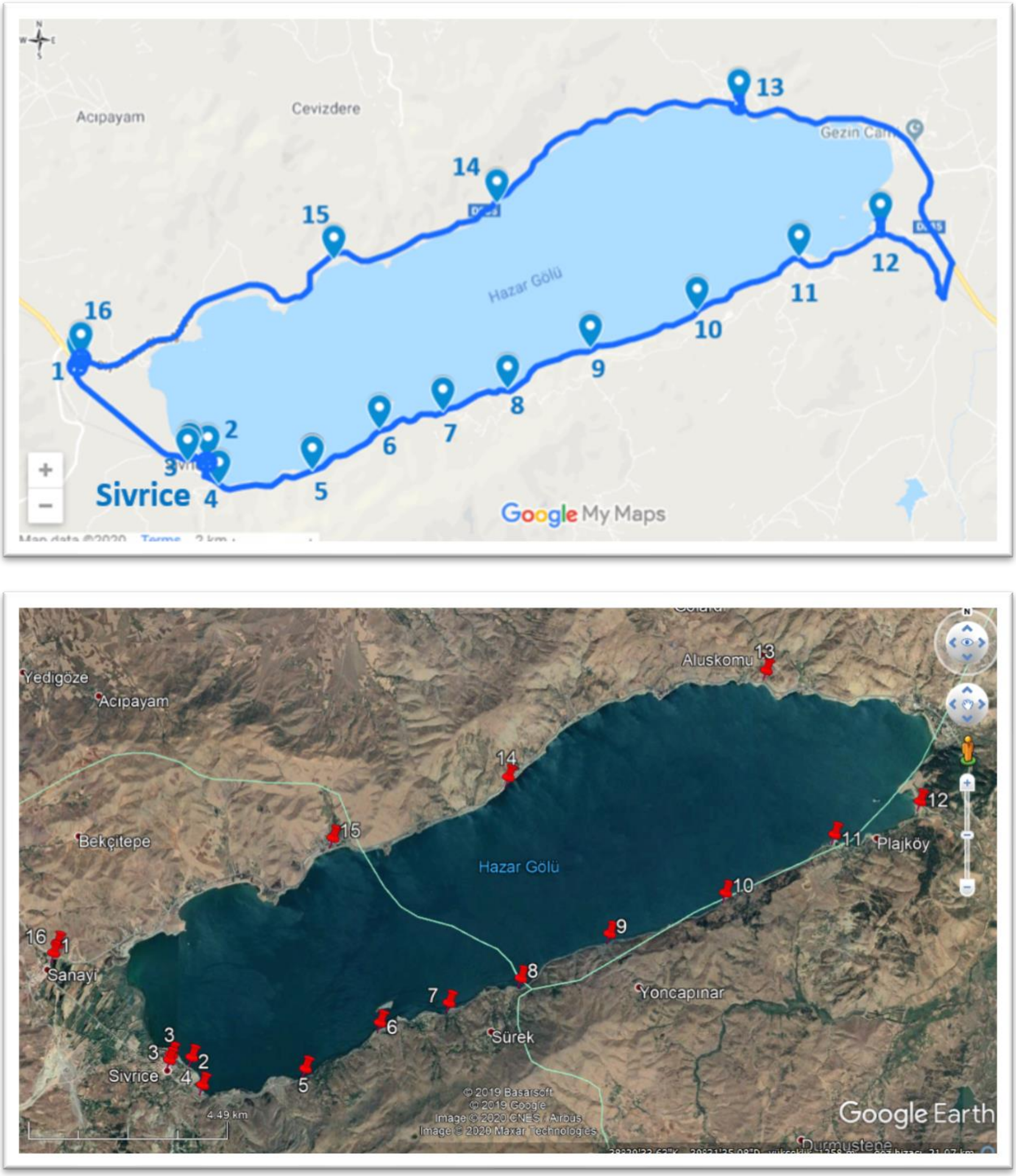

Figure 4.6 Site Visits-Day 1

Kamışlık, Fırat River, Malatya and Elâzığ, Kapıkaya Dam sites are visited in the second day, as shown in Figure 4.7. The team stopped again at 16 locations. The detailed observations from day two are discussed in Section 4.2.2.

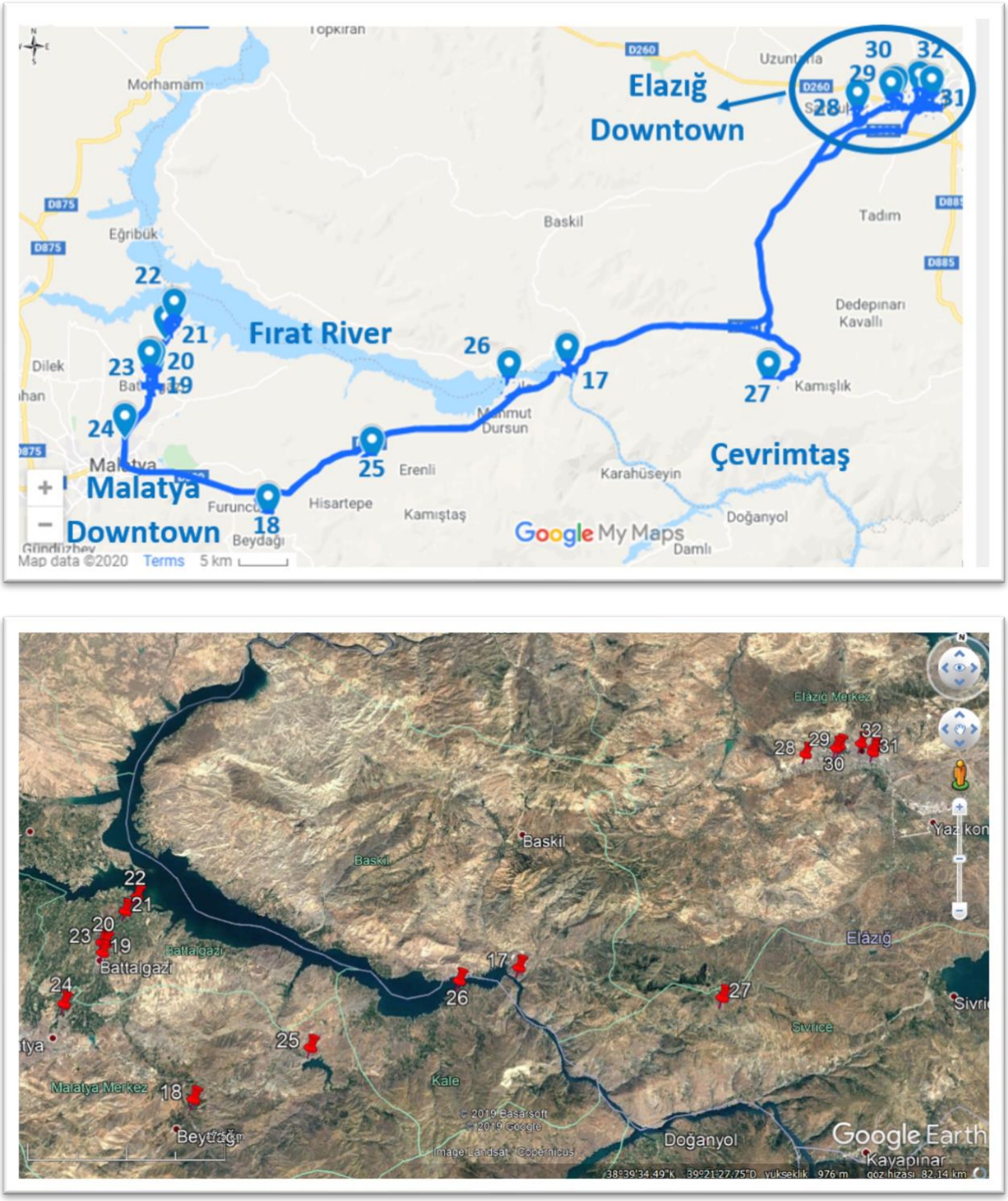

Figure 4.7 Site Visits-Day 2

4.3.1 Day 1: Hazar Lake Coast

1st stop- Sivrice Road

The surficial soils and the alluvial geological setting are concluded to be suitable for liquefaction triggering. However, no signs of liquefaction in the form of sand boils, lateral spread, excessive settlements, etc. were observed at the first stop, as shown in Figure 4.8.

Figure 4.8 A view of the site taken by Sivrice road
(38°28'08.6''N 39°16'40.2''E / 31.01.2020 / 11:47)

A small crack indicating a local bench failure was observed near the Sivrice road embankment, as shown in Figure 4.9. The crack is examined and presumed as a sign of a local small-scale slope instability problem.

Figure 4.9 A small crack observed near the highway embankment (38°28'08.0"N 39°16'38.7"E / 31.01.2020 / 11:50)

On the first stop just down the road embankment, a neighboring site was also visited, as shown in Figure 4.10. The site is composed of surficial clayey soils based on field observations. No damage and surface manifestation of ground deformations were observed.

Figure 4.10 Clayey site and no signs of ground failure
(38°28'09.0"N 39°16'46.8"E / 31.01.2020 / 11:51)

A crack was observed on the sidewalk near to Sivrice road as presented in Figure 4.11. The orientation of the cracking does not support a slope instability problem, which may be interpreted as an old crack existing before the earthquake.

Figure 4.11 Clayey site, no signs of failure
(38°28'10.0"N 39°17'03.6"E / 31.01.2020 / 11:56)

2nd stop- Sivrice Dock

Seismically-induced lateral spreading and volumetric settlements were observed on the natural beach of Hazar Lake shoreline and Sivrice dock. Observed ground failure was mapped and discussed in a detailed manner in Section 4.7. Distribution of volumetric settlement and lateral displacements are mapped as shown in Figures 4.12 to 4.19, respectively. Next to the lake beach, where liquefaction manifestation is observed, a neighboring beach has exhibited no signs of ground failure, as given in Figure 4.20 and 4.21.

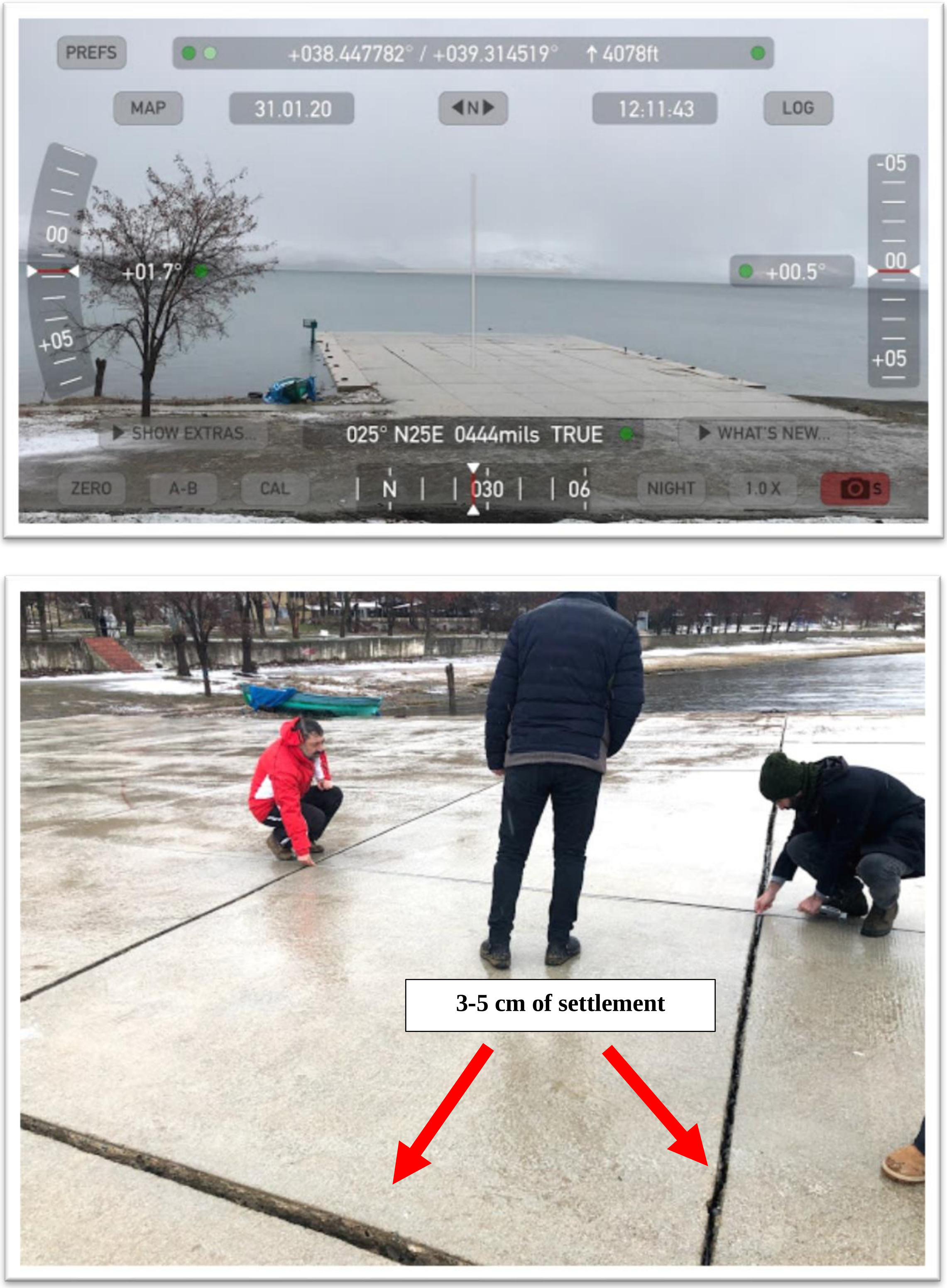

Figure 4.12 Seismically-induced volumetric settlement in the dock of Hazar Lake (38°28'10.0"N 39°17'03.6"E / 31.01.2020 / 12:11 & 38°26'53.2"N 39°18'53.4"E / 31.01.2020 / 12:14)

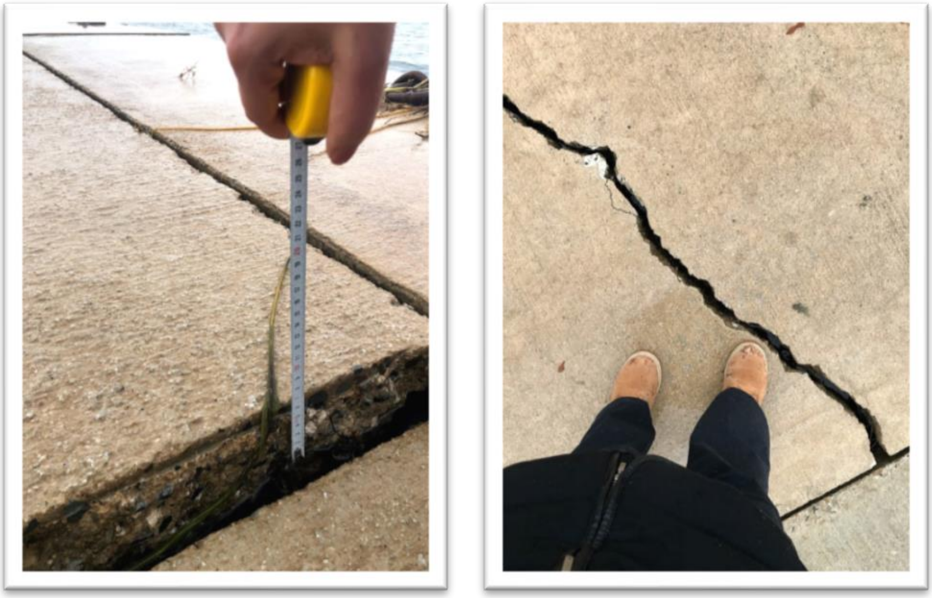

Figure 4.13 Measurements of seismically-induced volumetric settlement in the dock of Hazar Lake

(38°26'53.1"N 39°18'53.6"E / 31.01.2020 / 12:16 & 38°26'53.2"N 39°18'52.9"E / 31.01.2020 / 12:13)

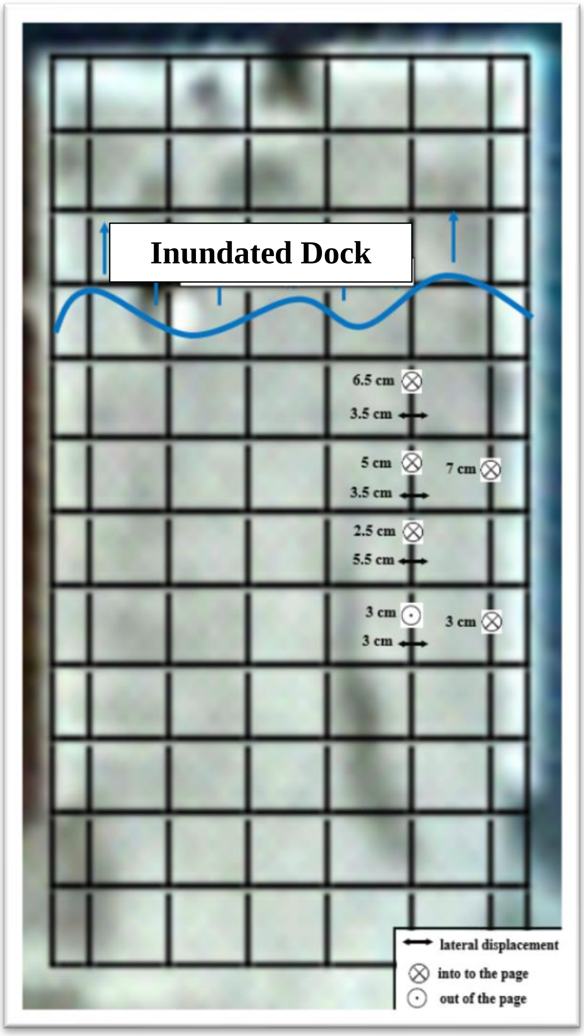

Figure 4.14 Displacements observed on reinforced concrete dock blocks

Figure 4.15 **S**eismically-induced lateral spreading on the beach of Hazar Lake
(38°26'53.7"N 39°18'54.2"E / 31.01.2020 / 12:21 & 38°26'50.7"N 39°18'56.9"E / 31.01.2020 / 12:21)

Figure 4.16 Seismically-induced lateral spreading ground deformations mapped on the beach of Hazar Lake
(38°26'50.7"N 39°18'56.7"E / 31.01.2020 / 12:28)

Figure 4.17 Seismically-induced lateral spreading on the beach of Hazar Lake
(38°26'48.4"N 39°18'57.4"E / 31.01.2020 / 12:31 & 38°26'50.1"N 39°18'57.2"E / 31.01.2020 / 12:54)

Figure 4.18 Another view of seismically-induced lateral spreading cracks
(38°26'50.7"N 39°18'55.4"E / 31.01.2020 / 12:36)

Figure 4.19 Mapping efforts of seismically-induced lateral spreading on the beach of Hazar Lake
(38°26'50.0"N 39°18'57.2"E / 31.01.2020 / 13:14)

Figure 4.20 No ground failure on a neighboring beach of Hazar Lake
(38°26'48.9"N 39°18'59.4"E / 31.01.2020 / 13:08)

Figure 4.21 No ground failure on a neighboring beach of Hazar Lake
(38°26'48.9"N 39°18'59.4"E / 31.01.2020 / 13:08)

3rd stop

In the third stop, the railway tracks were observed to experience no damage, as shown in Figure 4.22.

Figure 4.22 A view of railway tracks without any damage at Sivrice
(38°26'49.5''N 39°18'33.4''E / 31.01.2020 / 13:29)

Toppled chimneys were observed as presented in Figure 4.23 and Figure 4.24. These failures show the intensity of shaking observed at the site, indicating a Mercalli intensity scale of VIII.

Figure 4.23 Toppled chimneys in Sivrice
(38°26'49.6"N 39°18'32.9"E / 31.01.2020 / 13:29)

Figure 4.24 Toppled chimney in Sivrice
(38°26'49.7"N 39°18'33.0"E / 31.01.2020 / 13:30)

4th stop

In the fourth stop, surface geology has changed to volcanic rocks, as shown in Figure 4.25. No ground failure was observed due to earthquake.

Figure 4.25 No signs of ground failure
(38°26'32.0"N 39°19'11.4"E / 31.01.2020 / 13:42 & 38°26'33.2"N 39°19'10.0"E / 31.01.2020 / 13:42 & 38°26'31.9"N 39°19'04.4"E / 31.01.2020 / 13:3)

5th stop

No damage was observed on the railway tunnel. Railway tunnel is open to service and Güney Kurtalan Express Train was serving, as documented in Figures 4.26 and 4.27 along with the coordinates of the pictures taken.

Figure 4.26 A view of the tunnel in Stop 5
(38°26'43.7"N 39°20'40.8"E / 31.01.2020 / 13:54)

Figure 4.27 Güney Kurtalan Express Train passing by
(38°26'56.9"N 39°21'16.7"E / 31.01.2020 / 13:59)

The shoreline by the railway tunnel was also visited. The road embankment has relatively steep slopes (nearly 45˚); however, no ground failure was observed along this shoreline (Figure 4.28).

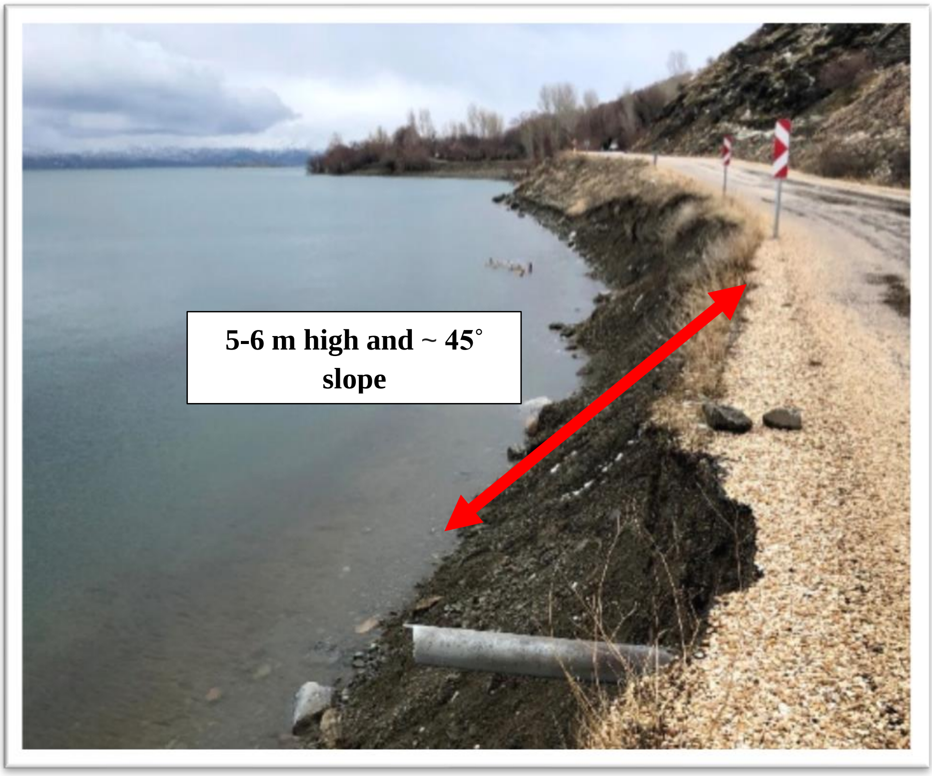

Figure 4.28 No failure on the road embankment
(38°26'43.7"N 39°20'40.7"E / 31.01.2020 / 13:54)

6th stop

The surficial soil layers are composed of low plasticity clays as shown in Figure 4.29. No signs of ground failure were observed.

Figure 4.29 No ground failure at the 6th stop
(38°27'17.1"N 39°21'49.3"E / 31.01.2020 / 14:03

7th stop

No ground failure was observed at steep slopes of the 7th stop, as shown in Figure 4.30.

Figure 4.30 No ground failure was observed at the shores of 7th stop
(38°27'31.0"N 39°22'55.9"E / 31.01.2020 / 14:08)

8th stop

Seismically-induced liquefaction failure was observed in the form of sand boils as shown in Figures from 4.31 to 4.37.

Figure 4.31 Sand boil observed in Stop 8
(38°27'49.7"N 39°24'01.1"E / 31.01.2020 / 14:38)

Figure 4.32 Sand boils observed in Stop 8
(38°27'49.8"N 39°24'03.0"E / 31.01.2020 / 14:14)

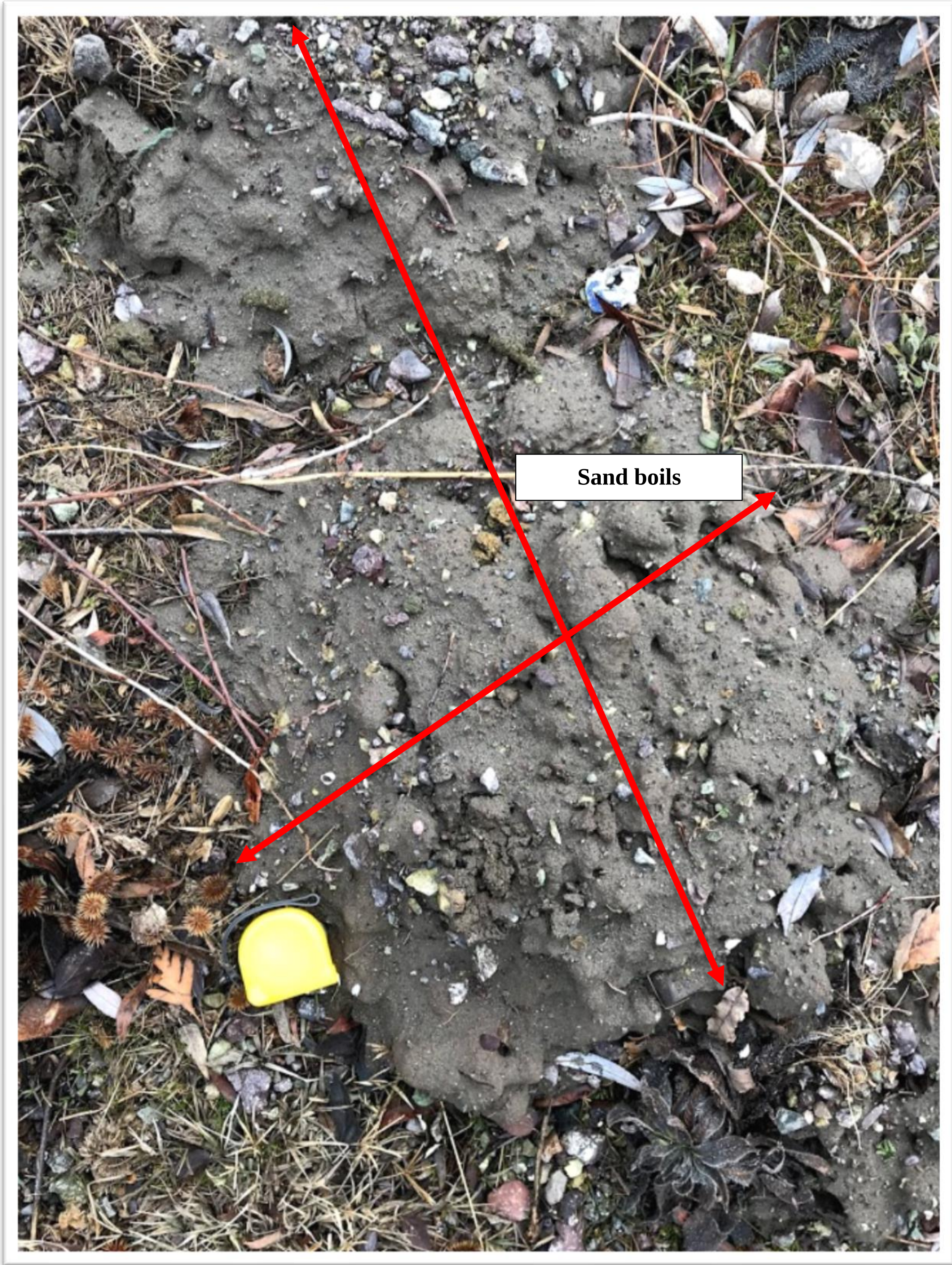

Figure 4.33 Sand boils observed in Stop 8
(38°27'49.9"N 39°24'02.8"E / 31.01.2020 / 14:17)

Figure 4.34 Sandy soil layers observed in Stop 8
(38°27'50.3"N 39°24'02.1"E / 31.01.2020 / 14:21)

Figure 4.35 A line of sand boils observed in Stop 8
(38°27'49.7"N 39°24'03.3"E / 31.01.2020 / 14:16)

Figure 4.36 Sand boil observed in Stop 8
(38°27'49.6"N 39°24'01.7"E / 31.01.2020 / 14:38)

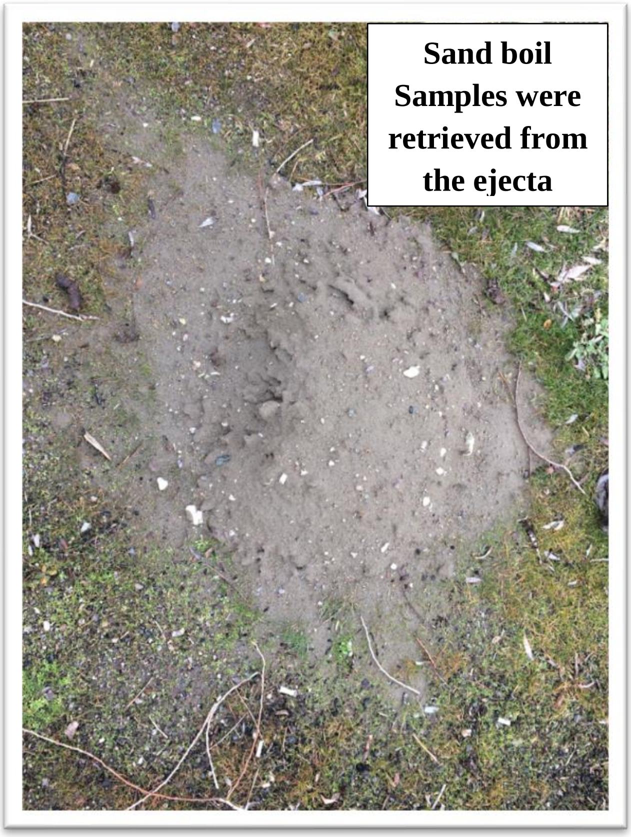

Figure 4.37 Sand boil observed in Stop 8
(38°27'50.1"N 39°24'01.3"E / 31.01.2020 / 14:43)

9th stop

No ground failure was observed at this site, as presented in Figure 4.38.

Figure 4.38 No ground failure was observed at shore of 9th stop
(38°28'22.2"N 39°25'24.9"E / 31.01.2020 / 14:53)

10th stop

A relatively very short (~15 m long) railway tunnel was constructed at the toe of a highly weathered rock steep slope. Tunnel has been possibly designed to eliminate toe excavations, which may trigger slope instability problems. No damage was observed, as also presented in Figures 4.39 to 4.41. Additionally, no slope failure was observed near Hazar Lake, as presented in Figure 4.42.

Figure 4.39 A railway tunnel and rails exhibiting no damage
(38°28'52.8"N 39°27'18.2"E / 31.01.2020 / 15:08)

Figure 4.40 A view of tunnel body at Stop 10
(38°28'53.2"N 39°27'18.4"E / 31.01.2020 / 15:09)

Figure 4.41 Interbeddings observed in volcanic rocks
(38°28'53.2''N 39°27'17.9''E / 31.01.2020 / 15:08)

Figure 4.42 No ground failure was observed at shore of 10th stop
(38°28'52.6''N 39°27'16.9''E / 31.01.2020 / 15:04)

11^{th} stop

At 11^{th} stop, no ground failure was observed as shown in Figure 4.43.

Figure 4.43 No ground failure was observed at shore of 11^{th} stop
(38°29'37.1"N 39°29'02.3"E / 31.01.2020 / 15:18)

12^{th} stop

Sand boils were observed at 12^{th} stop. These surface manifestations are shown in Figure 4.44.

Figure 4.44 Sand boils observed
(38°29'58.5"N 39°30'24.6"E / 31.01.2020 / 15:29 & 38°29'57.6"N 39°30'23.9"E / 31.01.2020 / 15:30 & 38°29'57.7"N 39°30'24.0"E / 31.01.2020 / 15:30)

13th stop

Rock falls were mapped at 13th stop as shown in Figures 4.45 to 4.49. Approximate dimensions (length, width, height) of the rocks are measured in the field. A simulation of the rock fall mechanism suggested a peak ground velocity of 4-6 m/s at the region as will be discussed later in the report. Fallen rock blocks horizontal distances from the toe of the first bench were measured as 3-5 m. The details of rockfall assessments will be presented later in the report.

Figure 4.45 Rockfall at 13th stop (general view)
(38°31'40.3"N 39°28'02.9"E / 31.01.2020 / 16:20)

Figure 4.46 Rockfall at 13th stop (upper bench)
(38°31'41.5''N 39°27'60.0''E / 31.01.2020 / 16:10)

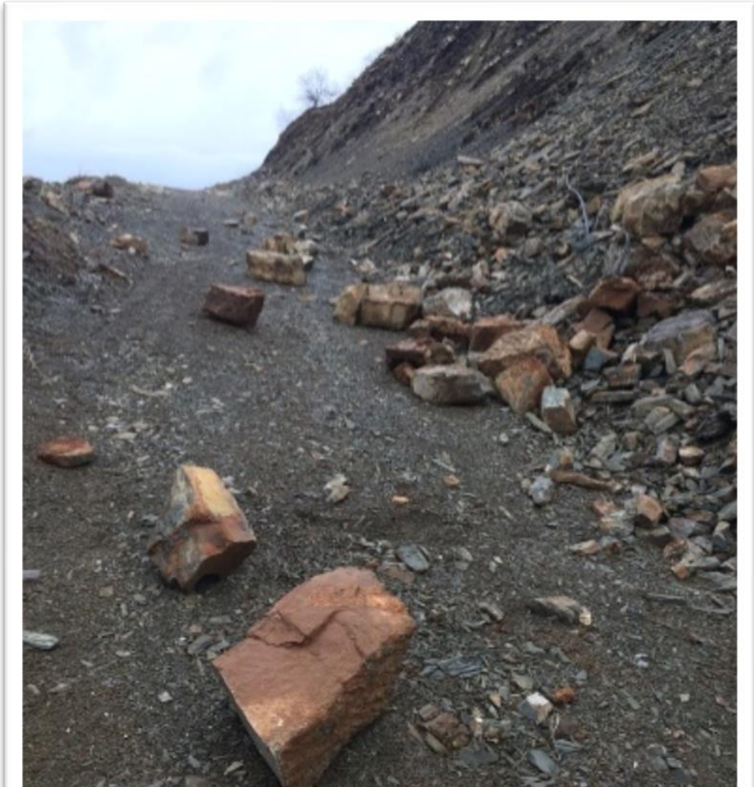

Figure 4.47 Rockfalls at 13th stop
(38°31'41.0''N 39°27'59.6''E / 31.01.2020 / 16:13)

Figure 4.48 Measurement of rockfalls' dimensions at 13th stop
(38°31'41.3"N 39°27'59.5"E / 31.01.2020 / 16:15 & 38°31'41.5"N 39°27'59.0"E / 31.01.2020 / 16:16)

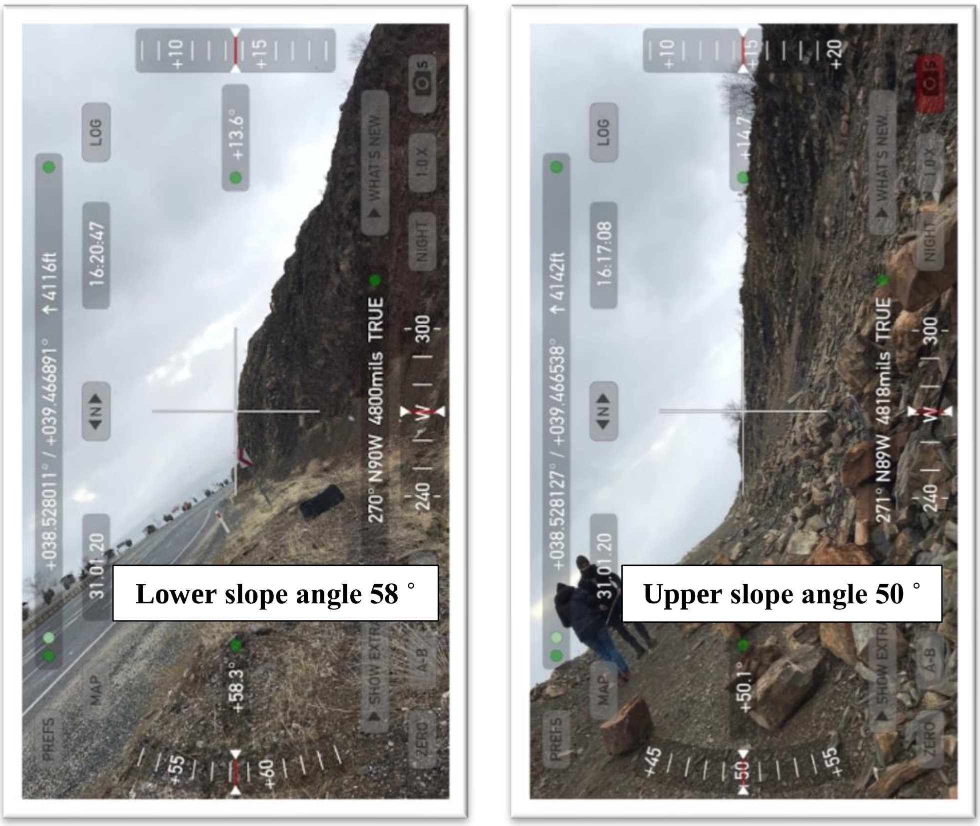

Figure 4.49 Rockfalls at 13th stop (Slope angle determination)
(38°31'40.8"N 39°28'00.8"E / 31.01.2020 / 16:20 & 38°31'41.3"N 39°27'59.5"E / 31.01.2020 / 16:17)

14th stop

A 65˚ slope was documented to be stable as shown in Figures 4.50 and 4.51.

Figure 4.50 Side view of the slope
(38°30'11.7"N 39°23'33.4"E / 31.01.2020 / 16:34 & 38°30'11.8"N 39°23'33.3"E / 31.01.2020 / 16:34)

Figure 4.51 Side view of the slope
(38°30'11.6''N 39°23'33.7''E / 31.01.2020 / 16:34)

Fallen rock blocks were also observed and mapped at the 14th stop. Approximate diameter of the rocks varies from 80 cm to 120 cm, and the slope angle was measured as 39˚. Figure 4.52 shows the slope and fallen rocks.

Figure 4.52 Rockfalls at 14th stop
(38°30'11.4"N 39°23'34.9"E / 31.01.2020 / 16:37 & 38°30'11.3"N 39°23'34.7"E / 31.01.2020 / 16:37)

15th stop

Seismically-induced liquefaction failure was observed in the form of sand boils at the 15th stop. Examples of sand boils in different forms are presented in Figures 4.53 to 4.55. Note that the plane tree leaves were covered by the sand boils in Figure 4.53.

Figure 4.53 Seismic soil liquefaction-induced sand boils at Stop 15
(38°29'32.3"N 39°21'03.8"E / 31.01.2020 / 16:57 & 38°29'34.5"N 39°21'03.6"E / 31.01.2020 / 17:11)

Figure 4.54 Seismic soil liquefaction-induced sand boils
(38°29'32.1''N 39°21'02.0''E / 31.01.2020 / 16:58)

Figure 4.55 Seismic soil liquefaction-induced sand boils
(38°29'34.5"N 39°21'03.7"E / 31.01.2020 / 17:12)

16th stop

At the 16th stop, a complete tour around the lake was completed. We felt lucky to complete our field studies before the start of heavy snow, which covered the surface manifestations immediately.

4.3.2 Day 2: Kamışlık, Fırat River, Malatya and Elâzığ, Kapıkaya Dam Sites

In the second day, our plan was to start the reconnaissance studies at Doğanyol, where a port failure was observed. Unfortunately, due to heavy snow, the highway to Doğanyol was closed. However, the port failure was documented based on a video shared by Ihlas Press Agency (IHA). Figure 4.56 shows the port failure, which was adapted from the IHA video shared in Youtube.

Figure 4.56 Doğanyol Port Failure adapted from IHA report
(38°33'34.6"N 39°04'10.6"E)

17th stop

2-3 m diameter rocks were fallen freshly on the shoulders of the highway, as shown in Figure 4.57.

Figure 4.57 Fallen rocks on the highway
(38°26'19.8"N 38°49'38.8"E / 01.02.2020 / 7:23)

New Kömürhan Bridge under construction on Fırat River was visited, which experienced no damage.

18th stop

As stated earlier, in the second day's morning the plan was to go to the Doğanyol village; however, the road accessing to Doğanyol was closed at the hills due to heavy snow storm, as shown in Figure 4.58. The Gendarme prohibited cars traveling beyond this point.

Figure 4.58 Road to Doğanyol
(38°18'39.9"N 38°29'41.7"E / 01.02.2020 / 7:52)

19th stop- Battalgazi Village / Malatya

There are no foundation displacements observed at a residential building in Battalgazi village, as shown in Figures 4.59.

Figure 4.59 A foundation at a residential building in Battalgazi Village

20th stop

Railway tracks were observed to be not damaged at the 20th stop. The railway was under service as presented in Figure 4.67. In the same figure a small bridge is shown again with no signs of damage.

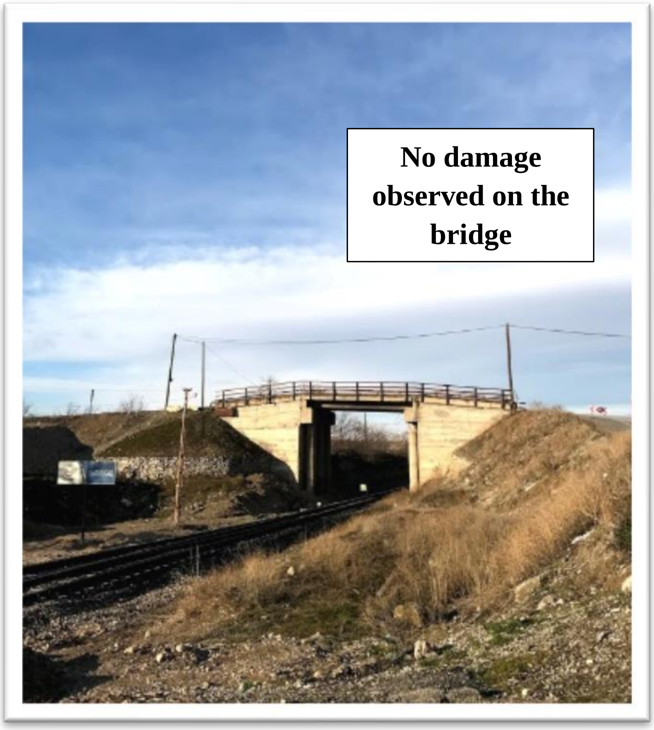

Figure 4.60 Railway and bridge at 20th stop
(38°26'00.1"N 38°21'59.1"E / 01.02.2020 / 8:49 & 38°26'00.2"N 38°22'01.3"E / 01.02.2020 / 8:50)

21st stop- Battalgazi Village Bahçelievler District / Malatya

A number of structural damages were observed, mostly concentrating on masonry buildings in Bahçelievler district of Battalgazi village, as shown in Figure 4.61 and 4.62.

Figure 4.61 Residential buildings in the Bahçelievler district of Battalgazi village
(38°26'51.2"N 38°22'19.2"E / 01.02.2020 / 8:52 & 38°26'51.1"N 38°22'19.2"E / 01.02.2020 / 8:53)

Figure 4.62 Cracks on the wall of a residential building in the Bahçelievler district of Battalgazi village
(38°27'48.5"N 38°22'50.6"E / 01.02.2020 / 8:56 & 38°27'49.0"N 38°22'51.7"E / 01.02.2020 / 8:56)

22nd stop- Battalgazi Village, Toygar District/ Malatya

Although it is composed of alluvial deposits with potential for ground failure, no signs of it were observed. Surficial soils, observed to be of high plasticity clays, and frozen ground were listed as two factors, which might have impeded possible ground failure, as shown in Figures 4.63 and 4.64.

Figure 4.63 Views of frozen soil in Toygar district of Battalgazi village
(38°28'38.6"N 38°23'27.1"E / 01.02.2020 / 9:03)

Figure 4.64 Views of frozen clayey soils in Toygar district of Battalgazi village (38°28'38.9"N 38°23'27.3"E / 01.02.2020 / 9:03 & 38°28'39.8"N 38°23'29.3"E / 01.02.2020 / 9:05)

23rd stop

A water canal and the highway bridge were documented with no signs of damage, as shown in Figure 4.65 and Figure 4.66. Note that the observed cracks were dated older and are not associated with the recent earthquake event.

Figure 4.65 Water trench in Dolamantepe district of Battalgazi village
(38°26'00.4"N 38°21'44.1"E / 01.02.2020 / 9:25)

Figure 4.66 Dolamantepe district of Battalgazi village
(38°25'59.9"N 38°21'41.5"E / 01.02.2020 / 9:26)

24th stop

There is no soil induced damage observed in Battalgazi Village Hanımçiftliği district.

25th stop- Kapıkaya Dam / Malatya

The dam was built on Memikhan River for irrigation purposes. It is an 89.5 m high clay core rockfill dam. The crest and normal water elevations were 868 m and 864.9, respectively. During our visit the water level was measured as 854.70 m. The right and left abutments along with the dam body itself were documented to be not affected from the shaking. Also, no damage to water in-take and spillways were observed. Pictures taken at the dam site can be seen in Figures 4.67 to 4.74.

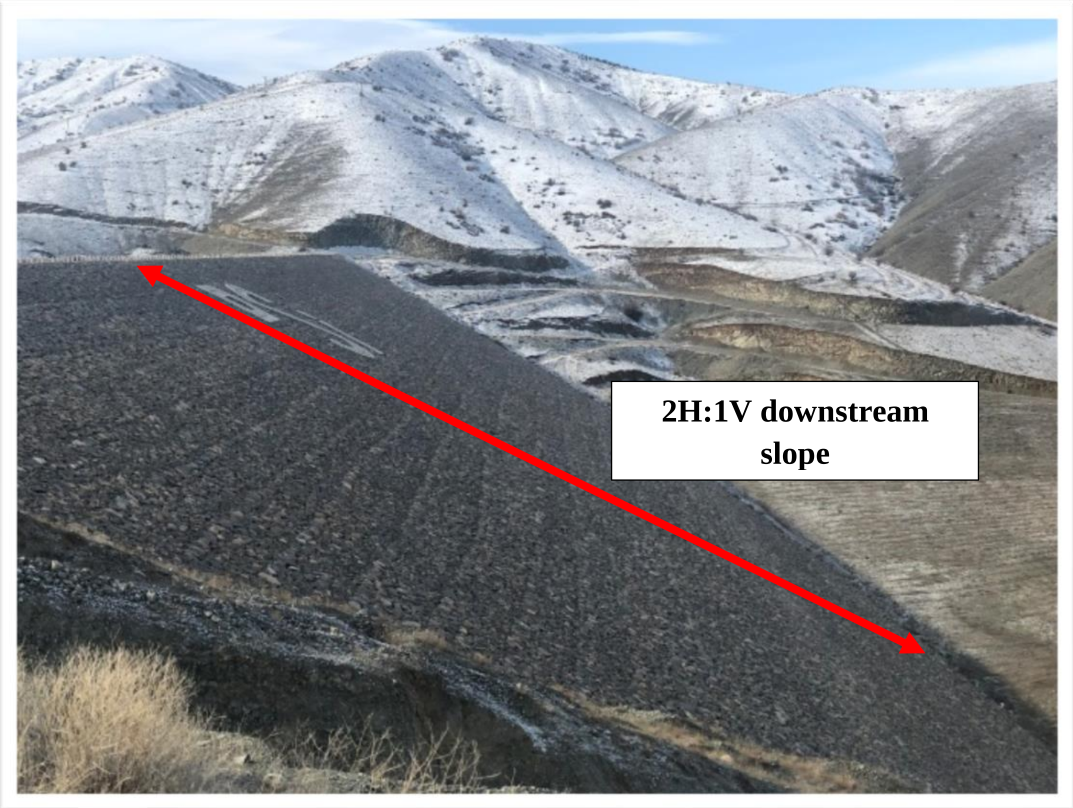

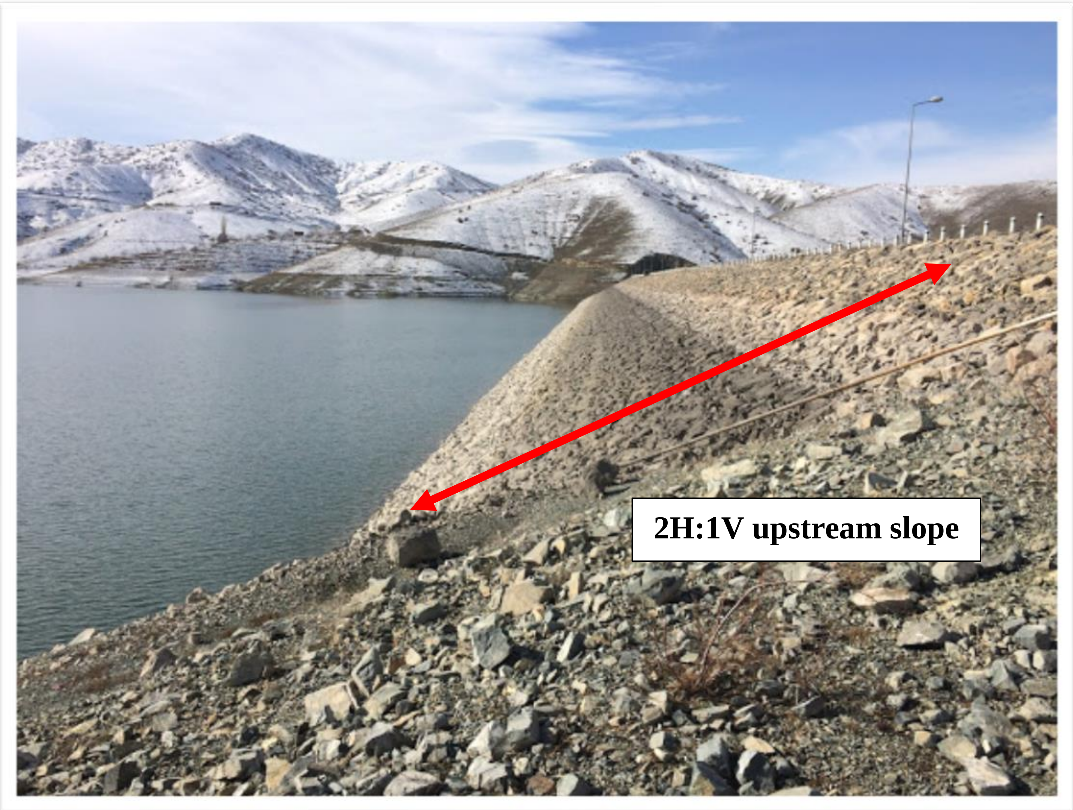

Figure 4.67 Side views of Kapıkaya Dam
(38°21'19.1"N 38°36'33.9"E / 01.02.2020 / 10:21 & 38°21'16.3"N 38°36'35.0"E / 01.02.2020 / 10:38)

Figure 4.68 Side view of Kapıkaya Dam downstream face
(38°21'16.3"N 38°36'33.2"E / 01.02.2020 / 10:40 & 38°21'13.1"N 38°36'26.7"E / 01.02.2020 / 10:46)

Figure 4.69 Crest view of Kapıkaya Dam
(38°21'15.9"N 38°36'32.8"E / 01.02.2020 / 10:40 & 38°21'12.6"N 38°36'26.9"E / 01.02.2020 / 10:46
& 38°21'16.9"N 38°36'36.0"E / 01.02.2020 / 11:13

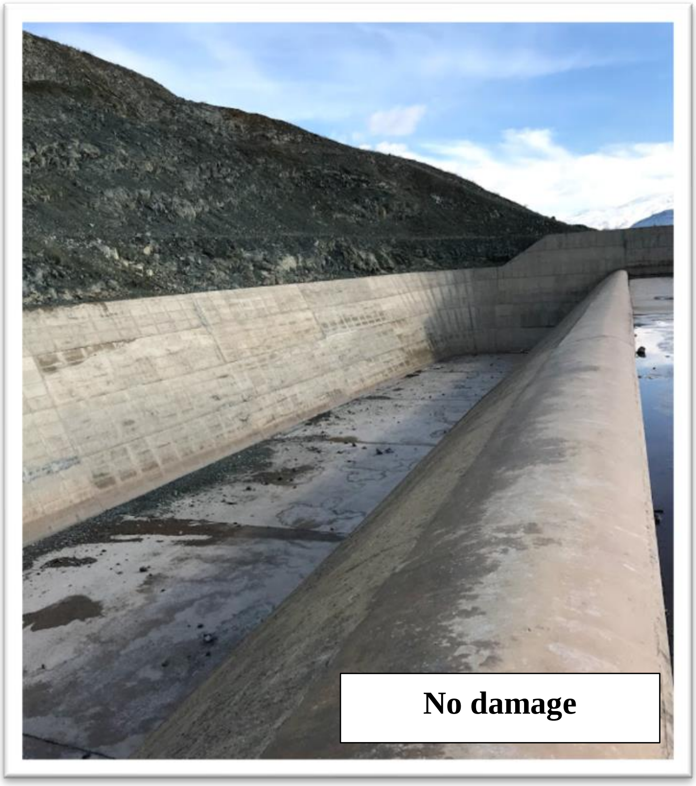

Figure 4.70 Water in-take structure of Kapıkaya Dam
(38°21'17.2"N 38°36'36.7"E / 01.02.2020 / 11:14)

Figure 4.71 Spillway of Kapıkaya Dam
(38°21'19.1"N 38°36'33.9"E / 01.02.2020 / 10:22 & 38°21'19.2"N 38°36'34.1"E / 01.02.2020 / 10:22)

Figure 4.72 Abutment slopes of Kapıkaya Dam
(38°21'07.1"N 38°36'22.0"E / 01.02.2020 / 10:51)

Figure 4.73 Right abutment natural slopes
(38°21'18.7"N 38°36'36.0"E / 01.02.2020 / 10:25)

Figure 4.74 Settlement Plate, piezometer, data acquisition house and inclinometer borehole located at Kapıkaya Dam
(N/A / 01.02.2020 / 10:50 & 38°21'11.7"N 38°36'23.5"E / 01.02.2020 / 10:48
38°21'11.1"N 38°36'23.7"E / 01.02.2020 / 10:48 & 38°21'10.2"N 38°36'23.0"E / 01.02.2020 / 11:06)

26th stop- Kale Village / Malatya

Seismically-induced liquefaction failure was observed in the Kale shores (Figure 4.75 and 4.76) in the form of sand boiling at 15th stop. A site view is shown in Figure 4.77. Pictures documenting sand boils are presented in Figures 4.78 to 4.82.

Figure 4.75 View of Kale shore
(38°25'25.1"N 38°45'46.1"E / 01.02.2020 / 12:12)

Figure 4.76 Another view of Kale shore
(38°25'22.2"N 38°45'40.9"E / 01.02.2020 / 12:17)

Figure 4.77 Kale shore
(38°25'15.9"N 38°45'28.8"E / 01.02.2020 / 12:39)

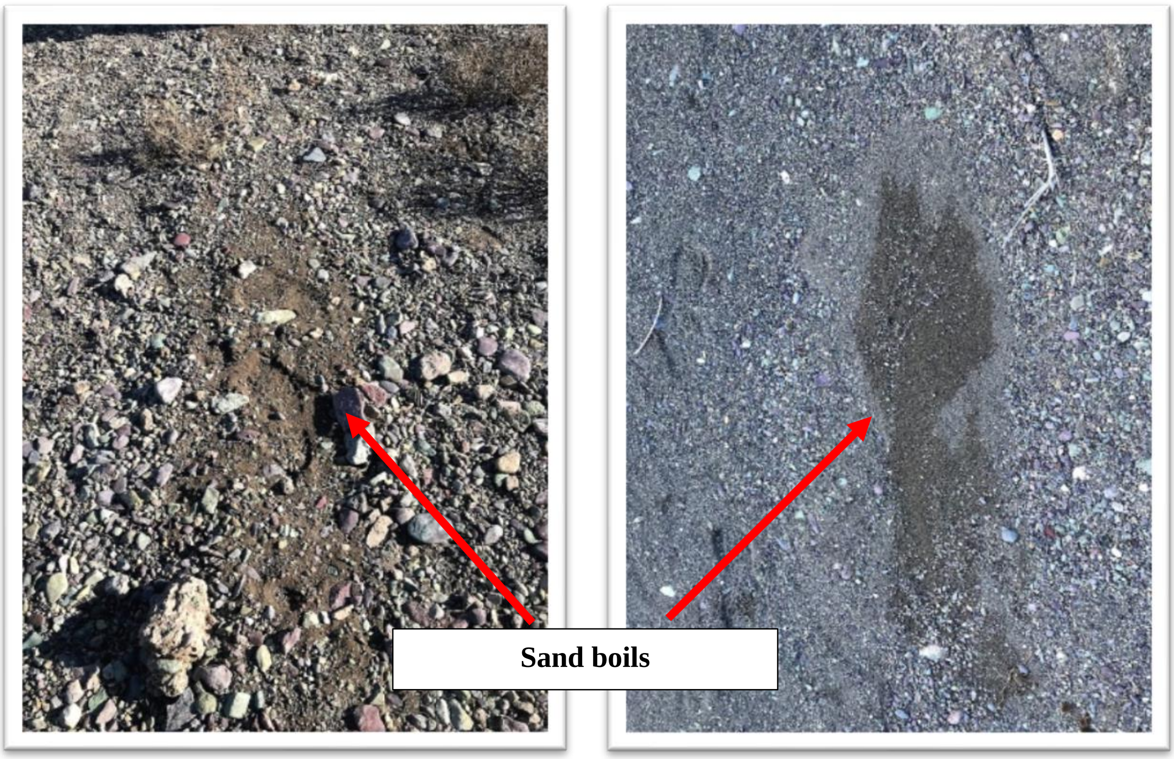

Figure 4.78 Seismic soil liquefaction-induced sand boils at Kale shore
(38°25'19.9"N 38°45'33.2"E / 01.02.2020 / 12:25 & 38°25'14.6"N 38°45'24.7"E / 01.02.2020 / 12:45)

Figure 4.79 Seismic soil liquefaction-induced sand boils at Kale shore
(38°25'15.2"N 38°45'24.1"E / 01.02.2020 / 12:45)

Figure 4.80 Seismic soil liquefaction-induced sand boils at Kale shore
(38°25'22.8"N 38°45'38.4"E / 01.02.2020 / 12:21)

Figure 4.81 Seismic soil liquefaction-induced sand boils at Kale shore
(38°25'19.9"N 38°45'32.1"E / 01.02.2020 / 12:27)

Figure 4.82 Seismic soil liquefaction-induced sand boils at Kale shore
(38°25'15.2"N 38°45'32.2"E / 01.02.2020 / 12:32 & 38°25'15.2"N 38°45'23.9"E / 01.02.2020 / 12:45)

27th stop

Our intent was to access to Çevrimtaş, the epicentral district. However, the road was closed to traffic due to heavy snow. (Figure 4.83). It was decided to spend the rest of the reconnaissance time in Elâzığ downtown.

Figure 4.83 Snow-covered road on our way to Çevrimtaş
(38°25'26.3"N 39°03'01.3"E / 01.02.2020 / 13:52)

28th stop- Abdullahpaşa District / Elâzığ

A number of structurally damaged residential buildings were documented in Abdullahpaşa district of Elâzığ city center, as shown in Figures 4.84 to 4.85. No signs of foundation failures were observed except a few rare cases of volumetric settlements of foundation backfill soils.

Figure 4.84 Tents for the people suffering from the earthquake
(38°39'30.0"N 39°08'59.5"E / 01.02.2020 / 14:28)

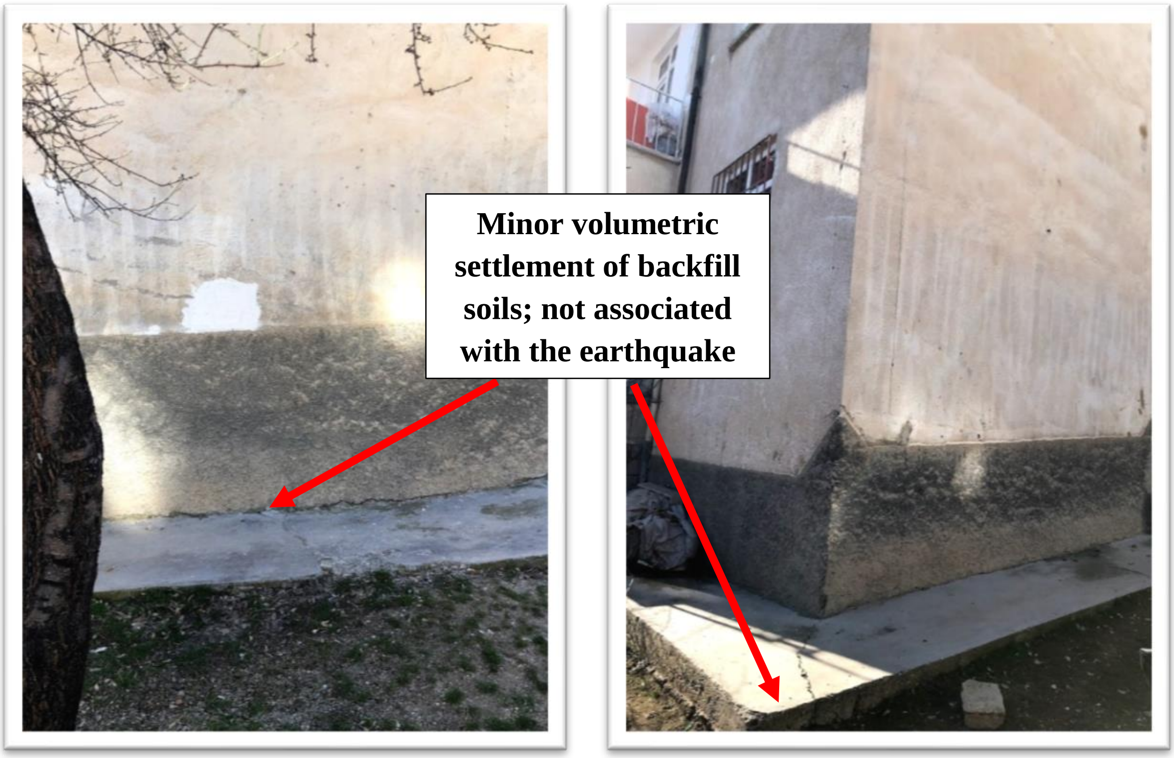

Figure 4.85 Tents for the people suffering from the earthquake
(38°39'29.8"N 39°08'58.4"E / 01.02.2020 / 14:29 & 38°39'28.9"N 39°09'01.9"E / 01.02.2020 / 14:30)

29th stop

Elâzığ ground motion station located at the Ministry of Environment and Urban Planning was visited (Figure 4.86).

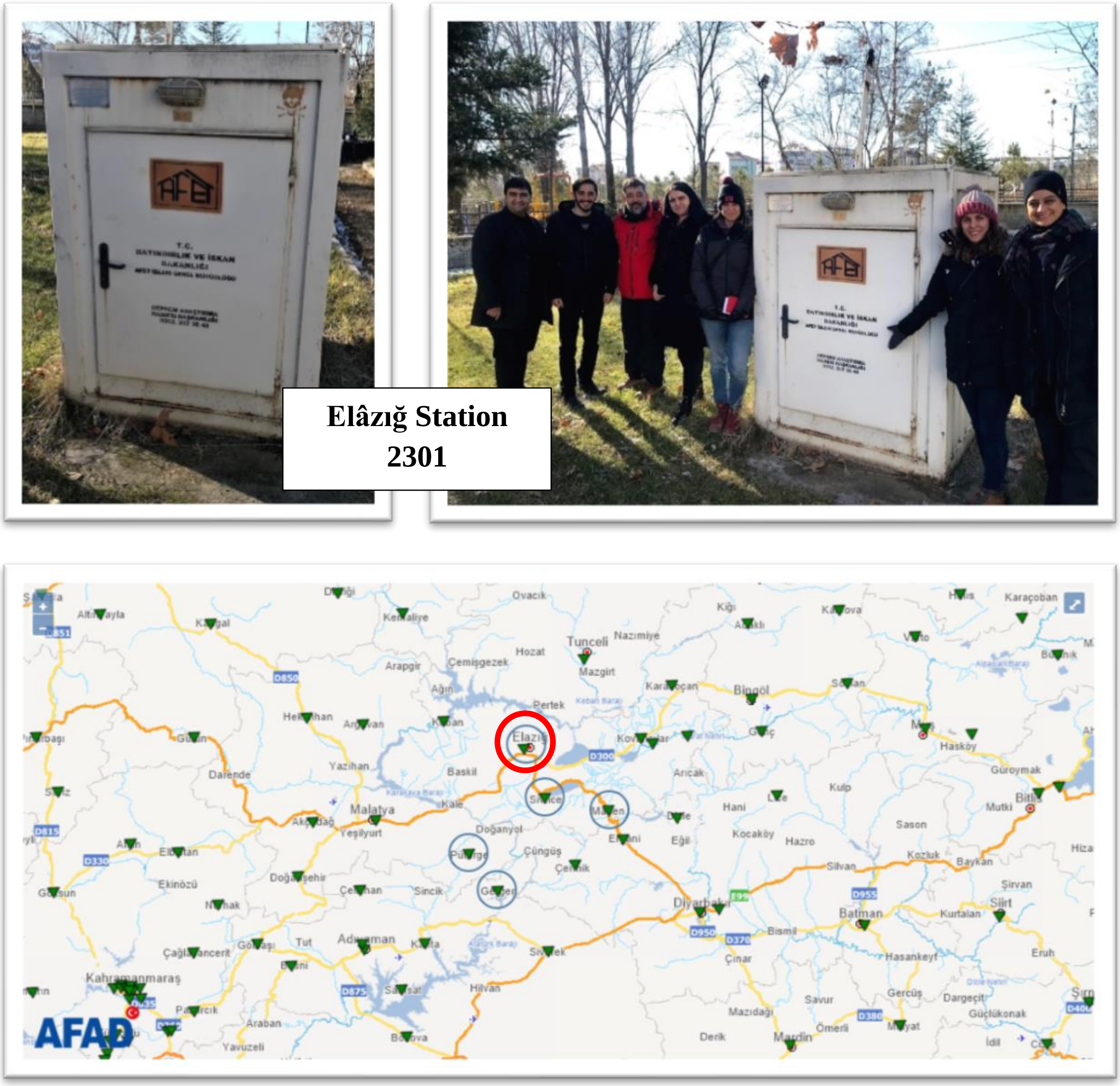

Figure 4.86 Elâzığ ground motion station
(38°40'13.2"N 39°11'31.3"E / 01.02.2020 / 15:08 & 38°40'13.5"N 39°11'31.6"E / 01.02.2020 / 15:09)

30th stop- Sürsürü District / Elâzığ

The most of the structural damage was concentrated in Elâzığ-Sürsürü district. Several structurally damaged residential buildings were documented, as shown in Figures 4.87 to 4.90. The level of damage varies in a large scale, from no damage to heavy damage. Cracks at the pavements, walls and foundations, due to cyclic and residual lateral and volumetric deformations were observed.

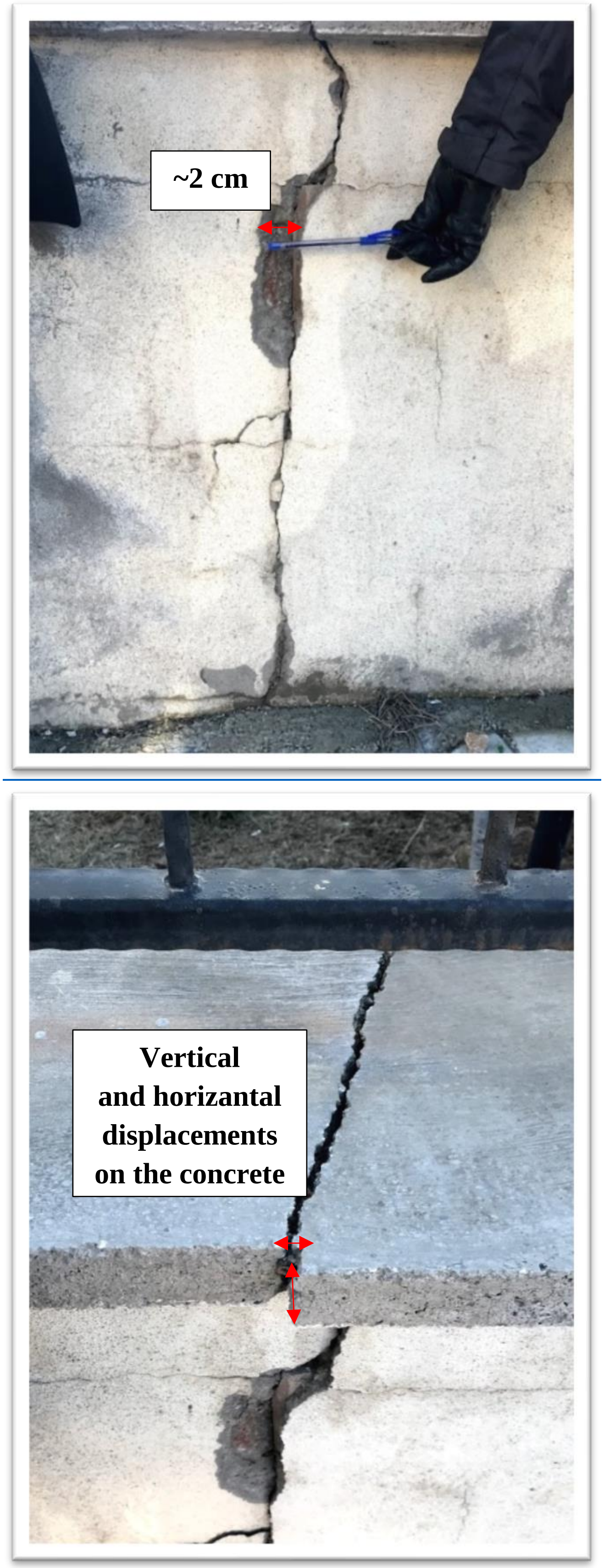

Figure 4.87 A crack on a concrete fence in Sürsürü district of Elâzığ city center
(38°40'05.5"N 39°11'12.4"E / 01.02.2020 / 15:28 & 38°40'05.5"N 39°11'12.4"E / 01.02.2020 / 15:28)

Figure 4.88 Settlement mapped at the entrance of some buildings
(38°40'04.7"N 39°11'12.4"E / 01.02.2020 / 15:31 & 38°40'05.9"N 39°11'08.2"E / 01.02.2020 / 15:41
38°40'05.9"N 39°11'08.1"E / 01.02.2020 / 15:41 & 38°40'04.7"N 39°11'09.7"E / 01.02.2020 / 15:40)

Figure 4.89 Settlements observed
(38°40'05.7"N 39°11'09.6"E / 01.02.2020 / 15:57 & 38°40'05.1"N 39°11'10.0"E / 01.02.2020 / 15:57)

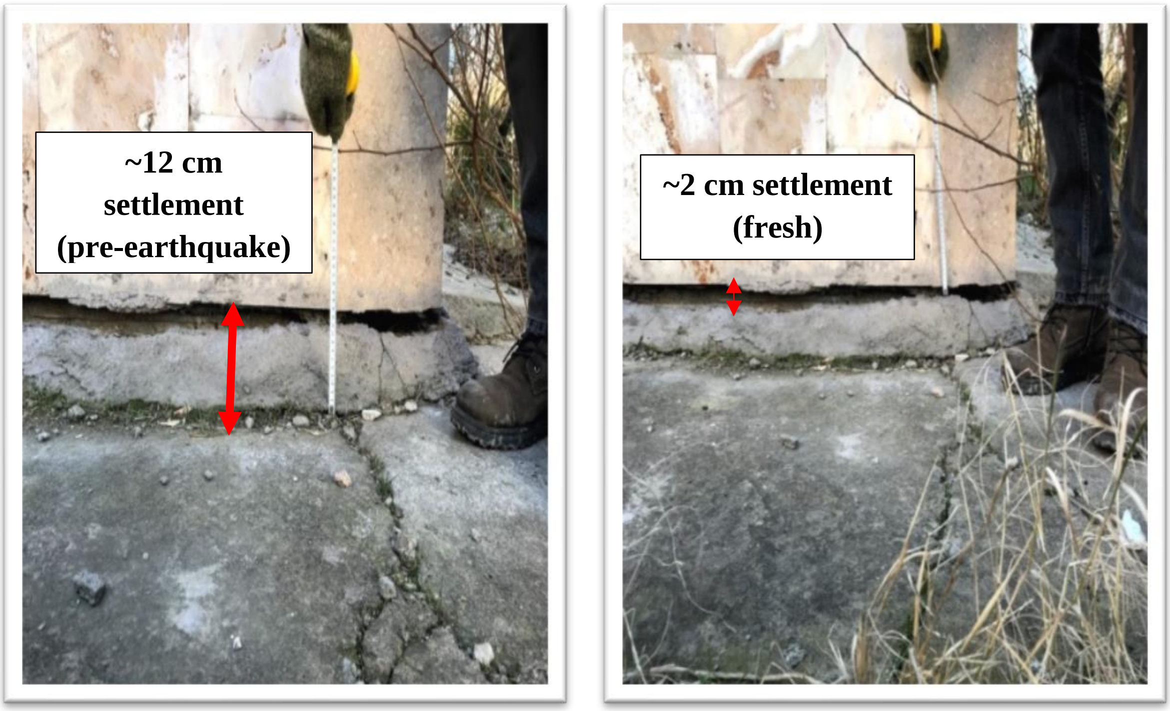

Figure 4.90 Settlement observed
(38°40'07.0"N 39°11'04.8"E / 01.02.2020 / 15:47)

During the site visit, a site investigation study was witnessed. A soil sample was taken from the borehole for laboratory testing. An automatic SPT trip hammer was used as shown Figure 4.91. The available borelog up to the depth of 12 m was retrieved.

Figure 4.91 Drilling efforts
(38°40'03.9"N 39°11'14.8"E / 01.02.2020 / 15:18 & 38°40'03.1"N 39°11'16.1"E / 01.02.2020 / 15:18)

31st stop

There is no soil induced damage observed in this stop.

32nd stop- Mustafapaşa District / Elâzığ

There is no soil induced damage observed in this stop.

4.4 Rockfalls

Field reconnaissance team observed rockfalls during their visit to the coast of Hazar Lake as shown in Figure 4.92 and 4.93. In this section, a more detailed discussion of these rockfalls will be presented.

At the first rockfall site, the surface geology reveals phllyites with schistocity texture. The cross section is 15 m high with a slope of 50°. The dimensions of the fallen rocks and the distance from the edge of the benches are mapped in the field. No fallen rocks were observed on the lower, second bench of the highway cut. Slope angle, length and height of different sections of the upper and lower benches, and possible height that rock falls were initiated were also mapped in the field. RocFall 2019 software program is used to guestimate the initial velocity of the rock.

Figure 4.92 Rockfalls observed at the shores of Hazar Lake at 13th stop
(38°31'40.0"N 39°28'01.5"E /31.01. 2020 / 16:08)

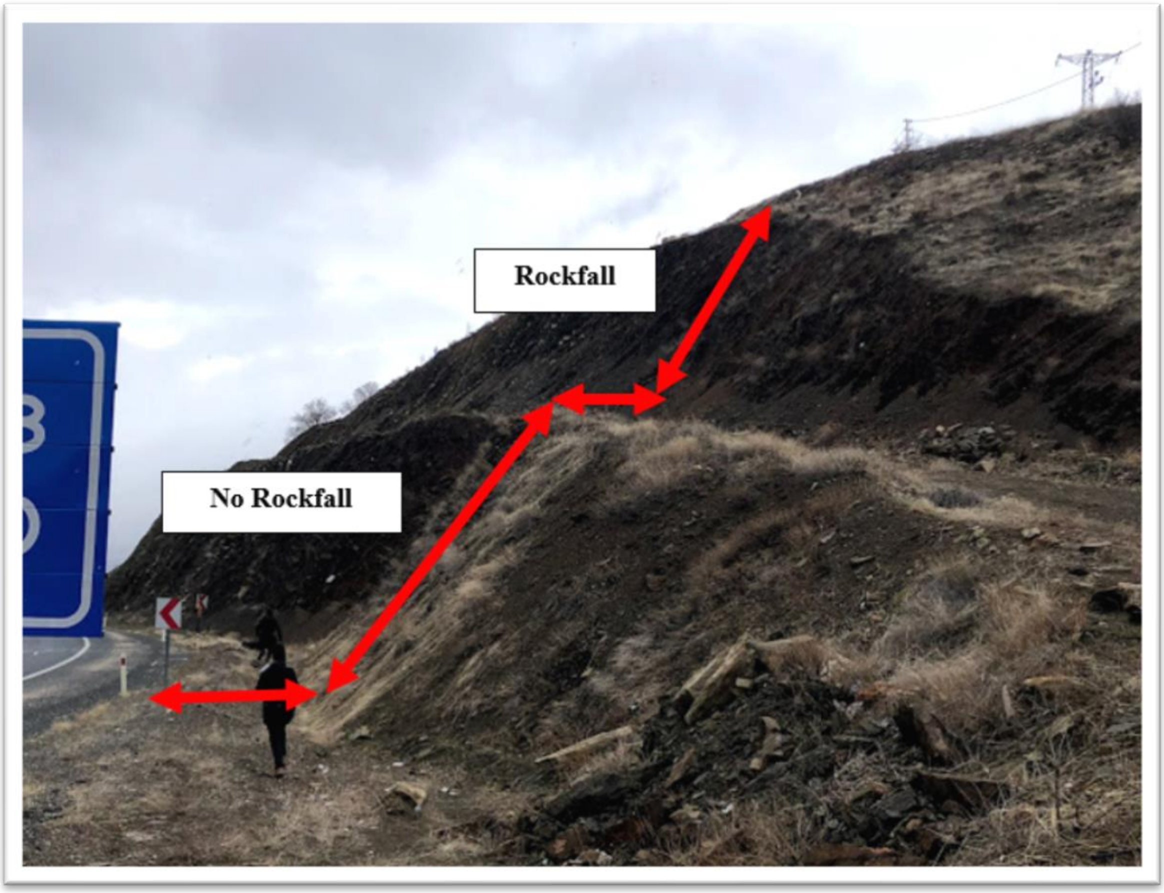

Figure 4.93 Cross section of the rockfall at 13th stop
(38°31'40.3"N 39°28'02.9"E / 31.01.2020 / 16:20)

The dimensions of the some fallen rock blocks and the distance of these rocks to the toe of the upper bench are recorded in the field as also summarized in Table 4-1.

Table 4.1 Fallen rock blocks measurements recorded at 13th stop

Length (cm)	**Height (cm)**	**Width (cm)**	**Distance of the rock blocks to the toe of the slope (m)**
60	30	35	3.9
32	15	30	5
55	30	28	3.2

As seen in Figure 4.94, back analysis is performed to guess the initial velocity of the rock blocks to reach their final positions observed in the field. RocFall 2019 by RocScience is used for the purpose. Based on these very preliminary assessments, velocity range to trigger the fall and match with observed travel distances is calculated as 4 to 6 m/s.

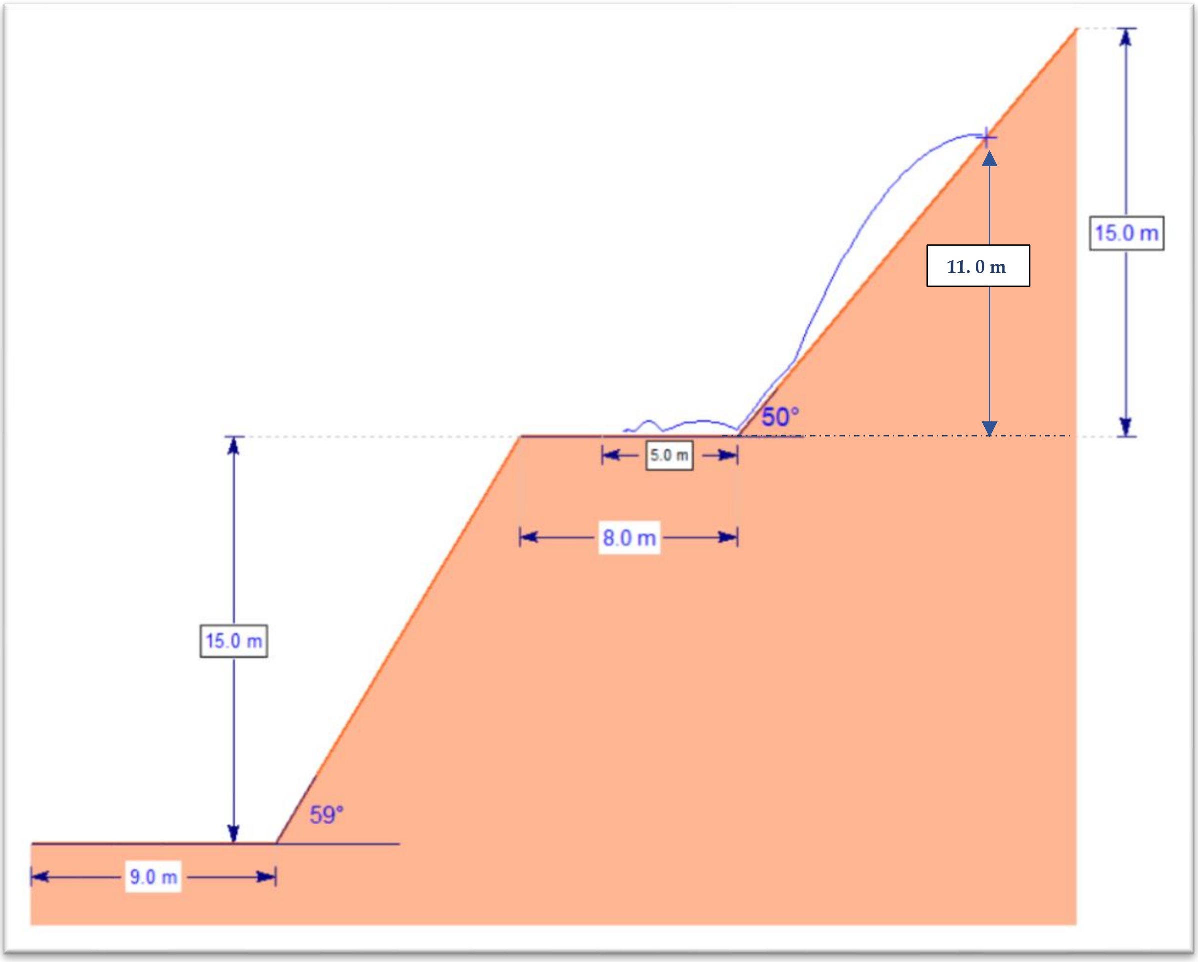

Figure 4.94 Back analysis of rockfall with RocFall 2019

4.5 Earth Structures

4.5.1 Hydraulic Dams

In the vicinity of Elâzığ-Malatya region, there exist 6 dams: Dedeyolu, Karakaya, Cip, Kapıkaya (Turgut Özal), Keban and Boztepe (Recai Kutan) Dams. It was reported by personal communication that a group of engineers from General Directorate of State Hydraulics Works (DSI) have performed reconnaissance studies immediate upon Sivrice Earthquake. Some characteristics regarding these dams are summarized in Table 4-2 as provided by DSİ.

Table 4.2 Inspected dams by DSİ reconnaissance team after Sivrice Earthquake

Inspected dams	**Height (m)**	**Dam type**	**Distance to epicenter of earthquake (km)**
Dedeyolu Dam	35.7	Homogenous earthfill	19.3
Karakaya Dam	173	Concrete arch	16.1
Cip Dam	24	Center clay core earthfill	35.5
Kapıkaya Turgut Özal Dam	89.5	Center clay core rockfill	39.8
Keban Dam	207	Combined rockfill and concrete gravity	56.6
Boztepe Recai Kutan Dam	82	Clay core sand+gravel+rockfill	87.6

General layouts and typical cross sections of the Karakaya, Dedeyolu, Karakaya, Cip, Kapıkaya Turgut Özal, Keban and Boztepe Recai Kutan Dams are shown in Figures 4.95 to 4.99.

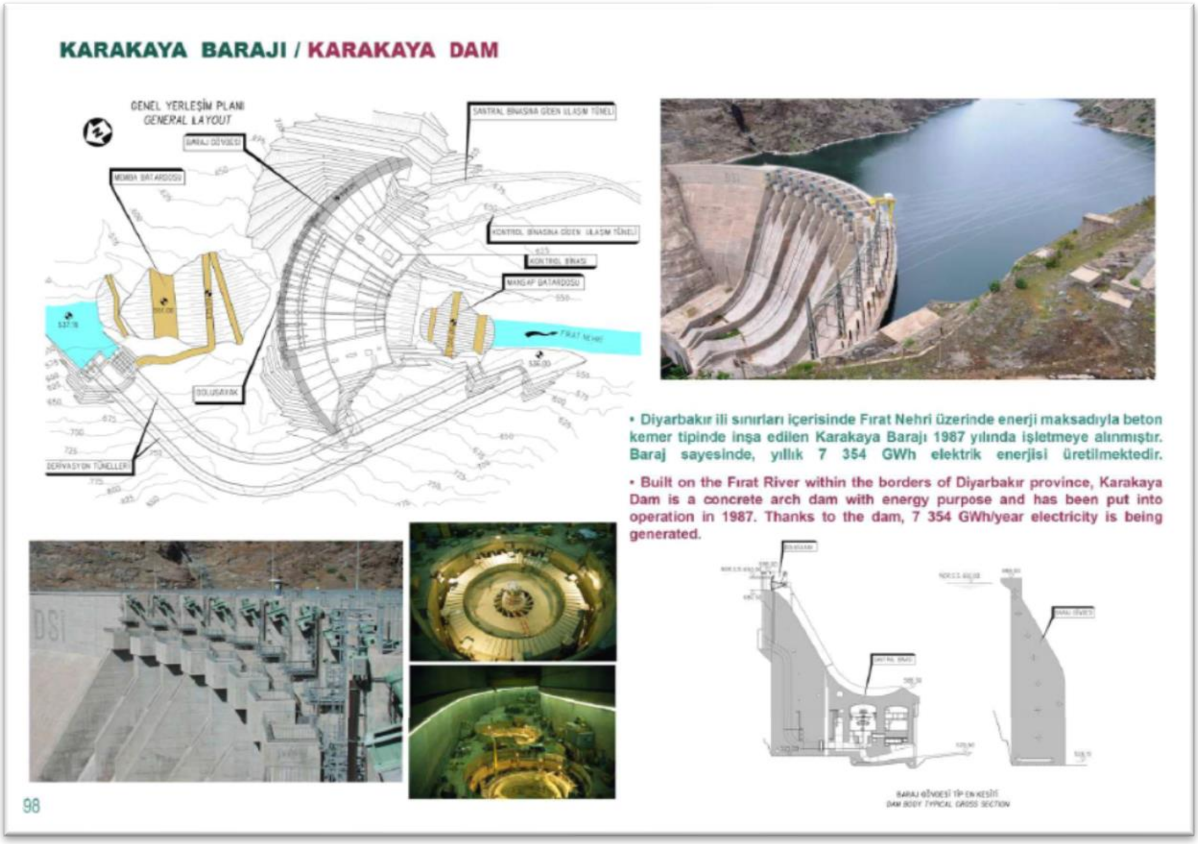

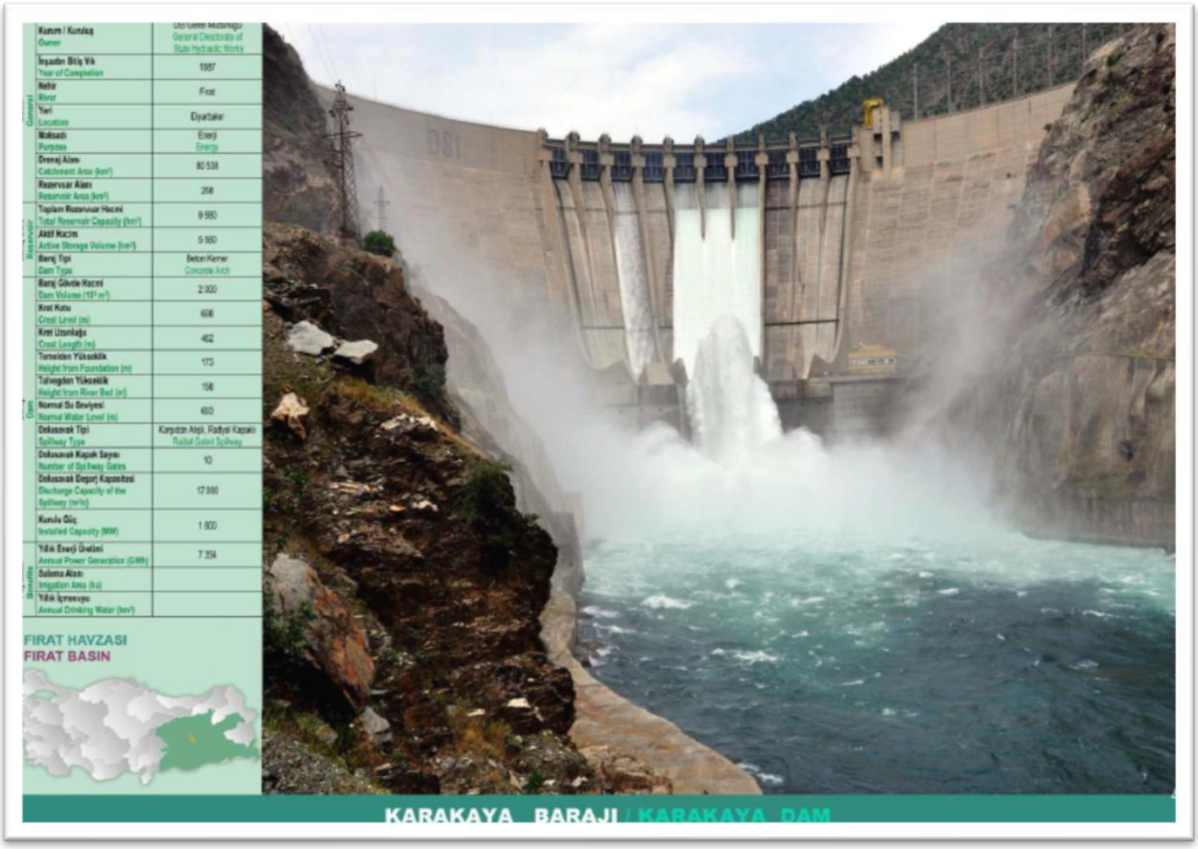

Figure 4.95 Karakaya Dam (DSİ)

Amacı : Sulama

Baraj ve gölü

Tipi	: Toprak dolgu
Gövde hacmi	: 446 000 m³
Kret kotu	: 1 008,00 m
Kret uzunluğu	: 1 024,40 m
Temelden yükseklik	: 24,00 m
Talvegden yükseklik	: 23,00 m
Temel jeolojik yapısı	: Kiltaşı, pliosen
Maksimum su kotu	: 1 006,50 m
Normal su kotu	: 1 004,50 m
Normal su kotunda göl hacmi	: 7,00 hm³
Normal su kotunda göl alanı	: 1,10 km²

Dolusavak

Tipi	: Karşıdan alışlı, kapaksız
Kret kotu	: 1 004,50 m
Kret uzunluğu	: 110,00 m
Proje taşkın piki	: 690 m³/s
Maksimum deşarj	:

Santral

Ünite adedi	: —
Ünite gücü	: —
Kurulu güç	: —
Yıllık enerji üretimi	: —
Sulama alanı	: 1 100 ha
Taşkın kontrol alanı	: —
Yıllık içmesuyu	: —

İnşaat : İnşaatına 1965 yılında başlanılmış ve 1965 yılında tamamlanmıştır.

Purpose : Irrigation

Dam and reservoir

Type	: Earthfill
Dam volume	: 446 000 m³
Crest elevation	: 1 008.00 m
Crest length	: 1 024.40 m
Height from foundation	: 24.00 m
Height from river bed	: 23.00 m
Geological formation of foundation	: Claystone, pliosen
Maximum water surface elevation	: 1 006.50 m
Normal water surface elevation	: 1 004.50 m
Reservoir volume at normal water surface elevation	: 7.00 hm³
Reservoir area at normal water surface elevation	: 1.10 km²

Spillway

Type	: Frontal type, ungated
Crest elevation	: 1 004.50 m
Crest lenght	: 110.00 m
Design flood peak flow	: 690 m³/s
Maximum discharge	:

Power Plant

Number of units	: —
Unit capacity	: —
Installed capacity	: —
Annual energy generation	: —
Irrigation area	: 1 100 ha
Flood control area	: —
Annual domestic water	: —

Construction : The construction was started in 1965 and completed in 1965

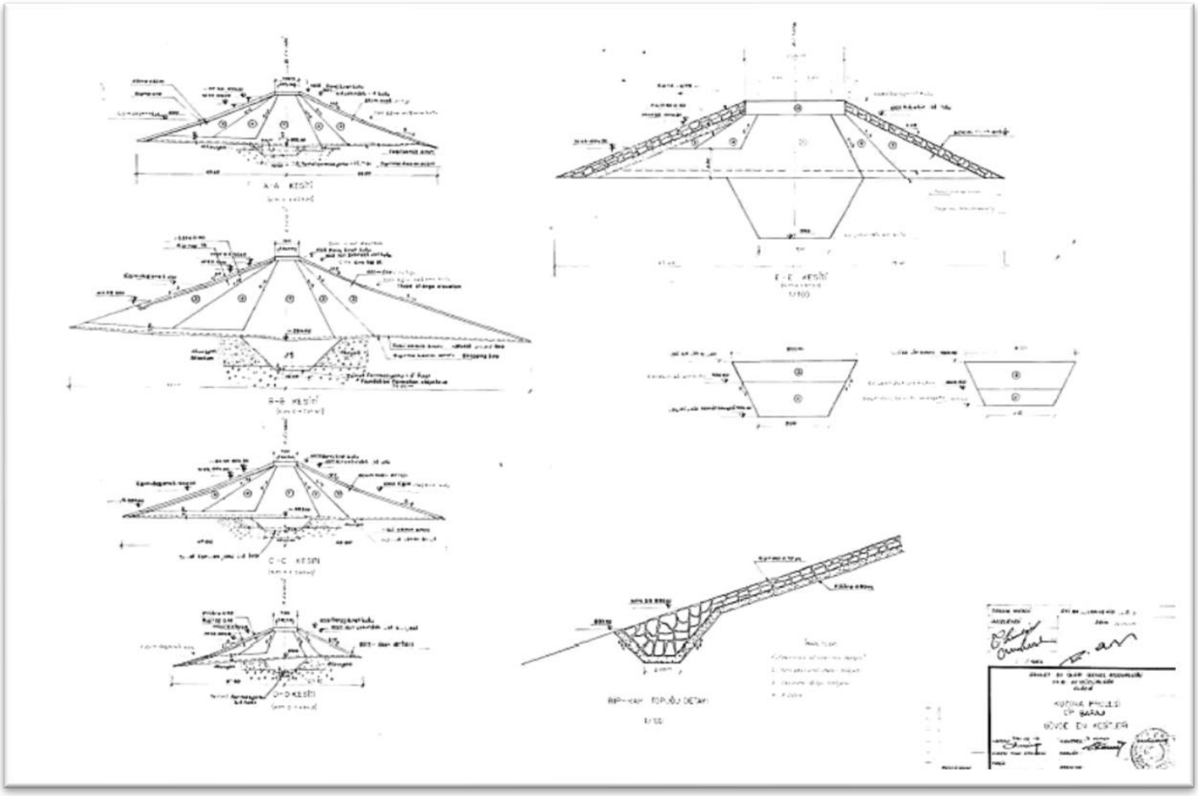

Figure 4.96 Cip Dam (DSİ)

As briefly discussed earlier, Kapıkaya Dam was visited during the 2nd day of reconnaissance studies. The upstream and downstream slopes of the dam, as well as abutments, inlet, spillway, dam body and crest were investigated in detail. No damage was observed at Kapıkaya Dam. Picture taken at Kapıkaya dam site were presented in Chapter 4.2.2, and will not be repeated again.

Figure 4.97 Kapıkaya Dam (DSİ)

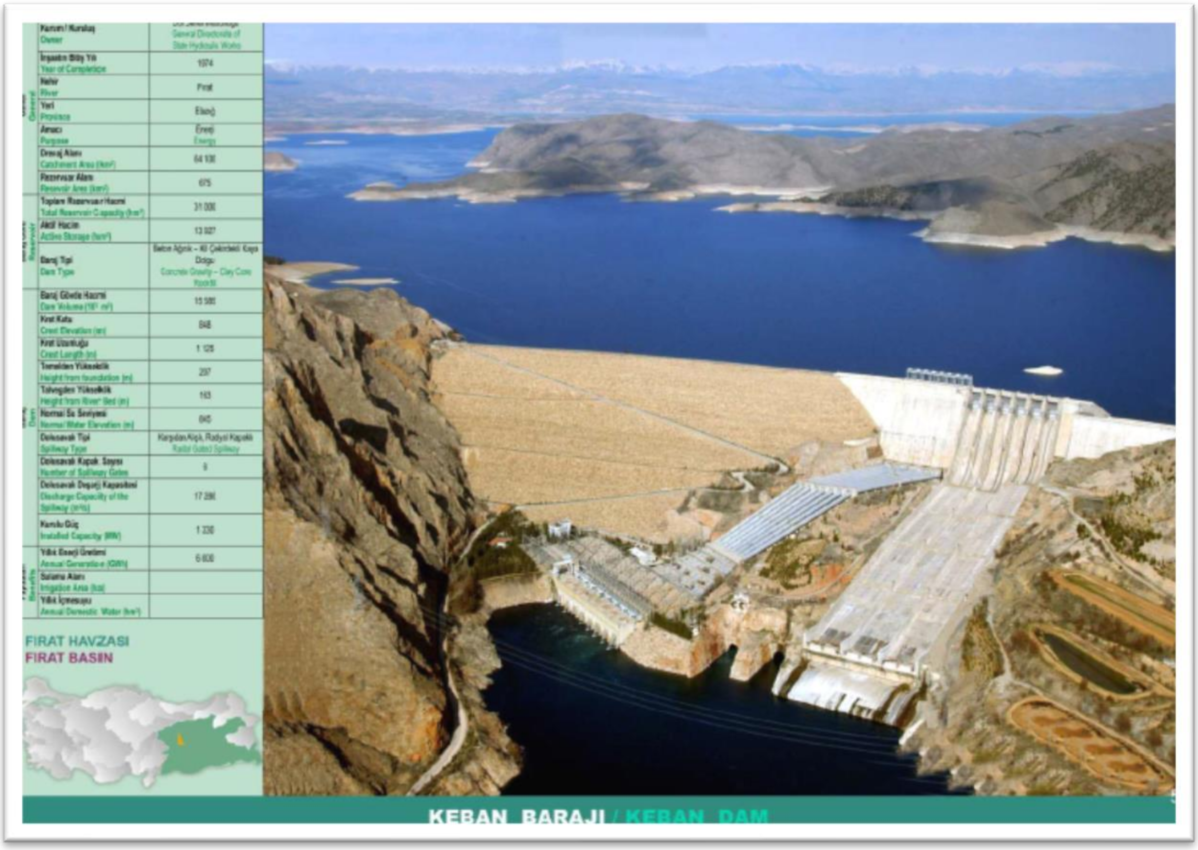

Figure 4.98 Keban Dam (DSİ)

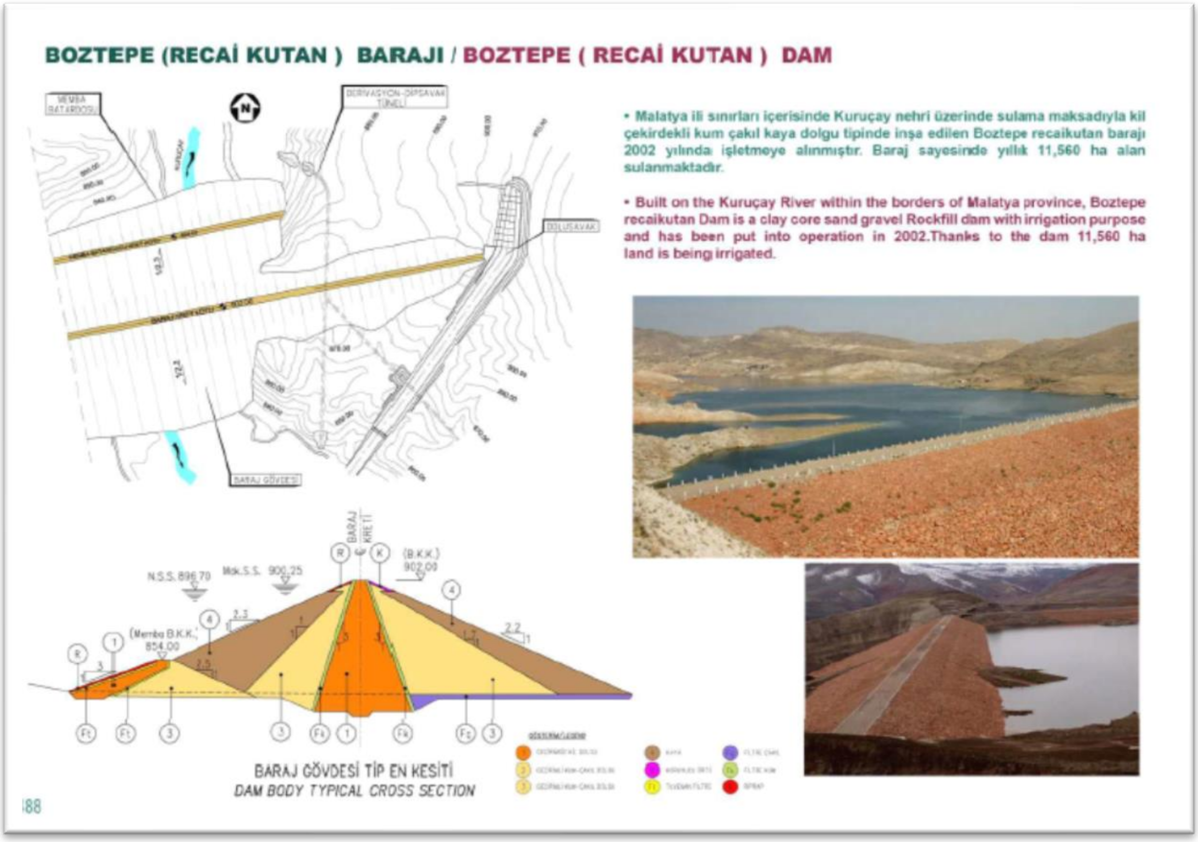

Figure 4.99 Boztepe (Recai Kutan) Dam (DSİ)

On the basis of reconnaissance studies performed by Dam Agency, no significant damage was reported to be observed at these dams after Sivrice Earthquake, except a limited extent longitudinal < 8 mm crack, as shown in Figure 4.100, observed on the crest of Dedeyolu Dam.

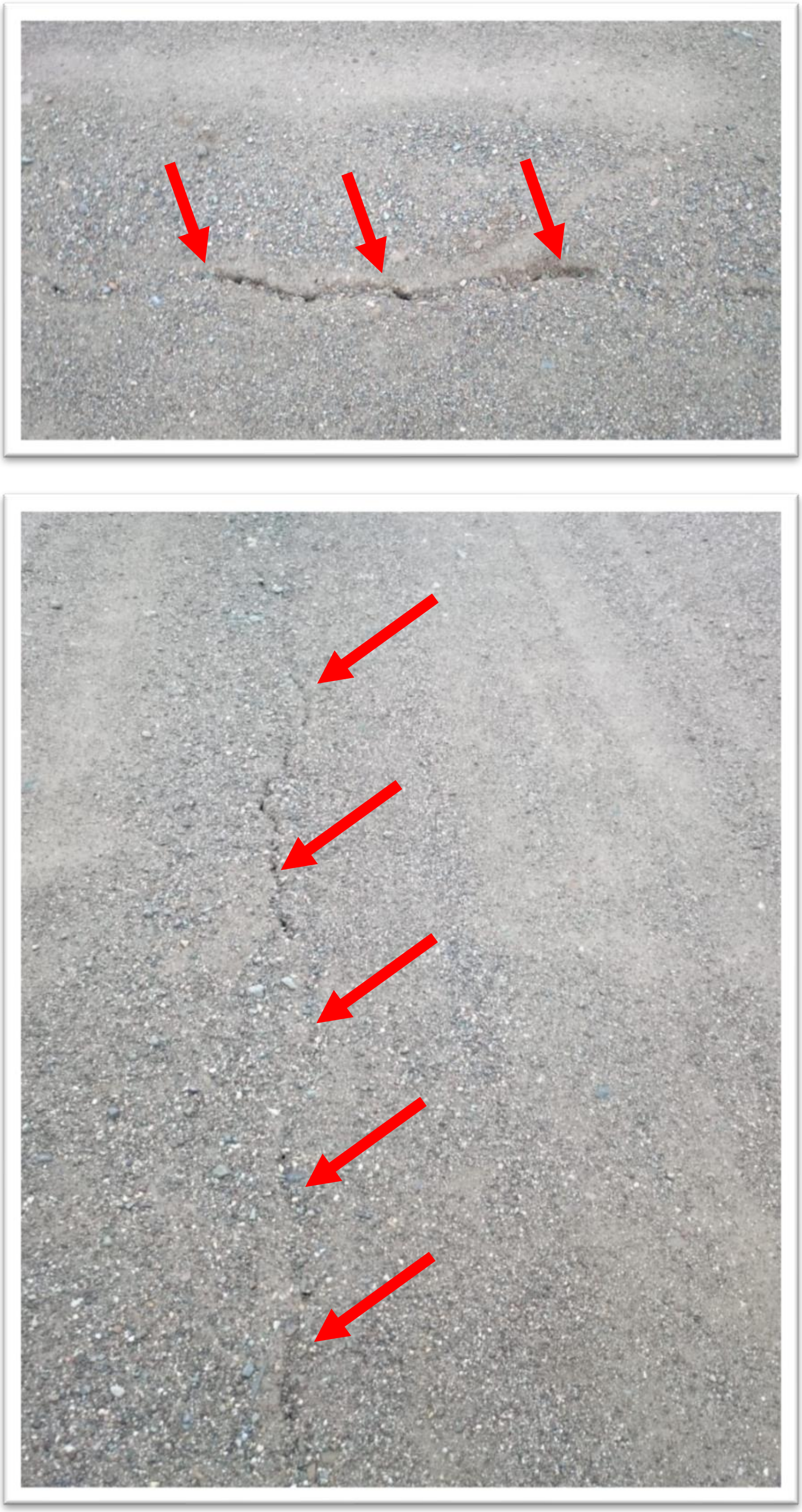

Figure 4.100 Longitudinal cracks on Dedeyolu Dam crest (Courtesy of S. Aydin, DSİ)

4.6 Railways

Based on Turkish Railway Authority (TCDD) database, two main railways passing through the East Anatolian Fault Zone were identified: i) Malatya-Elâzığ (Van-Gölü) and ii) Malatya-Diyarbakır (Güney Kurtalan) Express Trains. Their routes are shown in Figure 4.101.

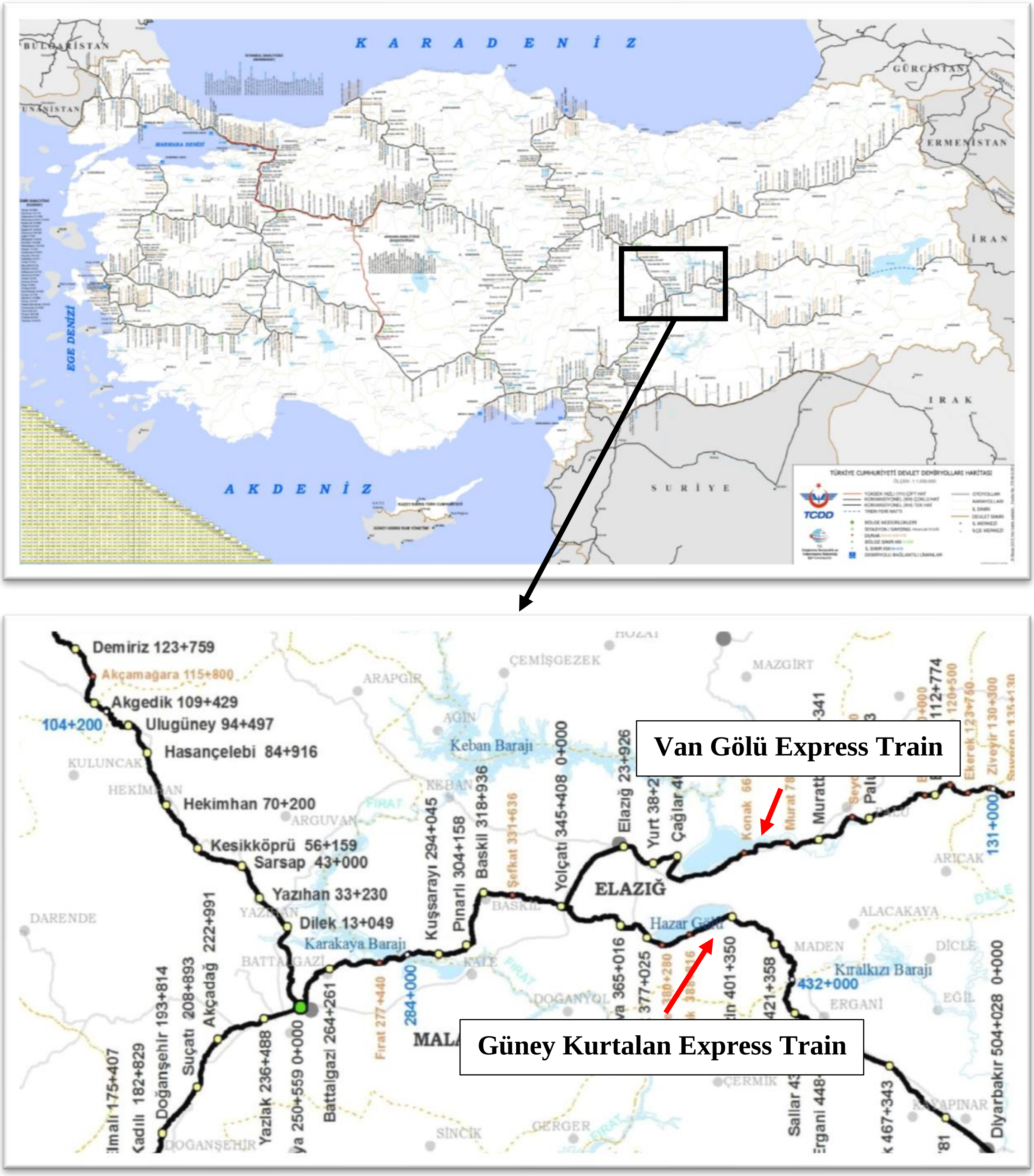

Figure 4.101 Turkish railway route map and the routes of Van Gölü and Güney Kurtalan Express Trains

As also briefly discussed earlier in Sections 4.2.1 and 4.2.2, no signs of track deformations or displacements were observed. As confirmed by the local railway authority, the railway system is in immediate service after the earthquake. A press news regarding a continuously monitored railway tunnel which cuts Eastern Anatolian Fault is shared below:

"Approximately three years ago, researchers from Yıldız Technical University discovered a railway tunnel built in the 1950s, located 50 m below the historical city in Palu, Elâzığ. The tunnel was directly cut by the Eastern Anatolian Fault so the tunnel is used as a monitoring station for EAF. Two creepmeters are placed on this tunnel to monitor the fault rupture and creep behavior of the EAF. 25 GPS stations were placed on the tunnel to retrieve the satellite information of the area and the tunnel was modeled in 3D with the help of laser scanner. According to the researchers' observation, there were no heavy damage on the Palu tunnel after the mainshock, however minor cracks were observed at the location of the East Anatolian Fault. It is advised that the tunnel should be monitored regularly, and some precautions should be taken for future events."

4.7 Seismic Soil Liquefaction and Lateral Spreading Cases Observed in Hazar Lake and Karakaya Dam Reservoir Shores

As discussed earlier, surface manifestations of seismic soil liquefaction triggering were observed in the form of lateral spreading and sand boils along the shoreline of Hazar Lake, Fırat River and Karakaya Dam Reservoir shores. Research team investigated the Hazar Lake shores during day 1 and Fırat River during day 2 of the reconnaissance studies.

By the natural shores of Hazar Lake, seismically-induced lateral spreading, sand boils and excessive volumetric settlements were observed. A map, summarizing consolidated field observations along the shores of Hazar Lake is shown in Figure 4.102. In Figure 4.102, green pins indicate non-liquefied sites, red pins indicate sites with surface deformations along with abbreviations of type of ground failure; RF: Rock fall, LS: Lateral spread, VS: Volumetric settlement, SB: Sand Boil.

Figure 4.102 A summary of ground failure observations along the shores of Hazar Lake (Green pins indicate Non-Liquefied sites, Red pins indicate sites with surface deformations, RF: Rock fall, LS: Lateral spread, VS: Volumetric settlement, SB: Sand Boil)

Figure 4.103 A summary of ground failure observations along the shores of Fırat River and Malatya-Elâzığ Route
(Green pins indicate Non-Liquefied sites, Red pins indicate sites with surface deformations, RF: Rock fall, LS: Lateral spread, VS: Volumetric settlement, SB: Sand Boil)

By Kale Village, at the shores of Fırat River, surface manifestations of seismic soil liquefaction in the form of sand boils were observed. A map, summarizing consolidated field observations along the shores of Fırat River is shown in Figure 4.103.

In day 1, surface manifestation of soil liquefaction in the form of sand boils and lateral spreading were mapped. The extent of lateral deformations was mapped as 3-5 cm along a 90 m long and 23 m wide zone at the second stop in the vicinity of Sivrice Dock, as shown in Figure 4.104. Figures 4.105 and 4.106 present the photos of lateral spreading site taken during field investigations.

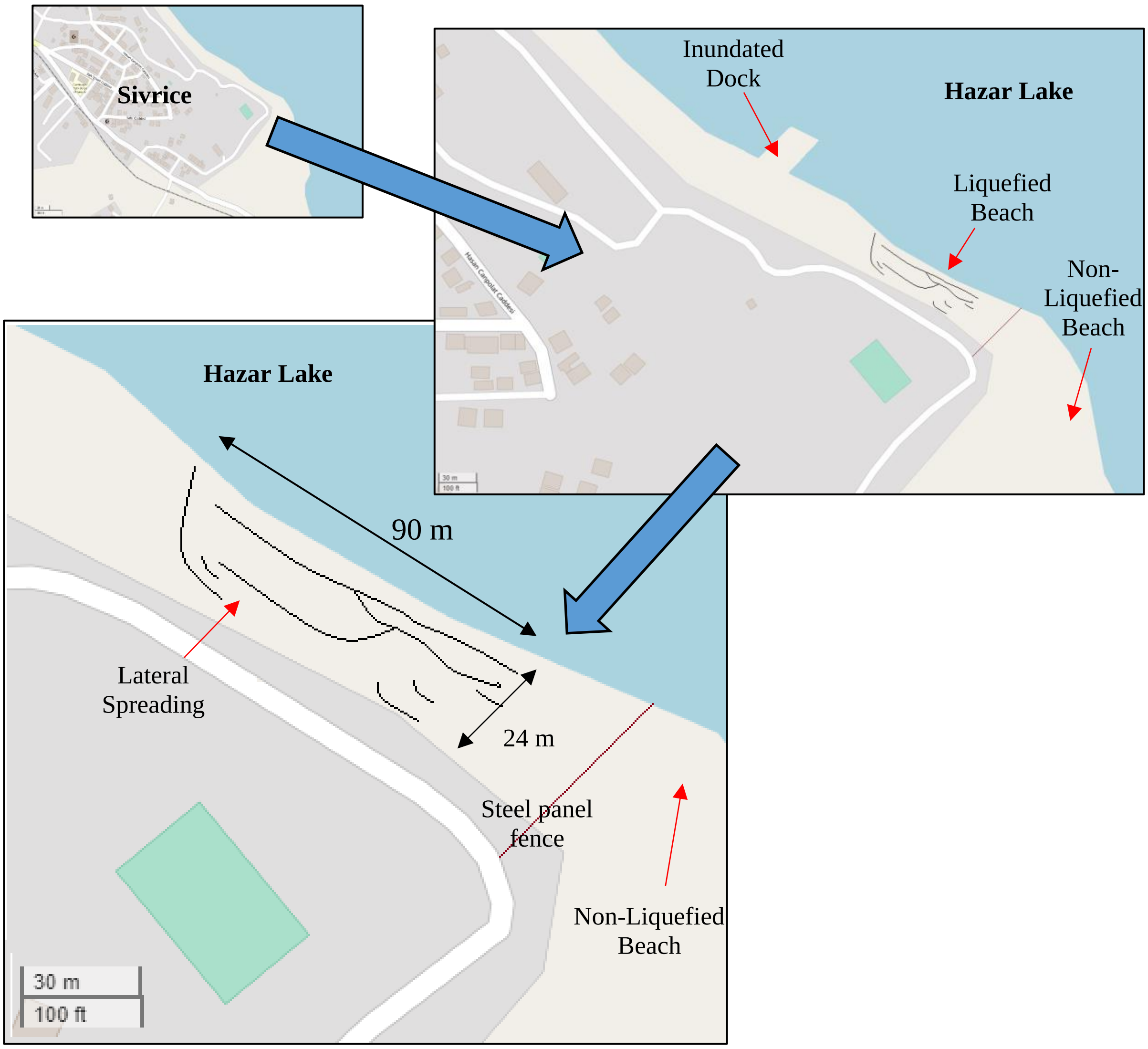

Figure 4.104 A sketch of lateral spread deformations at 2nd stop
(38°28'10.0"N 39°17'03.6"E / 31.01.2020 / 12:11)

Figure 4.105 Deformations and cracks due to lateral spreading observed along Hazar Lake (2nd stop)
(38°26'50.7"N 39°18'56.9"E / 31.01.2020 / 12:21 & 38°26'50.5"N 39°18'56.9"E / 31.01.2020 / 12:28)

Figure 4.106 Deformations and cracks due to lateral spreading observed along Hazar Lake (2nd stop)
(38°26'50.8"N 39°18'55.6"E / 31.01.2020 / 12:34 & 38°26'50.3"N 39°18'57.1"E / 31.01.2020 / 12:27)

No signs of liquefaction were observed at a natural beach neighboring the lateral spreading site as shown in Figure 4.107. This beach was observed to have a milder slope when compared to the lateral spreading site shown in Figures 4.104-4.105.

Figure 4.107 No ground failure at the natural beach neighboring the lateral spreading (2nd stop)
(38°26'48.9"N 39°18'59.4"E / 31.01.2020 / 13:08 & 38°27'58.0"N 39°20'42.4"E / 31.01.2020 / 13:08)

Ground deformations were observed due to liquefaction at 8th and 15th stops along Hazar Lake as shown in Figures 4.108 and 4.109. Sand boils were mapped, and soil samples were retrieved from these locations. A series of sieve analysis tests has been performed at METU Soil Mechanics Laboratory. Based on the results of these tests, samples were reported to be potentially liquefiable as also will be discussed in the next section.

Figure 4.108 Surface manifestations of soil liquefaction in Hazar Lake (8th stop)
(38°27'49.7"N 39°24'03.3"E / 31.01.2020 / 14:16 & 38°27'50.0"N 39°24'02.5"E / 31.01.2020 / 14:20)

Figure 4.109 Surface manifestations of soil liquefaction in Hazar Lake (15th stop) (38°29'34.6"N 39°21'03.7"E / 31.01.2020 / 17:11 & 38°29'30.6"N 39°20'57.7"E / 31.01.2020 / 17:01)

In day 2, surface manifestation of soil liquefaction in the form of sand boils were mapped along Kale shores. Figures 4.110 and 4.111 present the photos of the sand boils taken at the shores of Kale Village.

Figure 4.110 Surface manifestation of soil liquefaction at Kale Village shores (26th stop) (38°25'23.6"N 38°45'39.0"E / 01.02.2020 / 12:18)

Figure 4.111 Surface manifestation of soil liquefaction at Kale Village shores (26th stop)
(38°25'20.2"N 38°45'33.2"E / 01.02.2020 / 12:25)

Disturbed samples were taken from the surface of the liquefied areas. The locations of sites from where 6 samples (Hazar Lake) and 4 samples (Kale Village) were taken, are shown in Figure 4.112 and 4.113. A map showing these locations are also presented in Figure 4.114. These samples were tested at METU Soil Mechanics Laboratory to determine the soil-type, grain size and consistency characteristics. The results are comparatively presented with the particle size distribution ranges common for potentially liquefiable soils (Tsuchida, 1970), as given in Figure 4.115. Sieve analysis test results are summarized in Table 4-3. Based on USCS, most of the samples retrieved from sand boils were classified as SP (poorly graded sand) and SM (silty sand).

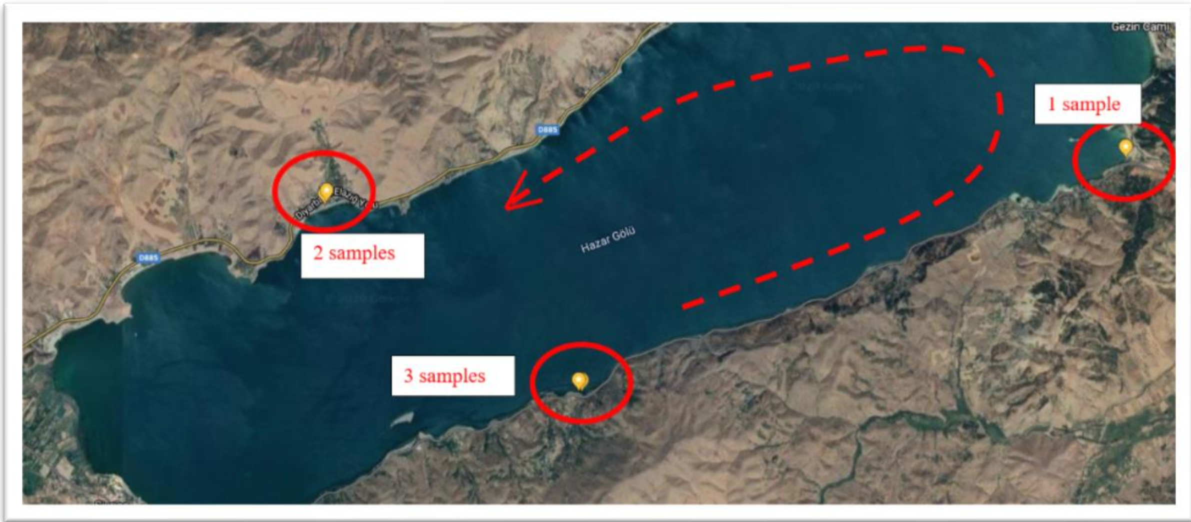

Figure 4.112 Location of sand boil samples taken from Hazar Lake shores

Figure 4.113 Location of sand boil samples taken from Kale Village shores

Figure 4.114 Location of the samples taken during site investigation (general view)

Table 4.3 Grain size distribution of sand ejecta

Region	Coordinates	Gravel %	Sand %	Fines %	Silt %	Clay %	D_{10} (mm)	D_{30} (mm)	D_{60} (mm)	C_u*	C_c*	Soil Type
Hazar Lake	38.463-39.4009	11.0	87.6	1.4			0.33	0.42	0.53	1.61	1.01	SP
	38.463-39.4007	28.8	41.1	30.1	27.6	2.5	0.02	0.075	0.6	30.0	0.47	SM
	38.499-39.506	4.2	80.9	14.9	11.1	3.8	0.02	0.24	0.42	21.0	6.86	SM
	38.492-39.35	10.0	87.0	3.0			0.32	0.65	1.7	5.31	0.78	SP
	38.492-39.351	4.1	83.5	12.5	10.6	1.9	0.06	0.16	0.25	4.17	1.71	SM
	38.463-39.4002	4.2	72.7	23.1	19.6	3.5	0.03	0.09	0.17	5.67	1.59	SM
Kale Village Lake side	38.424-38.762	36.4	57.5	6.2			0.09	0.2	2.9	32.2	0.15	SP-SM
	38.421-38.759	3.4	95.4	1.3			0.23	0.36	0.49	2.13	1.15	SP
	38.421-38.757	4.4	90.4	5.2			0.25	0.47	0.91	3.64	0.97	SP-SM
	38.424-38.762	26.2	70.8	3.0			0.32	0.5	1.44	4.50	0.54	SP

* $C_u = D_{60}/D_{10}$, $Cc = D_{30}^2/(D_{10} * D_{60})$

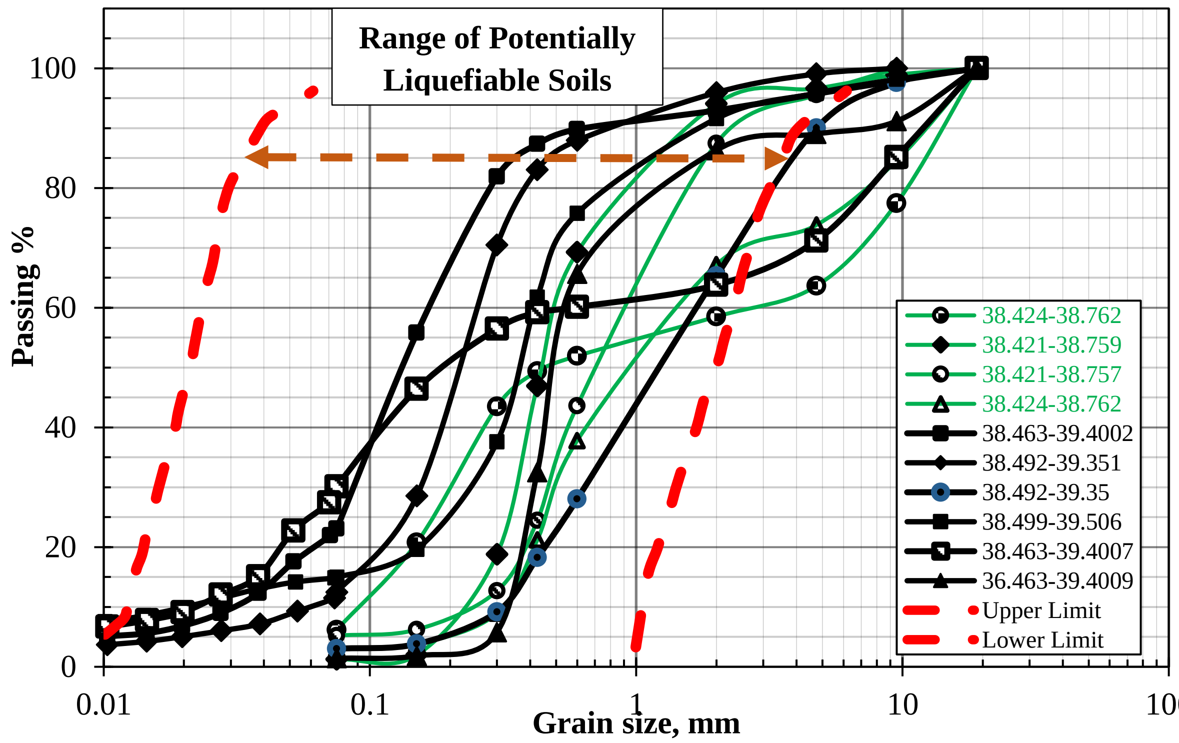

Figure 4.115 Particles size distribution curves of the sand ejecta taken from liquefied sites (Black lines are obtained from Hazar Lake region and green lines from Kale Village side, respectively)

Although there exist free field soil sites with highly potential for liquefaction triggering around the shores of Hazar Lake and Fırat River, due to lack of urbanization in these areas, the contribution of liquefaction triggering to observed structural damage is judged to be none, except Sivrice Dock failure.

Chapter 5
Observations on the Performance of Reinforced Concrete Structures

Prof. Erdem CANBAY[1]

Prof. Barış BİNİCİ[1]

Res. Asst. Erhan BUDAK[1]

[1] *Middle East Technical University*

5.1 Introduction

This section summarizes the observations of the field study trips performed on January 26-29, and February 6 after the Elâzığ earthquake. In these reconnaissance surveys, mainly the reinforced concrete buildings in the city center of Elâzığ were examined. According to the latest data from the Ministry of Environment and Urbanization, there are 263 collapsed, 7,698 severely damaged, and 1,540 medium damaged buildings among the investigated 61,152 buildings (https://www.csb.gov.tr/bakan-kurum-elazigdaki-hasar-tespit-calismalarini-anlatti-bakanlik-faaliyetleri-29711). Among these, 558 buildings need urgent demolition, and 201 of them have already been demolished. Only 3 buildings, however, collapsed in Elâzığ city center. All other collapsed buildings were in the districts and villages close to the epicenter of the earthquake.

As mentioned in the first part of the report, an earthquake of $M_W = 6.8$ occurred on January 24, 2020, at 20:55 local time. The earthquake epicenter is near the village of Çevrimtaş in Sivrice district of Elâzığ province. The event was a left-lateral strike-slip fault rupture on the East Anatolian Fault Zone (EAFZ), along the Pütürge segment extending in the NE-SW direction. A maximum ground acceleration of approximately $0.29g$ was recorded by the Disaster and Emergency Management Presidency (AFAD), in Sivrice district, which is located on the fault direction, and 24 km away from the epicenter. The maximum ground acceleration recorded in Elâzığ center is only $0.15g$. Earthquake ground motion level-2 (DD-2), also called the *standard* design earthquake ground motion, characterizes the rare earthquake ground motion where the spectral magnitudes are exceeded by 10% in 50 years, and the corresponding return period is 475 years. Turkey Earthquake Hazard Map (tdth.afad.gov.tr) gives DD-2 values at the epicenter and Elâzığ city center as $0.67g$ and $0.38g$, respectively. In other words, the ground acceleration measured in Elâzığ center was significantly lower and similar to the *frequent* earthquake ground motion (DD-3, 50% probability of exceeding spectral magnitudes in 50 years, and a corresponding return period 72 years) since the maximum ground acceleration DD-3 value is $0.148g$, according to the Turkey Earthquake Hazard Map.

First of all, the concrete quality should be discussed. For the buildings older than 30 years, concrete quality was very low since ready-mix concrete was not usually used in those days. Generally, ready-mix concrete has been used in the buildings since 2000. The visual appearance of concrete for these structures was better. The conversations with the occupant during the investigations showed that some of them were the contractors of their own buildings or a close relative was involved with the construction. This is an indication of the knowledge that they had about the construction stages of the buildings. All of them consistently told that water was added to the concrete mixers waiting in the construction site before casting concrete to improve workability. The additional water to the concrete mix surely affected the concrete strength adversely. Besides, they all mentioned that concrete curing was not done appropriately. These two factors were believed to result in low strength concrete. The conversations with the owners revealed that the concrete compressive strength and the earthquake resistant nature of the buildings were significantly improved after the ready-mix concrete era starting in around 2000. However, as a result of the ignorance regarding the concrete-mix, the curing of concrete, and the reinforcement placement, it appears that the current concrete strengths may still be below the target strength values.

5.2 System Irregularities

The reconnaissance study reveals that for the buildings 20 years or younger, the earthquake forces were generally taken into consideration during the design because the column sizes of these buildings were much larger than the older buildings and some of them even had shear walls. However, even in these types of structures, low damage was observed under $0.15g$ ground acceleration, and non-structural elements had usually moderate/heavy damage. When the structures with such an unexpected level of damage is examined, it is found out that there is no proper seismic lateral force resisting system, they do not have a continuous frame system, and an irregular system is created to comply with the architectural drawing. In short, while the large column sizes could prevent total collapse or heavy structural damage, the desired level of performance could not be achieved for the buildings with irregular systems.

Figure 5.1 shows a beam spanning eccentrically to the column. Simply to comply with the architecture, such off-axis systems are designed. The structural system irregularity is very common since the civil engineer and the architect do not work together while preparing the preliminary project, and mostly, the architects decide on the structural system. Generally, a proper and continuous load path is not formed, and beams cross over with irregularities. Figure 5.2 shows a typical example of beam irregularity.

Irregular axis and beam system were found in all the buildings examined. An interesting irregularity is given in Figure 5.3. The cantilever balcony slab on the left of the figure is supported by the cantilever beam. In other words, a cantilever carries another cantilever. As a result, very serious damage occurred in the building.

Figure 5.1 Eccentric beam

Figure 5.2 Beam irregularity

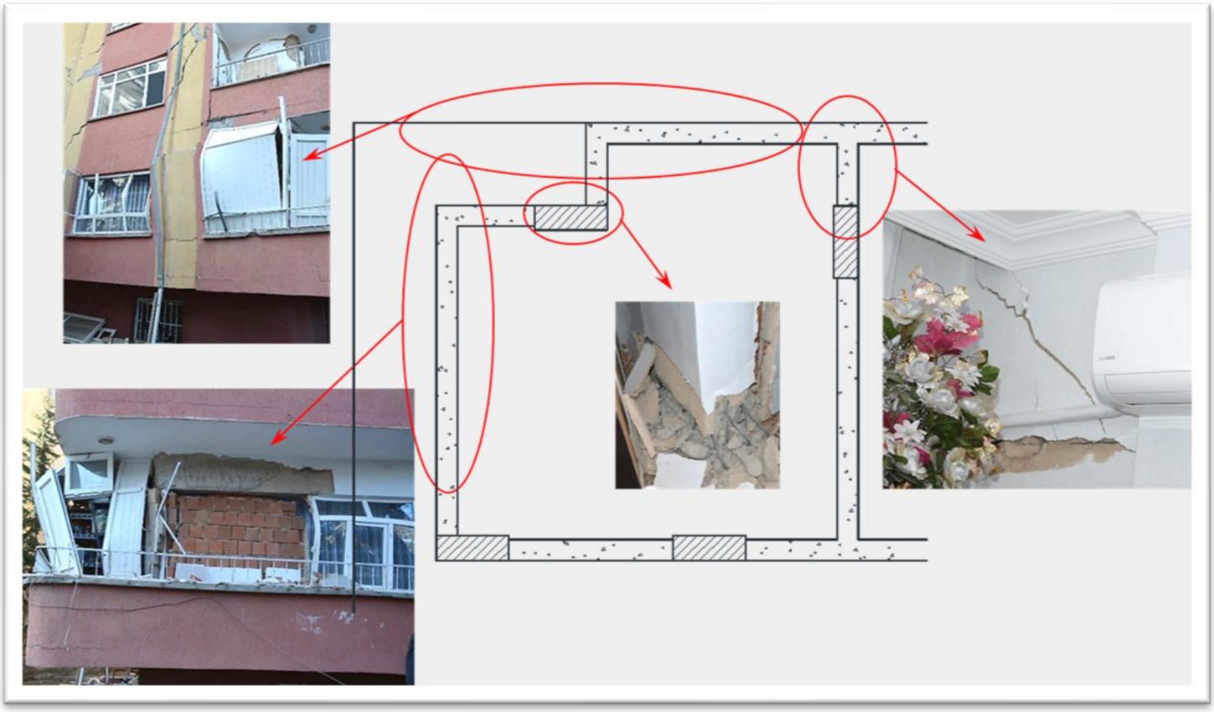

Figure 5.3 System irregularity

The column damaged due to the irregularity given in Figure 5.3 is also presented in more detail in Figure 5.20. Another irregularity problem of this building is that it was designed as a star shape. The satellite image of the building is given in Figure 5.4. There is an elevator core in the middle section. However, there is no core shear here. Only the backside of the elevator is a shear wall, but the side faces are brick walls. Considering the current severely damaged state of the building, it can be said that the star shape does not provide a proper lateral load resisting system for the building during the earthquake.

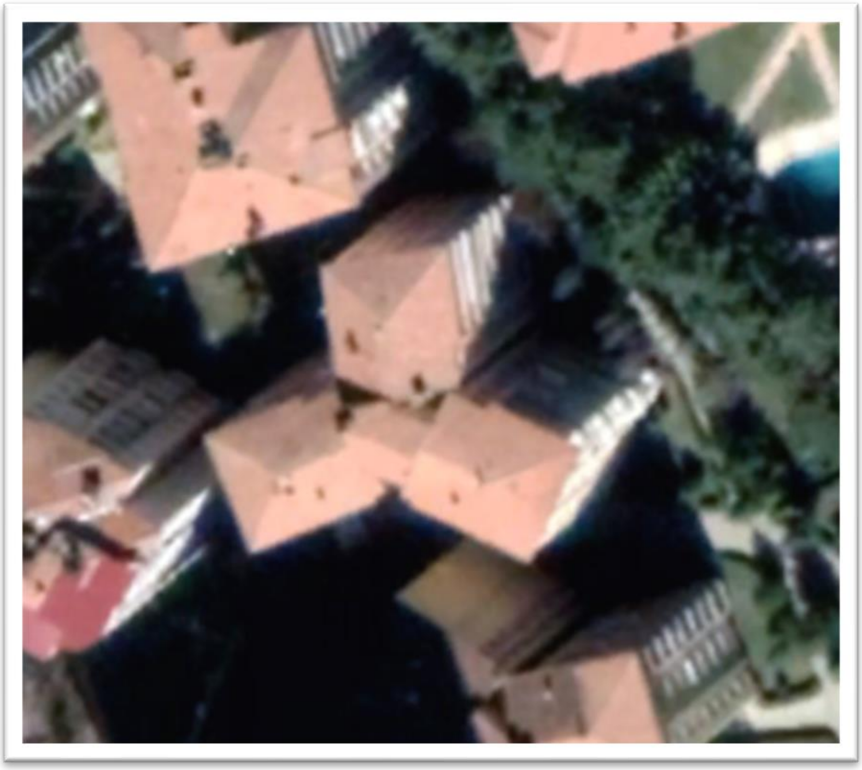

Figure 5.4 Aerial view of the building

5.3 Structural Damages

In this section, the observation results on 30 buildings are reported. Unfortunately, structural damages similar to those observed in the previous earthquake observations are repeated after this earthquake as well.

5.3.1 Total Collapse

There are 3 buildings collapsed totally in the city center of Elâzığ, Figure 5.5 and Figure 5.6. Unfortunately, these buildings could not be examined closely since the search and rescue activities were continuing. After the search and rescue works, no significant clues for total collapse could be found since the buildings have already turned into debris. However, as a result of the observations made only from outside, the usual weaknesses were realized: low concrete quality, insufficient stirrups, 90° stirrup hooks, no cross-ties, weak column-strong beam, absence of shear walls, insufficient beam-column joints.

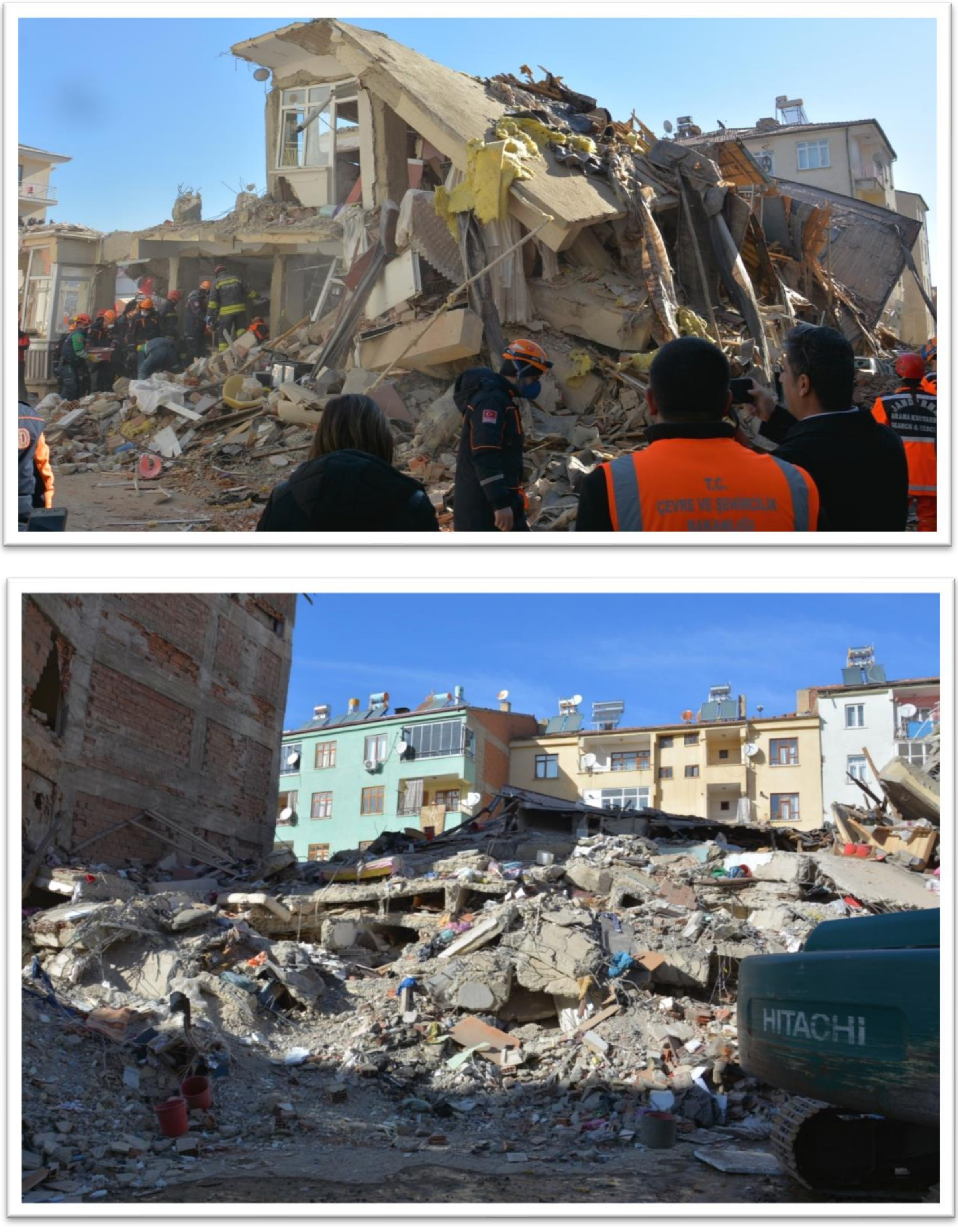

Figure 5.5 Total collapsed buildings in Elâzığ city center

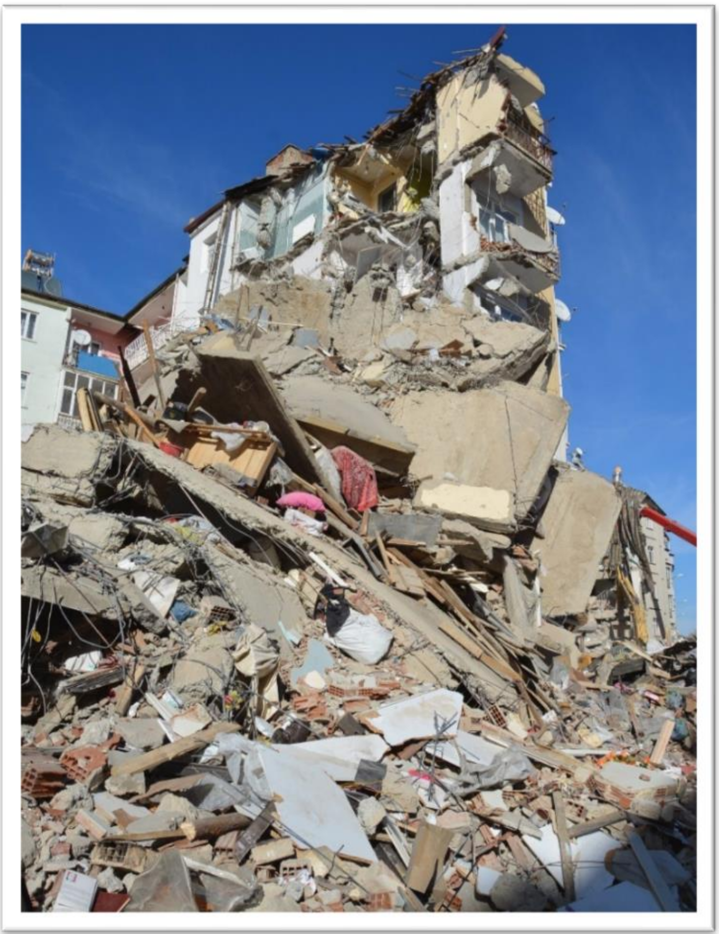

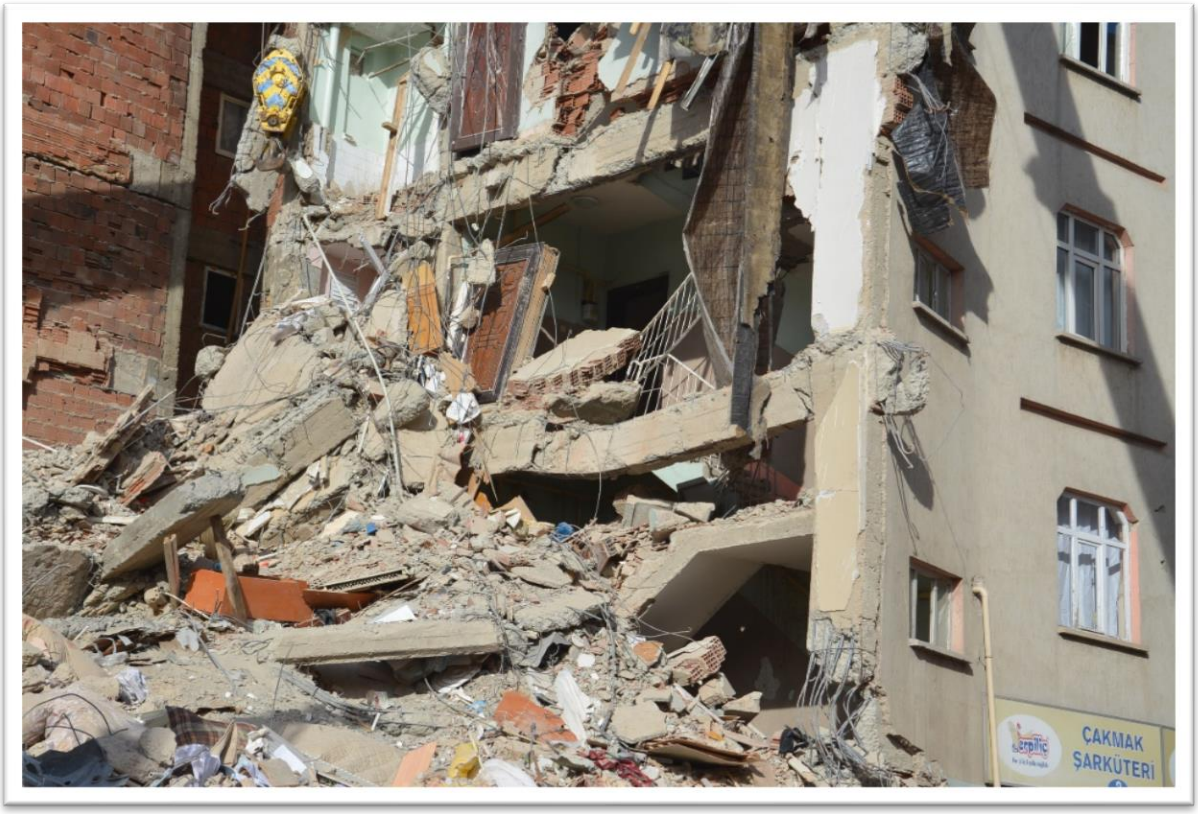

Figure 5.6 Total collapsed buildings in Elâzığ city center

5.3.2 Partition Wall Damages

Partition wall damage is very common damage type in all structures examined. Infill wall damages were observed either at the partition wall and beam-column interfaces or as diagonal X-cracks on the partition walls or collapses of the partition wall in the out-of-plane direction partially or entirely (Figure 5.7- 5.13). These cracks indicated insufficient lateral stiffness of the structure. Since the partition walls were placed without any gaps with the surrounding beams and columns, cracks were observed on the walls even at low displacement demands. The cracks on the partition walls have usually two major drawbacks. First, the occupants who see the cracks on the walls do not want to enter these buildings. In other words, these cracks affect people psychologically and cause them to stay outside in tents unnecessarily under harsh conditions. Secondly, it can mislead damage identification teams to categorize the building incorrectly, usually to a higher damage level.

In Figure 5.7 and Figure 5.8, a general view of the partition wall damages is given from the exterior of the buildings. Typical partition wall cracks in the inspected buildings are given in Figure 5.9 and Figure 5.10. A heavy wall crack is given in Figure 5.11. Such wall separations have been much less common. As can be seen in Figure 5.12, it is highly probable that the exterior partition walls, which were especially made of double layers, fell down. The heat insulation material was placed between the two thin bricklayers. Walls on overhangs aggravates such wall damage. Figure 5.13 shows a completely damaged exterior wall due to out of plane deformations. This kind of collapses are one of the important types of damage that can cause loss of life and property.

Figure 5.7 Partition wall cracks on the beam-column boundary, exterior

Figure 5.8 Diagonal partition wall crack, exterior

Figure 5.9 Partition wall cracks on the beam-column boundary, interior

Figure 5.10 Diagonal partition wall crack, interior

Figure 5.11 Heavy diagonal partition wall crack

Figure 5.12 Partition wall fall

Figure 5.13 Out of plane failure of the partition wall

5.3.3 Heavy Overhangs

The footprint of the building, and the plan area of the upper floors are different in the buildings of Elâzığ but also true for the buildings in the rest of the country. The upper floors are enlarged in plan with cantilever overhangs to gain further space. These cantilever overhangs are usually excessive and crack under the load of the exterior walls on overhangs. These parts of the building can be damaged heavily during earthquakes.

Figure 5.14 and Figure 5.15 show pictures of wall cracking observed at the corners of heavy overhangs. As can be seen in Figure 5.12 above, the exterior walls in the overhangs can fall. Such accidents can cause injury or even death.

Damages in heavy overhangs are not only limited to the partition walls but also the structural system. Bending and shearing cracks after an earthquake is a common problem in the beams of overhangs, Figure 5.16.

Figure 5.14 Heavy overhang damages

Figure 5.15 Heavy overhang damages

Figure 5.16 Cantilever beam damage of overhangs

5.3.4 Column and Shear Wall Damages

A rectangular column that sustained significant damage is given in Figure 5.17 as an example. All typical deficiencies regarding the column detailing are present in this picture. Plain bars are used, stirrup spacing is large, stirrups are not closely spaced at column ends, stirrup hooks are left at 90°, no cross-ties are used, and concrete quality is poor. Site prepared concrete with unwashed, dirty river sand and aggregate was used in the construction of this building.

Shear damage typically seen in columns due to insufficient transverse reinforcement is given in Figure 5.18. Since the stirrups were not closely spaced at the column ends, plastic hinging can be seen in the end regions as shown in Figure 5.19. Frame-wall interaction augmented this damage as well. This damage occurred due to the lack of sufficient confinement at the upper end of the column. Figure 5.20 shows heavy damage at the bottom of the column. The damage here is beyond plastic hinging, almost reaching the disintegration of the column.

In a limited time, only the buildings that were reported to us as moderate or heavy damaged were tried to be inspected. Most of the buildings did not have shear walls. An example for the shear wall damage is given in Figure 5.21. The first photo contains typical shear damage. The second one shows a sliding movement. Most likely, the dowel bars from the foundation end at this level. Therefore, such sliding deformation appears at this level.

Figure 5.17 A typical column example

Figure 5.18 Shear failure in columns

Figure 5.19 Plastic hinging at the top of the column

Figure 5.20 Collapse at the bottom of the column

Figure 5.21 Shear wall damages

5.3.5 Beam Damages

Bending and shear damages are observed at the ends of the beams after the earthquake. Figure 5.22 shows bending cracks at the beam ends.

Figure 5.22 Beam bending cracks

In Figure 5.23 and Figure 5.24 provide observed extensive cracking on beams and penetrating toward the slab. A shear crack on a cantilever beam was given formerly in Figure 5.16

Figure 5.23 Beam shear cracks

Figure 5.24 Beam shear cracks

5.3.6 Pounding Damages

The construction of adjacent buildings, which is widely applied in our country, is also frequently seen in Elâzığ. Minimum separation distance given by the regulations should be followed between the adjacent structures. Thus, the structures will not hammer and damage each other during an earthquake. However, it is observed that the structures in Elâzığ are constructed completely adjacent, without any gaps between them.

Generally, buildings are constructed by leaving waste molds between buildings. Sometimes even the adjoining building is used as a formwork without proper formwork. Figure 5.25 shows a column cast without formwork between the adjacent building. Even the structure built later does not put up a wall but uses the wall of the next building.

The most extensive damage seen in adjacent buildings in Elâzığ is the cracks seen at the interface of the buildings. An example of such a crack is given in Figure 5.26. This crack is only caused by covering the intermediate joint gap with plaster and is not a structural damage. However, it has a negative impact on the occupants.

Structural damage to adjacent buildings occurs if buildings hit each other during an earthquake. Buildings especially with different floor levels can cause heavy damage to each other by the impact of hammering. Among the investigated buildings, only one building had serious damage at this level. Pounding damage is seen in Figure 5.27. The impact of pounding damaged the beam-column joint heavily.

Figure 5.25 Column cast without formwork

Figure 5.26 Adjacent building damage

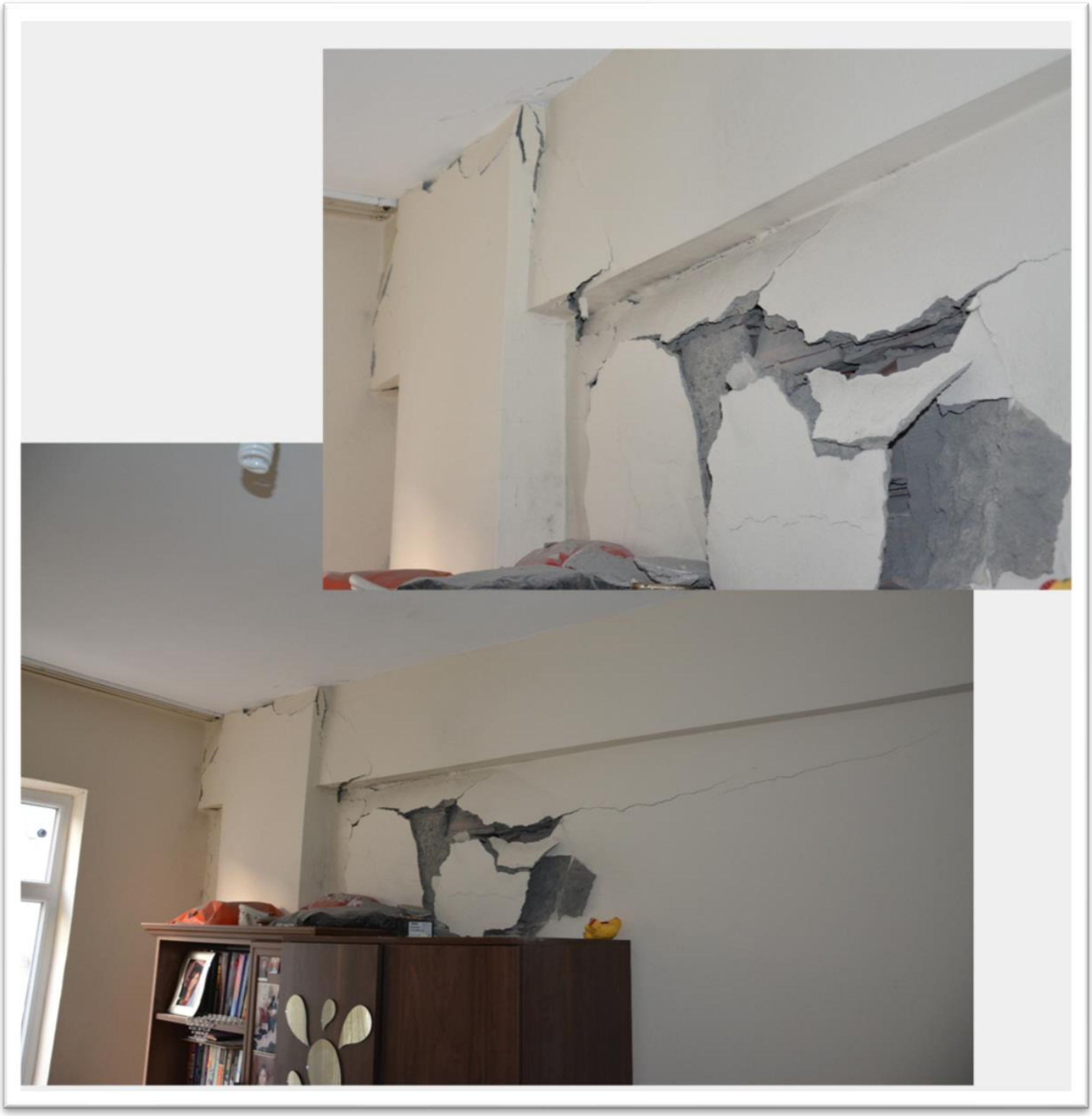

Figure 5.27 Pounding damage

5.3.7 Gable and Parapet Wall Damages

As in all earthquakes investigated to date, gable walls and parapet walls constructed improperly have also been damaged in Elâzığ. Brick walls falling from the roof of the buildings pose great danger. Examples of these damages are given in Figure 5.28.

Figure 5.28 Gable and parapet wall damages

5.3.8 Soil Subsidence

A very limited number of soil settlements were observed after the earthquake. This damage was seen in the buildings where the ground floor was built by casting lean concrete directly onto the ground. Figure 5.29 shows the floor cracking caused by the soil subsidence. The sinking in this base floor slab sitting directly on the soil is approximately 10 cm. Figure 5.30 shows damage to the walls due to soil subsidence. Widespread heavy wall cracks due to this soil damage were observed on the ground floors of several buildings side by side, constructed in the same type.

Figure 5.29 Damages caused by soil subsidence

Figure 5.30 Wall damage due to soil subsidence

5.4 The Performance of a Strengthened Building

In the city center of Elâzığ, there is an almost identical building next to the totally collapsed building. The basement of this building was strengthened previously. For this purpose, 7 columns in the basement were rehabilitated with reinforced concrete jacketing. The jacketing details, concrete strength, and reinforcement details are uncertain in terms of engineering design and application. However, even if the strengthening was applied incorrectly, it prevented the building from total collapse. Besides, the building damage remained limited, with mostly infill wall damage. This practice shows the importance of strengthening buildings against earthquakes. While one building totally collapsed, the identical survived the earthquake almost smoothly.

Figure 5.31 Column strengthening with reinforced concrete jacketing

5.5 Concluding Remarks

Based on the reconnaissance survey conducted in Elâzığ after the earthquake, the following remarks can be made:

- Although the intensity of the ground motion at Elâzığ city center was significantly below the design level earthquake, moderate and severe damages were observed in many buildings.
- The observed damage mostly concentrated on buildings built before the year 2000, where the quality of construction was significantly low.
- The buildings that were constructed after the 2000s performed much better than the older ones.
- The observed structural damage was similar to those observed in the past earthquakes.
- The observed non-structural damage affected the psychology of the occupants, magnifying in most cases the apparent damage, and mislead damage assessment work in the field. Its importance for seismic risk reduction is once again observed.
- A building's total collapse or no collapse is a very fine line, which is a difficult situation to decide in terms of engineering. With the strengthening of buildings, total collapse, and accordingly, the loss of life can be prevented.
- The urbanization and reconstruction of buildings vulnerable to collapse under low to moderate seismic excitations similar to Elâzığ city center case are vital to saving lives.
- Economic strengthening of the buildings that are expected to sustain moderate to heavy damage after earthquakes is extremely important for seismic risk reduction.
- Engineered proper systems for infill walls must be enforced to eliminate in-plane infill wall damage and out of plane collapse.

Chapter 6
Post-Earthquake Damage Assessment in Rural Areas

Prof. Murat Altuğ ERBERİK[1]

Prof. Ayşegül ASKAN GÜNDOĞAN[1]

Res. Asst. Aylin ÇELİK[1]

[1] *Middle East Technical University*

6.1 Introduction

This chapter focuses on the post-earthquake field investigations, observations and evaluations that were conducted on January 29-30, 2020 in rural regions close to the ruptured fault line. Accordingly, the technical team investigated Sivrice sub-province and five rural districts in a detailed manner. The locations of these places are shown in Figure 6.1 The epicenter of the earthquake has also been shown by the asterisk sign on the same figure. The observations and evaluations of the field investigation are provided in the following sections.

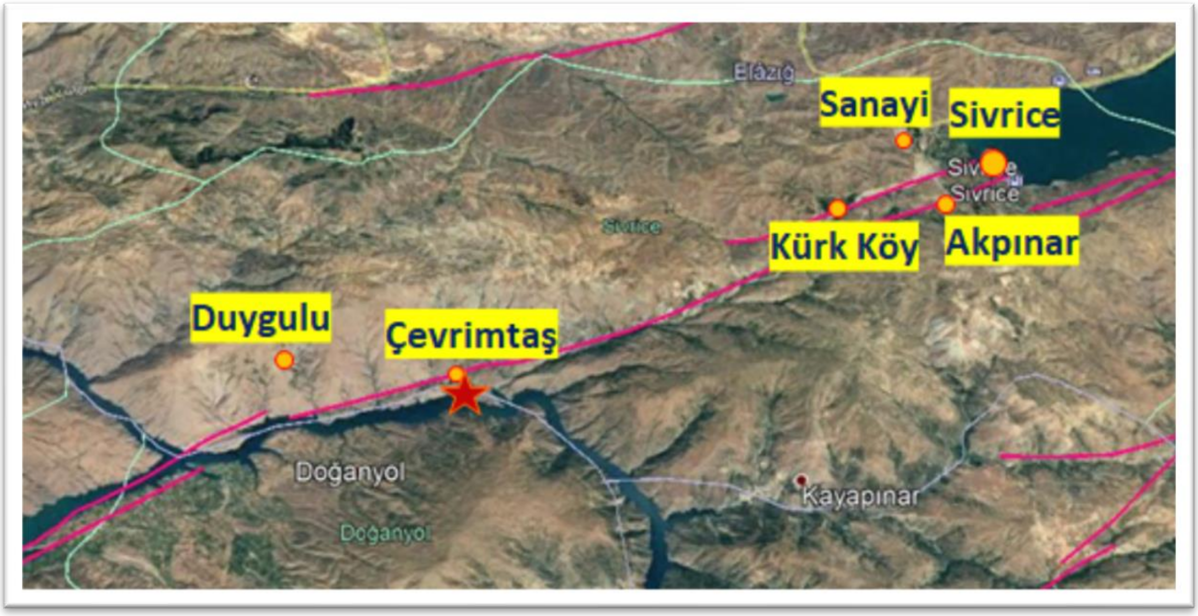

Figure 6.1 The rural districts close to the fault line which were thoroughly investigated

6.1.1 Sivrice Sub-province

First the technical team visited Sivrice sub-province, which is the most affected populated area from the earthquake. As seen from the aerial photograph (Figure 6.2), Sivrice is a sub-province nearly on the fault line with a population of 10,000 and having 400-500 dwellings on the southwest coast of Hazar Lake. There are 52 remote villages of this sub-province. The building stock is mostly composed of low-rise unreinforced masonry (URM) and low-rise and mid-rise old reinforced concrete frame structures (Figure 6.3). Although the number of collapsed buildings in this province, which is close to the fault line, is limited there exist many buildings with different levels of damage ranging from light to severe (Figure 6.4).

Figure 6.2 Aerial photograph of Sivrice sub-province (Google Earth)

Figure 6.3 A glance at the building stock in Sivrice

Figure 6.4 Photographs of damaged buildings in Sivrice

The largest and the most complex building in sub-province is the Central Mosque of Sivrice (Figure 6.5). According to the residents, the mosque has already been lightly damaged after the 2019 December earthquake and it then experienced heavy damage after the last earthquake. As seen in Figure 6.5, there are wide shear cracks and partial collapses in the out-of-plane direction on the perimeter walls.

When the damaged mosque is examined thoroughly, it has been observed that the mosque possesses many structural deficiencies. The concrete strength seems to be low in all the load-bearing members (i.e. columns and beams), there is not adequate spacing between the lateral reinforcement and there is corrosion in the longitudinal reinforcement (Figure 6.6). In addition, on the basement floor of the mosque, there is heavy damage to some of the columns in terms of hinge formation at the member ends due to the short column effect (Figure 6.6).

Figure 6.5 The Central Mosque of Sivrice, which was heavily damaged after the earthquake

Figure 6.6 Observed damage in the Central Mosque of Sivrice

6.1.2 Kürk Village

Kürk village, which is located on the southeast of Sivrice, is on the north of the ruptured fault line. In the north part of the village, there are two identical stone masonry buildings, which were occupied as the school building and its lodging in the past, according to the residents of the village (Figure 6.7). The structures are very similar to the stone masonry building that was collapsed in Palu during the 2010 Elâzığ-Karakoçan earthquake (Figure 6.8). In one of these abandoned buildings, there has been a partial collapse in the corner due to poor wall-to-wall connection during the earthquake.

Figure 6.7 Two stone masonry buildings in Kürk village which were used as school building and its lodging in the past

Figure 6.8 A similar stone masonry school building which collapsed in Palu during the 2010 Elâzığ-Karakoçan earthquake

Further investigations in the village revealed that the non-engineered stone and adobe masonry buildings were generally heavily damaged or collapsed (Figure 6.9). The main reason is the low strength and quality of the masonry units and mortar that have been used to construct the load-bearing walls. In addition, the use of different materials in the same wall causes loss of integrity and homogeneity in masonry walls (Figure 6.10).

Figure 6.9 Heavily damaged or collapsed stone and adobe masonry buildings in Kürk village

Figure 6.10 Non-homogeneous nature of the collapsed masonry walls in Kürk village

In addition to the heavily damaged and collapsed buildings in the village, there also exist lightly damaged structures (Figure 6.11). These buildings seem to have been constructed more recently, mostly by using reinforced concrete frame system. They have fewer structural deficiencies than the collapsed non-engineered buildings. This proves the observation that for structures for which seismic intensity level is almost the same, the seismic performances can be totally different depending on the structural characteristics and vulnerabilities of these structures.

Figure 6.11 Low-rise concrete building with light damage in Kürk village

6.1.3 Sanayi District

The field observations in Sanayi district have revealed that the structures in the region have not experienced severe damage during the earthquake (Figure 6.12). As the building quality seems to be better than the previous village investigated (i.e., Kürk village), the buildings have mostly experienced light damage. One of the most critical damage is the fall of the top of the minaret in the mosque, as seen in Figure 6.13.

Figure 6.12 The condition of the buildings in Sanayi district after the earthquake

Figure 6.13 The damaged minaret of the mosque in Sanayi district

6.1.4 Akpınar Village

Akpınar village is located close to Sivrice sub-province, just like Sanayi district, but at a higher elevation. The building stock in this village is composed of single-story masonry buildings (Figure 6.14). Some of these structures, which have been built with stone and adobe units as masonry material, have experienced damage during the earthquake. On the other hand, brick masonry structures are observed to have better performance in this village. It should also be mentioned that there are no completely collapsed buildings in Akpınar.

Figure 6.14 The condition of the buildings in Akpınar village after the earthquake

6.1.5 Duygulu Village

After completing the field investigations in the vicinity of Sivrice sub-province, the technical team followed the fault line in southwest direction and arrived at a village in the mountains, named as Duygulu village. The investigations showed that the buildings had experienced different damage levels, varying from light damage to collapse (Figure 6.15). Despite the collapsed buildings in the village, there are fortunately no casualties. Most of the buildings are masonry constructed using different materials. There are few newly constructed masonry and reinforced concrete buildings where no severe damage was reported (Figure 6.16). Some of the buildings have also been investigated from inside and it was observed that the damage is generally due to low material strength, poor wall-to-wall and wall-to-floor connections (Figure 6.17). Weak connections prevent the structures to exhibit box-like behavior. This causes the walls to show independent cantilever-like behavior, which is prone to the out-of-plane collapse of the wall.

Figure 6.15 Rural structures in Duygulu village with different damage levels

Figure 6.16 Newly constructed and lightly damaged buildings in Duygulu village

Figure 6.17 Structural damage from the inside of buildings in Duygulu village

The mosque in the village deserves some attention since it is a historic masonry building, which is said to have been officially registered to the Turkish Republic Ministry of Culture and Tourism (Figure 6.18). The name plate states that it had been constructed in 1883, but the villagers claim that it had been built earlier. It has also been noted that the mosque experienced interventions multiple times in the past, especially the minaret, which was renovated a few years ago. However, the structure is still observed to possess severe damage after the earthquake. The arches and the colonnades have wide cracks. Some of the veneer stones have fallen down. There are also severe cracks in the masonry walls of the mosque (Figure 6.19). There are also some cracks and separations on the body of the minaret.

Figure 6.18 The historical masonry mosque in Duygulu village

Figure 6.19 The observed damage in the mosque

6.1.6 Çevrimtaş Village

Çevrimtaş village is the closest residential area to the epicenter of the earthquake along the fault line. The village is located in two regions: along the riverside and along the hillside (Figure 6.20). Although the distance between these two districts is at most 300-400 meters, the damage distribution is totally different. All the structures along the riverside were collapsed, and people lost lives (Figure 6.21). However, it is possible to encounter buildings with varying states of damage (light, moderate, severe damages and collapse) along the hillside (Figure 6.22). No casualties were reported in this district. A comparison of the structures in these two districts (riverside and hillside) reveals that they have very similar structural properties but totally different performances during the earthquake. The main reason is that the buildings along the riverside are very close to, probably just on the fault line, whereas the ones along the hillside are a little bit far away from the fault line. The total devastation of structures only on the fault line has already been experienced in past major earthquakes, particularly the 17 August 1999 Kocaeli earthquake. Such observations in this earthquake as well as in past earthquakes encourage taking measures about a safety area along the fault line on which no construction is allowed. In addition, the ruins close to the riverside district prove that once the village had been constructed in a nearby location but then it had been abandoned, probably after another major historical earthquake (Figure 6.23).

Figure 6.20 Two different districts in Çevrimtaş village

Figure 6.21 Completely collapsed buildings along the riverside in Çevrimtaş village

Figure 6.22 Buildings with different damage states along the hillside in Çevrimtaş village

Figure 6.23 Ruins of the past settlement area close to riverside district

6.1.7 Other Villages Close to the Fault Line

The limited information regarding the damage distribution in some of the nearby villages in addition to the ones that have been investigated in detail, as explained in the above sections, is presented in Figure 6.24. The supplied data reveals that the damage increases getting closer to the fault line, and the epicenter of the earthquake, stone, and adobe masonry structures have generally experienced severe damage and collapse, whereas brick masonry and concrete structures have responded to the earthquake with better performance.

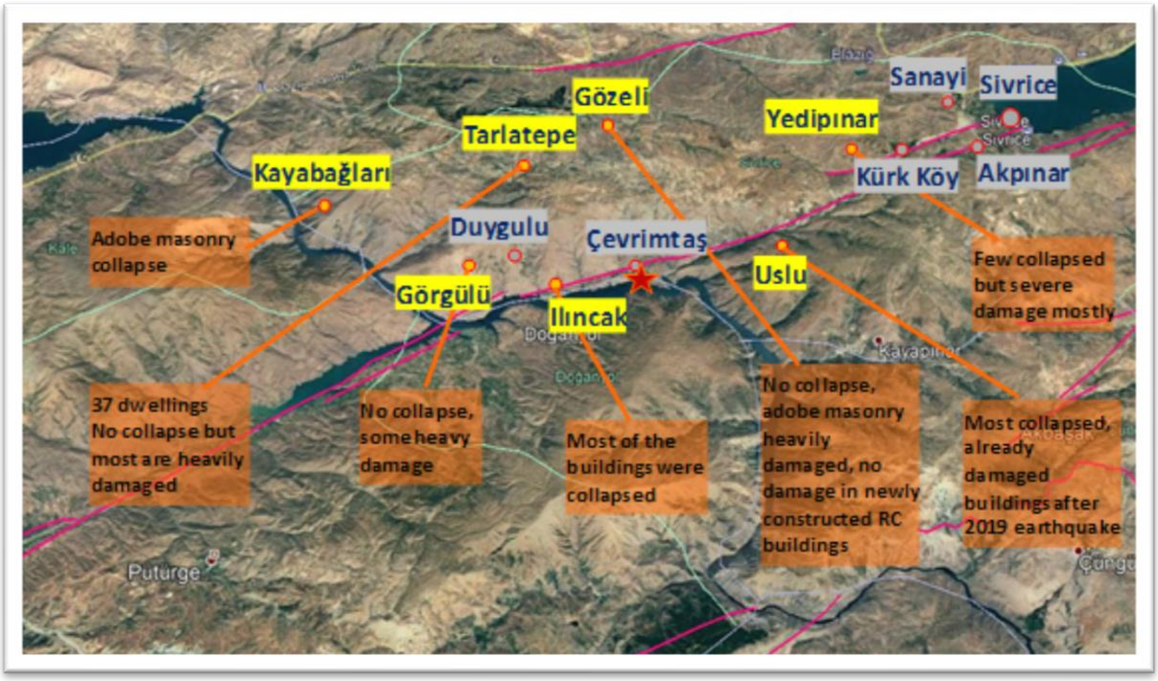

Figure 6.24 Damage distributions in some of the villages near the fault line

6.2 General Post-Earthquake Observations Regarding Rural Structures

Post-earthquake observations regarding the structural damage distribution in rural areas can be stated as follows:

- There seem to be a higher number of collapsed or heavily damaged buildings in rural areas when compared to the urban areas due to the use of poor construction materials and lack of engineering touch in rural structures. Fortunately, the rural population has moved to the cities in the winter period, which is a factor that seems to have reduced the death toll significantly.
- In rural regions, the heavily damaged and collapsed buildings are generally stone and adobe masonry buildings. It has been observed that low-strength masonry units and mortar were used in the damaged buildings. In addition, the safe load paths do not exist due to poor connections between walls and floors. This caused vulnerability in the walls, especially in the out of plane direction during the earthquake.
- Low-rise RC buildings constructed in rural areas seem to have exhibited relatively better performance than non-engineered masonry buildings. This is due to the fact that they possess less structural deficiency, and material quality is generally higher.
- The field investigations show that damage ratio increases closer to the fault line and the epicenter. Particularly on the fault line, the damage seems to be catastrophic with total destruction. Such observations point out the necessity to take serious measures about a safety area along the fault line on which construction is not allowed or it is only allowed under specific conditions.

Chapter 7
Observations on the Performance of Bridges

Prof. Alp CANER[1]

Andrea NATALE[1]

Kerem BOYACI[1]

Doğucan YILMAZ[1]

[1] *Middle East Technical University*

7.1 Introduction

This section summarizes the observations of the field study trip performed on Feb 1-2, 2020 after the Elâzığ earthquake. In these reconnaissance surveys, mainly bridges were examined within 100 km radius of the epicenter.

A total of 19 bridges were investigated for structural performance. Some of the bridges were built around 1950's and some of them are within 1 km vicinity of the active fault line. All the bridges have satisfied the immediate use performance just after the earthquake. Only two bridges have observed to have minor movements or stressing at their abutments marked in yellow in Figure 7.1. The other bridges had observed to have no damage induced by the earthquake. Similar observations for another group of bridges have been also made also immediately after the Van Earthquake 2011 M_w: 7.1.

The locations of the visited bridges are shown below.

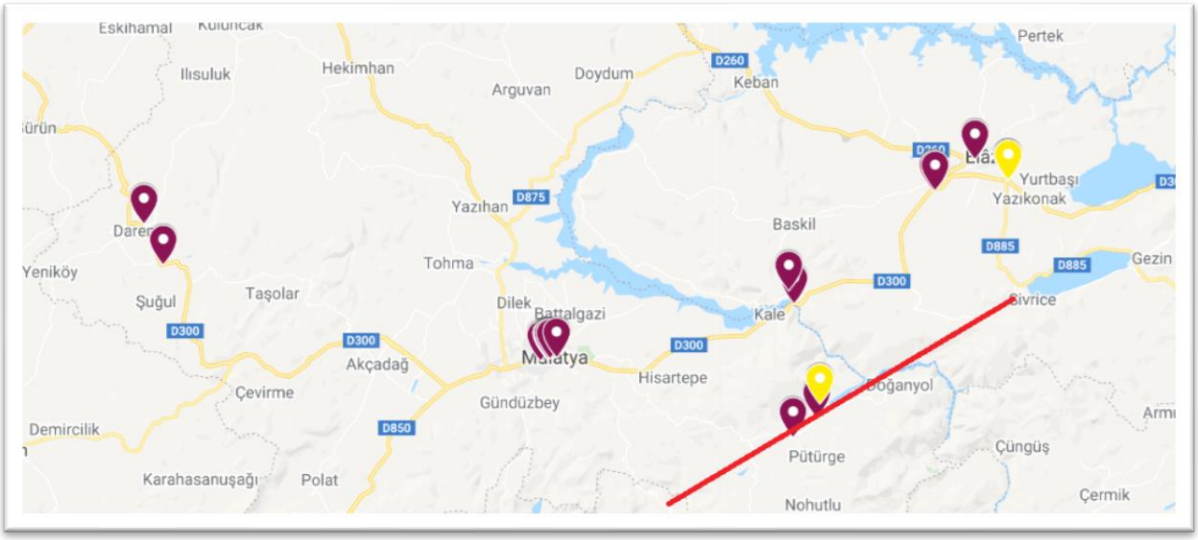

Figure 7.1 Bridge locations

7.2 Observations

A special cable-stayed bridge still under construction was subjected to earthquake survived with no visible damage (Figure 7.2). The old post-tensioned box girder bridge constructed with balanced cantilever method was also in service. The bridge had a main span of 135 meters.

Figure 7.2 Cable-stayed Kömürhan Bridge (distance from epi-center: 23.5 km, distance from fault line: 18 km) ve post-tensioned box Kömürhan Bridge (construction year: 1986)

In the very same region and very close to these Kömürhan bridges, another post-tensioned box bridge with a main span of 150 meters were under service just after the earthquake. This particular bridge had a rehabilitation in 2018 for service loads (Figure 7.3).

Figure 7.3 Beylerderesi Bridge (construction year: 2010)

The Talis reinforced concrete bridge with gerber girders was in the vicinity of the fault line and no damage induced by earthquake was observed. (Figure 7.4). The bridge constructed around 1978 had a typical continuous span of 23 meters.

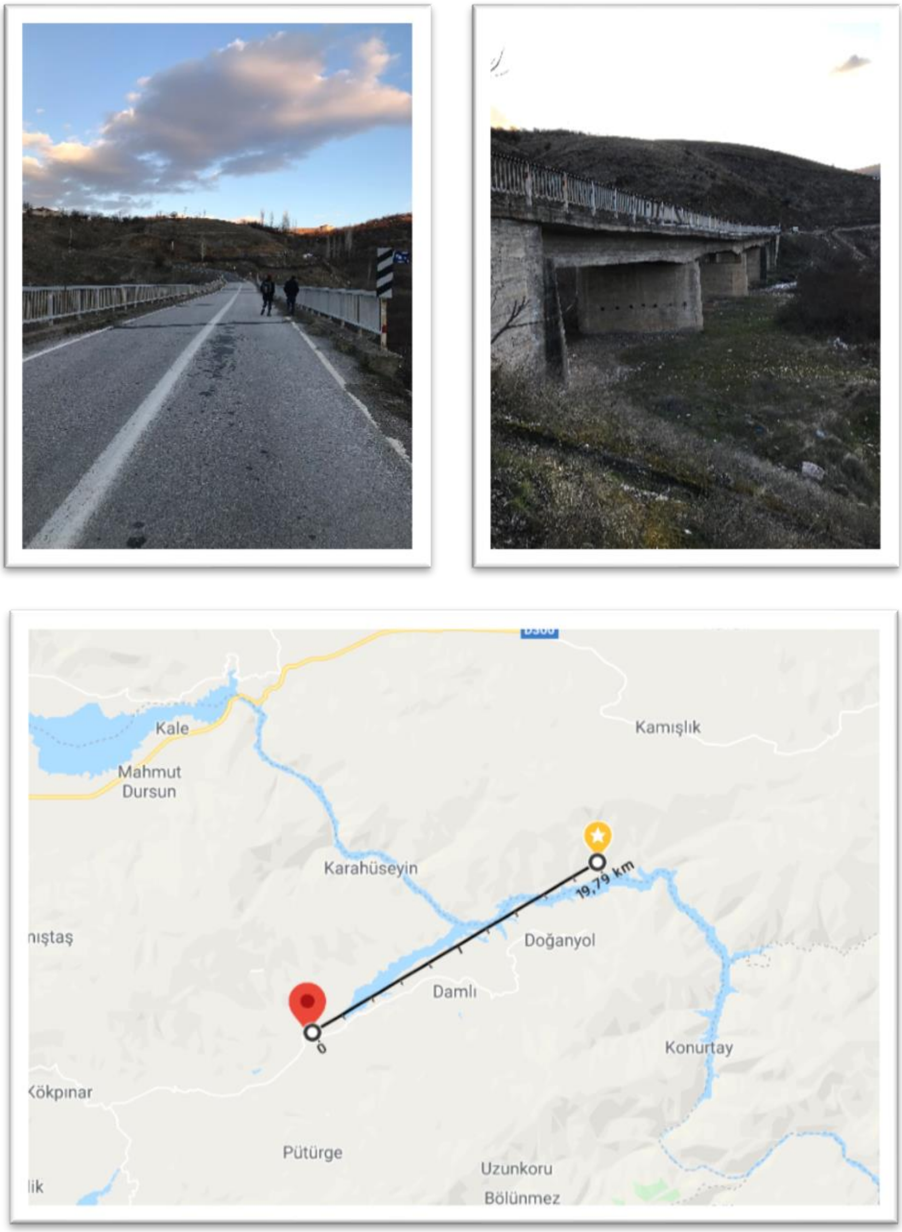

Figure 7.4 Talis Bridge (distance to epi-center: 19.7 km, distance to fault line < 1 km)

A village bridge very close to the Talis Bridge has a steel composite superstructure. The bridge had been observed to have a relative movement at the abutment of about 10 cm. The bridge is believed to be constructed around 1950’s. Each pier has five steel columns and the last column at each pier has a rotation about its vertical axis. Based on the age of this bridge, total replacement can be considered instead of a repair. The bridge was still under service at the time of the visit as shown in Figure 7.5. Drone flies has been conducted around the bridge to develop a digital map to measure dimensions and distances.

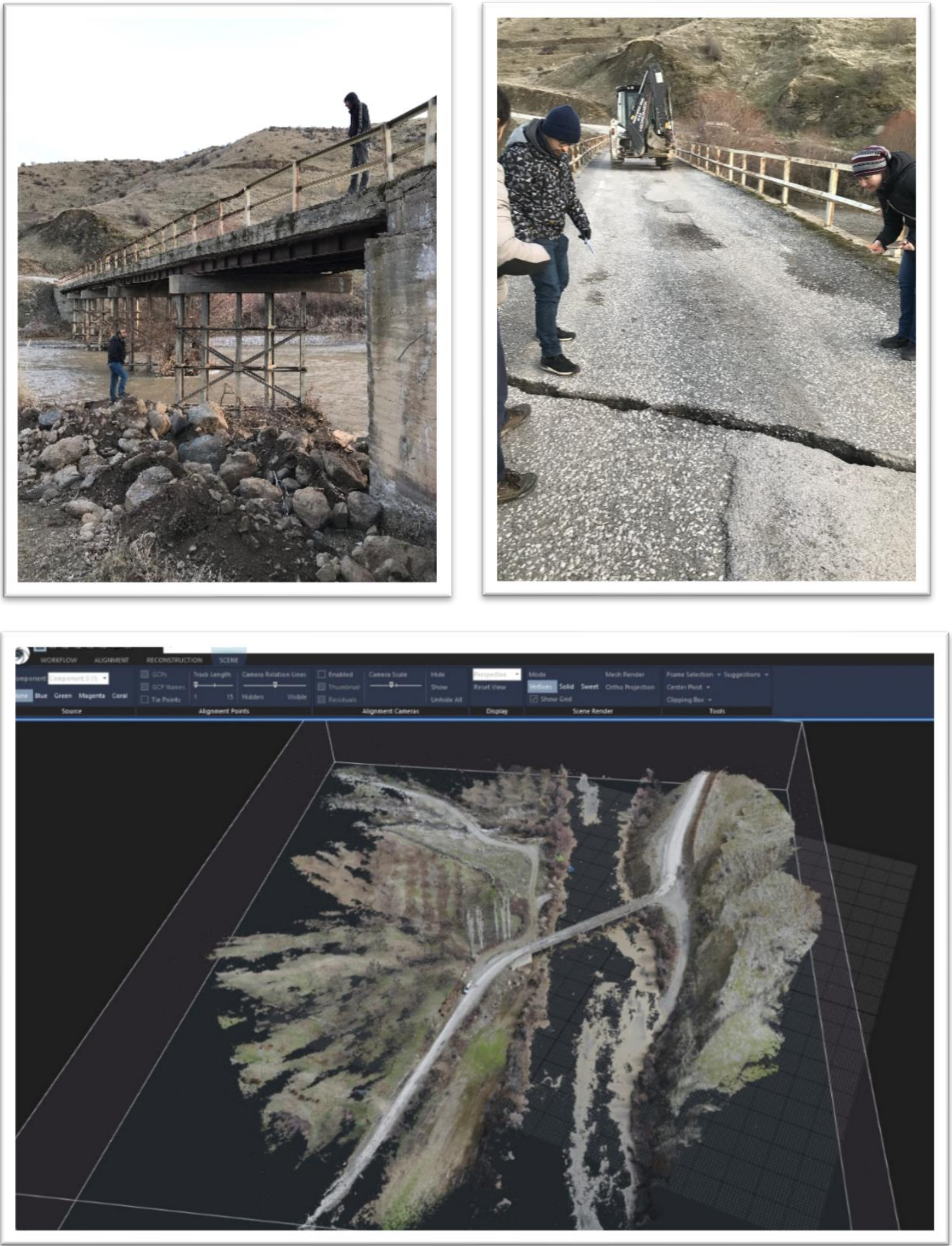

Figure 7.5 Steel composite village bridge (distance to epi-center: 19.7 km, distance to fault line < 1 km)

Köprügözü Bridge, two continuous spans constructed with reinforced concrete girders in 2001. Each span is about 21 meters and bridge has no damage as shown in Figure 7.6.

Figure 7.6 Köprügözü Bridge (distance to epi-center: 140 km, distance to fault line: 60 km)

In the city of Elâzığ, there are couple of bridges and overpasses. Construction of precast girder on slab bridges are very common in the city very similar to the construction practice in Turkey. In one of the bridges, the shear key at the abutment has cracked due to close gap between girder and shear key as shown in Figure 7.7. As known in bridge engineering practice, these shear keys restrain the transverse movement of the bridge. Some of these bridges has reinforced earth system at their abutments and approaches. These soil retaining structures has observed to be functioning perfectly.

Figure 7.7 Typical Elâzığ city bridge (distance from epi-center: 35 km, distance to fault line: 19 km)

7.3 Conclusions

- All observed bridges have satisfied the immediate use performance after the major earthquake even if some of them are very close to the fault line within 1 km. It is believed that simple hand computations are used in design of bridges with some basic seismic computations around 1950's.
- Out of 19 bridges, 17 of them has no damage at all. One slender bridge in the vicinity of the fault line by 1 km, has a relative movement of the superstructure at the abutment. The movement has not been tried to be restrained by shear keys as designed in modern bridges. A modern highway bridge about 20 km from the epi center of the earthquake has a crack at its shear key at the abutment due to lack of sufficient gap between girder and shear key. Most likely, if the gap was larger no damage will be observed during the earthquake. At each pier, there are five steel columns and the last column at each pier had a rotation about its vertical axis. Such a rotation can develop due to a past flood or current earthquake
- For aged bridges such as the steel village bridge, replacement may be the best option rather than trying to retrofit or repair them.
- In the Van Earthquake 2011, M_w 7.1, the bridges around Van also satisfied the immediate use performance. Perhaps one of the main reasons, bridges did not subject to major damage is they are more engineered compared to buildings. One other reason may be some movement is usually allowed between the superstructure and substructure thru bearings that gives some mechanical flexibility to the system. In building structures most of the flexibility is based on ductility of the framing system that can easily get damage during earthquake.

References

Abrahamson, N., Atkinson, G., Boore, D., Bozorgnia, Y., Campbell, K., Chiou, B., Idriss, I. M., Silva, W., and Youngs, R., (2008). “Comparisons of the NGA ground-motion relations”, Earthquake Spectra 24, 45–66.

Akkar, S., A. Aldemir, A. Askan, S. Bakır, E. Canbay, I.O. Demirel, M.A. Erberik, Z. Gülerce, P. Gülkan, E. Kalkan, S. Prakash, M. A. Sandıkkaya, V. Sevilgen, B. Ugurhan, E. Yenier (2011). 8 March 2010 Elâzığ-Kovancılar (Turkey) Earthquake: Observations on ground motions and building damage. Seismological Research Letters, 82, 42-58. (DOI: 10.1785/gssrl.82.1.42).

Akkar, S., Azak T., Çan T., Çeken U., Demircioğlu Tümsa M. B., Duman, T. Y., Erdik, M., Ergintay, S., Kadirioğlu, F. T., Kalafat, D., Kale, Ö., Kartal R. F., Kekovalı K., Kılıç T. S., Zülfikar Ö. (2018). “Evolution of seismic hazard maps in Turkey”, Bulletin of Earthquake Engineering, Vol.16, Issue 8, pp 3567-3570.

Akkar, S., Kale, Ö., Yenier, E., and Bommer, J. J. (2011). “The high-frequency limit of usable response spectral ordinates from filtered analogue and digital strong-motion accelerograms”, Earthquake Engineering and Structural Dynamics 40, 1387–1401.

Aksoy, E., (1993). “Elâzığ batı ve güneyinin genel jeolojik özellikleri”. Doğa Türk Yerbilimleri dergisi.

Ambraseys, N.N. (2009). “Earthquakes in the Mediterranean and Middle East: a multidisciplinary study of seismicity up to 1900”. Cambridge University Press, Cambridge, UK 947pp.

ASTM D2487-17, Standard Practice for Classification of Soils for Engineering Purposes (Unified Soil Classification System), ASTM International, West Conshohocken, PA, 2017.

ASTM D6913 (2017). Standard Test Method for Particle-Size Distribution (Gradation) of Soils Using Sieve Analysis.

ASTM D7928 (2017) Standard test method for particle-size distribution (gradation) of fine-grained soil using the sedimentation (hydrometer) analysis. ASTM International: West Conshohocken (PA).

Avşar, N., (1983). “Elâzığ yakın kuzeybatısında stratigrafik ve mikropaleontolojik araştırmalar” Doktora tezi.

Barka, A. (1996). “Slip distribution along the North Anatolian Fault associated with the large earthquakes of the period 1939 to 1967”, Bull. Seismol. Soc. Am. 86, 1238-1254.

Bilal, M. and A. Askan (2014). “Relationships between Felt Intensity and Recorded Ground-Motion Parameters for Turkey”, Bulletin of the Seismological Society of America, 104 (1), 484–496. (DOI: 10.1785/0120130093).

Boore, D. M., and Atkinson, G. M., (2008). “Ground-motion prediction equations for the average horizontal component of PGA, PGV, and 5%-damped PSA at spectral periods between 0.01 s and 10.0 s”, Earthquake Spectra 24, 99–139.

Boore, D. M., Stewart, J. P., Seyhan, E., and Atkinson, G. A., (2014). “NGA-West 2 equations for predicting PGA, PGV, and 5%-damped PSA for shallow crustal earthquakes”, Earthquake Spectra 30, 1057–1087.

Bozkurt E. (2001). “Neotectonics of Turkey–a synthesis”. Geodinamica Acta 14: 3-30.

Chiou, B. S. J., and Youngs, R. R., (2008). “Chiou-Youngs NGA ground motion relations for the geometric mean horizontal component of peak and spectral ground motion parameters”, Earthquake Spectra 24, 173–217.

Chiou, B. S. J., and Youngs, R. R., (2014). “Update of the Chiou and Youngs NGA model for the average horizontal component of peak ground motion and response spectra”, Earthquake Spectra 30, 1117–1155.

Duman T. Y., Emre Ö. (2013). “The East Anatolian Fault: geometry segmentation and jog characteristics”. Geol Soc London Spec Publ 372: 495-529.

Emre Ö., Duman T. Y., Özalp S, Elmaci H., Olgun Ş., Şaroğlu F. (2013). “Active Fault Map of Turkey with an Explanatory Text”. Ankara, Turkey: General Directorate of Mineral Research and Exploration (MTA).

Gülerce, Z., Kargıoglu, B., and Abrahamson, N. A. (2016) “Turkey-adjusted NGA-W1 horizontal ground motion prediction models,” Earthquake Spectra 32, 75–100.

Gülerce, Z., Shah, S. T., Manekşe, A., Özacar, A. A., Kaymakci, N., & Çetin, K. O. (2017). “Probabilistic seismic-hazard assessment for East Anatolian fault zone using planar fault source models”, Bulletin of the Seismological Society of America, 107(5), 2353– 2366.

İnceöz, M., (1994). “Harput (Elâzığ) yakın kuzeyi ve doğusunun jeolojik özellikleri”. Doktora tezi, F.Ü. Fen Bilimleri Enst.

Kale, Ö., Akkar, S., Ansari, A. and Hamzehloo, H. (2015). “A ground-motion predictive model for Iran and Turkey for horizontal PGA, PGV and 5%-damped response spectrum: Investigation of possible regional effects”, Bulletin of the Seismological Society of America, 105, 2A, 963-980.

Kale, Ö. (2019). “Some Discussions on Data-Driven Testing of Ground-Motion Prediction Equations under the Turkish Ground-Motion Database”, Journal of Earthquake Engineering, 23(1), 160–181.

Kurtuluş, C., Sertçelik, F., Sertçelik, İ., Kuru, T., Tekin, K., Ateş, E., Apak, A., Kökbudak, D., Sezer, S., & Yalçın, D. (2019). “Ulusal Kuvvetli Yer Hareketi Kayıt İstasyonlarının Zemin Parametrelerinin Belirlenmesi”, Ulusal Deprem Araştırma Programı (UDAP), AFAD.

Palutoğlu,M., Tanyolu E. (2006). “Elâzığ İl Merkezi Yerleşim Alanının Depremselliği”, Fırat Üniv. Fen ve Müh. Bil. Dergisi, 18 (4), 577-588.

Sandıkkaya, M. A., Yılmaz, M. T., Bakır, B. S., & Yılmaz, Ö. (2010). “Site classification of Turkish national strong-motion stations”. Journal of Seismology, 14(3), 543–563.

Sengör A. M. C., Gorur N., Saroglu F. (1985). “Strike-slip faulting and related basin formation in zones of tectonic escape: Turkey as a case study”. Society of Economic Paleontologists andMineralogists, Special Publication 37: 227 – 264.

Şaroğlu, F., Emre, Ö. & Kuşçu, İ. (1992). “Active Fault Map of Turkey at Scale 1:1 000 000”, Mineral Research and Explorations Institute of Turkey Publication, Ankara, 3 sheets.

Turkish Building Seismic Code, TBSC, 2019.

Taymaz, T., Jackson, J. & Mckenzie, D. P. (1991). “Active tectonics of the north ve central Aegean Sea”, Geophysical Journal International, 106, 433–490.

Tsuchida, H. (1970). Prediction and countermeasure against the liquefaction in sand deposits. Abstract of the Seminar in the Port and Harbor Research Institute.

USGS, United States Geological Survey.

Utkucu, M., Nalbant, S., McClusky, J., Steacy, S., Alptekin, Ö., (2003). “Slip distribution and stress changes associated with the 1999 November 12, Düzce (Turkey) Earthquake (M_w = 7.1).”, Geophys. J. Int. 153, 229–241.

Wells D. L., Coppersmith K. J. (1994). “New empirical relationships among magnitude, rupture length, rupture width, rupture area, and surface displacement”. Bulletin of the Seismological Society of America; 84 (4): 974–1002.